

THE UNIVERSITY OF HULL

**ASPECTS OF LASER TISSUE INTERACTION
IN PHOTODYNAMIC THERAPY**

being a Thesis submitted for the Degree of

DOCTOR OF PHILOSOPHY

in the University of Hull

by

Graham Pyper BSc (Hons)

October 1997

I would like to dedicate this to my mother for her immense support and my late father

David J Pyper, who constantly took the “mick.”

And to my late brother in law John Graham.

Acknowledgements

Chapter 1: Introduction	1
Aims	1
Photodynamic Therapy	2
Clinical applications	3
Mathematical model	3
Goniometry	4
Kubelka-Munk Theory	5
Integrating sphere	5
Added absorber method for determining the effective attenuation coefficient of Soyacal	6
Displacement Sensor probes	6
1.1 References	8
Chapter 2: Overview of Photodynamic Therapy	9
2.1 Introduction	9
2.2 Cancer	9
Unrestrained growth and proliferation	10
Defying the laws of death (apoptosis)	10
The ability to invade and infiltrate surrounding tissue and to establish secondary lesions	11
2.3. Historical Perspective of PDT	12
2.4 Light Delivery Systems	12
Laser Sources	13

	Optical fibres	14
2.5	Clinical Applications	16
	In vivo biological response in human lung cancer	16
	Moghissi's method of bronchoscopic PDT	18
	Solar photosensitivity	19
	Photobleaching	19
2.6	Chemistry of Heamataporphyrin Derivative	20
2.7	Singlet Oxygen	22
2.8	Sensitiser Distribution in Cells and Tissues	24
2.9	Molecular and Cellular Effects	25
	Membrane damage	26
	Cellular Effects	27
	Enzymes	28
	Vascular effects	28
2.10	Hyperthermia	29
2.11	References	32
Chapter 3	Derivation of the Diffusion Approximation from Transfer theory	35
3.1	Introduction	35
3.2	Radiative Transfer Equation Derivation	36
	Cross-sections and Scattering Amplitude	37
	Specific Intensity	38
3.3	The Diffusion approximation for slab geometry	43

	Slab Geometry	43
	Radiance and diffuse intensities	44
	Diffusion approximation using Legendre Polynomials	46
	Fluxes	48
	Space Irradiance	50
	Diffusion equation derivation	52
3.4	References	56
Chapter 4:	Goniophotometry	57
4.1	Introduction	57
4.2	Phase Function	58
	Eddington phase function	60
	Delta Eddington phase function	60
	Henyey – Greenstein phase function	61
4.3	Goniophotometer apparatus	63
4.4	Tissue preparation	64
4.5	Data analysis	67
4.6	Least square fit	72
4.7	Results/Discussion	74
4.8	References	76
Chapter 5:	Reflectance and Transmission Measurements	78
5.1	Introduction	78

5.2	Kubelka-Munk Theory	79
5.3	Single Integrating Sphere theory	82
	Diffuse irradiance of sample	83
	Baffle Effects	86
	Diffuse Reflectance	86
	Collimated Incident Light	86
	Sphere Measurements	88
	Determining Sphere Coefficients	90
5.4	Experimental Methods	92
	Experimental Apparatus	92
	Tissue Preparation	93
5.5	Results	94
5.6	Discussion	96
5.7	References	99

Chapter 6: Effective attenuation coefficient

	in vitro and in vivo	101
6.1	Introduction	101
6.2	Added absorber method of determining the optical properties of a Phantom	102
	Theory	102
	Absorption and reduced scattering coefficients	103
6.3	Dipole theory for displacement probes	104
6.4	Displacement sensor probe construction	106

Optical fibre preparation	107
Light diffusing sphere for optical fibre	108
Thermocouple Placement	109
Mutual inductance coil construction	109
Rigid Sheath for handling purposes	110
Probe Shielding	110
Probe Terminations	111
6.5 Experimental methods	112
Soyacal	112
Lung tissue	113
In vivo experimental method	114
Displacement sensor Alignment	115
6.6 Results	116
6.7 Discussion	119
6.8 References	121
Chapter 7: Conclusion	122

Acknowledgements

I would like to thank first and foremost Prof. Moghissi. Not only for the Laser Trust Moghissi Appeal that funded my research but for his concern in the PhD and myself. For all at ward 7 in Goole district hospital especially Kate Dixon for her support and readiness to help, thank you.

As always none of this would be possible without the skills of the technical staff.

Thanks to Paul for his prompt response and advice about the most trivial of details. To Brian and Gordon for all those “niggley” electronics problems that were eventually sorted out. To Terry the glass man and finally to Graham who saved the day by lending me equipment at short notice.

Thanks to my close friends who lived through this as much as me and survived. Special thanks to Geoff who put his computer skills to use when the sky fell in and I was burgled. My poor house-mates over the years have suffered and will all be glad to hear that I have finished. Thanks to the entire Ju-Jitsu club for the great social life and cheering up when needed.

Thanks to my mother, Trudy, Oriel and uncle Herbie for there support over the years especially the food parcels disguised as money. Especial thanks to Jayne for being with me over the years and eventually seeing the light. Thanks for being there when I was ill and when I wasn't, I didn't appreciate it at the time but do now.

Finally but not least, to my supervisor Prof. Pete Dyer for his guidance through these years and for solving and explaining what to me were mountains but mole hills to him.

Introduction

Aims

Over the last few decades the use of lasers in medicine has become common practice in such areas as ophthalmology, tumour removal, gynaecology, cosmetic surgery, etc.

However in spite of their widespread use the general principles of laser-tissue interaction is still in its infancy because the optical properties of biological media are in general complex and are characterised by local inhomogeneties. In vitro measurements have the advantage over in vivo measurements in that the effect of individual tissue structure may be evaluated. However, they are also subject to preparation artefacts and don't have the circulatory systems of the human body. Results by other researchers to date indicate wide variations in optical coefficients not only for different tissue types but also for similar tissues, depending on the method of measurement and theoretical model used. The aim of this thesis was to investigate the optical properties of Soyacal an intravenous feed, pig lung tissue and human necrotic lung tissue and to develop an optical source and detecting probe for in vivo human lung experiments.

The optical parameters of Soyacal i.e. the absorption, scattering coefficients and the anisotropy factor (mean cosine of scatter) have previously been investigated near the 630nm wavelength.^{1 2} The experiments performed on the Soyacal solution were used as a reference guide to ensure the correct experimental techniques were used.

An initial question arose whether to investigate tissue with or without blood present in the samples? Other researchers have only reported optical values for lung tissue without blood. The two human necrotic tissue samples retrieved from patients during Photodynamic therapy (PDT) treatment obviously had blood in the tissue. Since the ultimate aim of the thesis was to investigate human necrotic tumour both in vitro and in vivo, tissue samples of pig lung with and without blood were investigated. Therefore a direct comparison between other researchers could be made and between in vivo and in vitro results.

Photodynamic Therapy

Photodynamic therapy is a means of selectively eradicating tumours by injection of a tumour localising, wavelength dependent, photosensitising agent and by irradiation of laser light. Chapter 2 includes a brief description of how and why cancer spreads and a brief summary on the history of PDT. Clinical applications are described for human lung cancer with a method of bronchoscopic PDT summarised. The distribution of the sensitiser in tissue is detailed with subsequent molecular and cellular effects. The photosensitiser is active over a given wavelength and it is this wavelength that determines the laser type and delivery system. Types of lasers and delivery systems are described with the emphasis on PDT of lung tumours. Optical fibres are used in the application of laser light to the treatment site. The size, shape and position of a tumour will directly influence the type of fibre system used. The clinical effectiveness of PDT for treatment of tumours depends on the appropriate delivery of both light and photosensitiser to the target tissue.

Clinical applications

The patients were injected with a photosensitising dye (Photofrin[®] II) 12 – 24 hours prior to the operation. The photosensitiser accumulates more readily in the tumour than in normal tissue. The laser system used in PDT and for the experimental work was an Argon ion pumped dye laser producing 1- 3W output from the delivery system. The delivery system was most commonly a 600 μ m quartz optical fibre with a 1cm-diffusing tip. The photosensitiser when irradiated with light reacts to form a highly reactive form of oxygen, which kills the malignant cells. This reaction is still not fully understood. One week following the operation the patient is then assessed and debridement is carried out at the irradiated site. PDT is a successful treatment to eradicate tumours of the lung.

Mathematical models

Knowledge of light propagation in tissue is essential for accurate dosimetry during therapy. A rigorous and detailed analysis of the optical distribution is impossible because of the optical complexity of tissue. It is therefore necessary to simplify the description so that it will meet the requirements for accuracy during clinical procedures and simultaneously be of reasonable physical and mathematical complexity. Most light propagation models are approximations of transport theory³. By assuming tissue homogeneity and a regular geometry an estimate of the distribution of light can be calculated by solving the radiative transport equation.⁴ This requires knowledge of the absorption and scattering properties of the tissue and the phase function, characterising the scattering events in the tissue.

The diffusion approximation⁵ is a solution of the transport equation and is presented in chapter 3. The transport equation is approximated to the one dimensional diffusion approximation but written in terms of a set of differential equations for collimated forward flux and the diffuse forward and backward flux.

Goniometry

For anisotropic scattering experimental estimation of the phase function is necessary, this is accomplished by measuring the angular distribution of scattered light from thin samples. The direct phase function measurements performed by goniometry and a HeNe laser at 633nm wavelength on thin slices of tissue have established the preference for the Henyey-Greenstein⁶ phase function, which describes the forward scattering nature of most tissues. Measurements of reflection and transmission as a function of angle are presented for tissue thickness ranging from 25 to 500 μm . Extrapolation of the angular scattering data to the limit of an incremental tissue thickness specifies the scattering phase function appropriate for use in the radiative transport equation.⁷ Experimental results, methods and data are discussed in chapter 4, for pig lung tissue with and without blood present and human necrotic tissue for the measurement of the angular distribution of scattered light.

Kubelka-Munk Theory

Experimental determination of the optical properties of tissue requires not only the solution to the transport equation in the experimental geometry but also suitable relations between this solution and the optical properties. In chapter 5 a system is described for the measurement of the optical properties of tissue ie the scattering and absorption coefficients. The Kubelka – Munk (K-M)⁸ solution with the transfer theory is used to determine the absorption and scattering coefficients of media. The Kubelka - Munk solution is based on two fluxes travelling in opposite directions through a medium. Since the diffusion theory was written in terms of diffuse forward and backward fluxes a comparison with the K-M model can be made, hence relating the K-M absorption coefficients to the diffusion theory coefficients. This model provides simple equations for computing optical parameters of the diffuse reflection and transmission. The measurements of the reflection and total transmission allow the determination of the absorption and reduced scattering. The measurements are made with thin samples placed between glass slides placed on an integrating sphere port and irradiated with a HeNe laser.

Integrating Sphere

Other than goniophotometer measurements the majority of techniques involve the use of integrating spheres to measure the reflection and transmission of tissue samples.

Although the integrating sphere theory has been extensively^{9 10 11} studied sphere formulas for both diffuse incident and collimated incident light are given, as they are necessary for understanding the procedures for calibrating the spheres.^{12 13}

The power collected by a detector situated in the wall of an integrating sphere is calculated as a function of the area and the reflectance of the wall, the holes, the sample, and the detector for both diffuse and collimated light incident upon the sample. The sample is located at either the exit port (reflectance) or the entrance port (transmission) of the sphere.

Added absorber method for determining the effective attenuation coefficient of Soyacal

The light energy fluence rate of an isotropic light source immersed in an aqueous solution of 1% Soyacal with and without an added absorber as a function of distance was measured in chapter 6. The effective attenuation coefficient was the gradient of the normalised light flux measured versus the distance. The absorption coefficient of the added absorber was determined using a spectrophotometer and was assumed purely absorbing. The absorption and scattering coefficients were then determined. The absorption and scattering coefficients obtained with the added absorber method can be compared with the values obtained in chapter 4 and 5.

Displacement sensor probes

There have been few studies on human lung tissue, with all studies done in vitro. Presented in chapter 6 is a method of measuring the effective attenuation coefficient of human lung tissue in vivo. The measurements are made with two probes each probe containing an optical fibre with a diffusing sphere attached to the end. A thermocouple is attached to each probe to ensure no unwarranted temperature rise in situ. Near the

diffusing sphere a coil was wound around each fibre with an oscillating signal placed down one coil. The oscillating coil produces a magnetic flux that induces a voltage in the second coil. The distance between the two probes was measured by this mutual inductance.

In this chapter the construction techniques are described for the two displacement sensor probes. The effective penetration depth for homogenised lung tissue was measured using the displacement sensor probes and is used as a reference point for the in vivo measurement of human lung tissue. The displacement sensor probes were inserted down the bronchus of fourteen patients with experimental data on 24 placements.

1.1 References

1. Moes C J, van Gemert M J, Star W M and Marijnessen, *Appl. Opt.* **28**, 2292, (1989)
2. Star W M, Marijnessen J P, Jansen H, *Photochem. Photobiol.* **46**, 619, (1987)
3. Wave propagation and scattering in random media, Ishimaru A, New York, Academic Press, 1978
4. Wilson B C and Patterson M S, *Phys. Med. Biol.* **31**, 327,(1986)
5. Groehuis R A J, Ferwada H A, Bosh J J, *Appl. Opt.* **15**, 2059, (1983)
6. Henyey L G, Greenstein J L, *Astrophysical J.* **93**, 70,(1941)
7. Jacques S L, Alter C A and Pral S A, *Lasers in Life Sci.* **1**, (4), 309, (1987)
8. Kubelka P, Part 1 *J. Opt. Soc. Am.* **38**, 448, (1948)
9. Taylor A H, *J. Opt. Soc. Am.* **4**, 9, (1920)
10. Jacquez J A and Kuppenheim H F, *J. Opt. Soc. Am.* **45**, 460, (1955)
11. Goebel D G, *Appl. Opt.* **6**, 125, (1967)
12. Pickering J W, Moes C J, Sterenborg H, Prahl S, Van Gemert M J J. *Opt. Soc. Am. A* **9**, (4), 621, (1992)
13. Pickering J W, Prahl S A, van Wieringen, Beek J, *Appl. Opt.* **32**, (4), 399, (1993)

2 Overview of Photodynamic Therapy

2.1 Introduction

Preferential destruction of tumours with minimal damage to normal tissue is the ultimate goal in oncology. Photodynamic Therapy (PDT) with its tumour localising photosensitisers and light delivery system has emerged as a promising cancer treatment modality for certain malignancies. The need to understand the process of PDT and the effects on the tissue are of paramount importance, hence the optical properties of the tissue need to be determined. This chapter contains brief explanations of the constituent parts of PDT starting from a description of cancer to the interaction of the photosensitiser with tissue and from light delivery systems to clinical applications.

2.2 Cancer

Within the human body, cells are equipped with certain backup systems to guard against runaway mutations, one such system is cell suicide. Cancer refers to more than 100 forms of the disease. Almost every tissue in the body can spawn malignancies, whilst some can yield several histological types. During the course of our lifetime genes are being attacked by carcinogens imported into our bodies from the environment and by chemicals produced in our cells. 30% of fatal cancers may be attributed to smoking and an equal number to lifestyle, especially dietary practices and lack of exercise.

Cancer encompasses a large group of highly varied disorders that share certain key characteristics. Three of the features common to the many different cancers give rise to their most deleterious effects.

Unrestrained growth and proliferation

The first and fundamental quality of cancerous tissue is its continued enlargement through the ability of cancer cells to proliferate indefinitely. Normal cells reproduce only when instructed to do so by other cells in their vicinity; this unceasing collaboration ensures that each cell maintains its size. Cancer cells in stark contrast violate this scheme; they defeat the usual controls on proliferation and follow their own internal agenda for reproduction.

Defying the laws of death (Apoptosis)

A second defence against runaway proliferation is the number of times a cell can reproduce. After 50 - 60 life cycles, growth stops in human cells and cell suicide will occur. However an occasional cell will escape this, multiply indefinitely forming tumour tissue. Associated with this uncontrolled cell growth and division is the invasion of the tumour into surrounding normal tissue.

The ability to invade and infiltrate surrounding tissue and to establish secondary lesions.

Cancer cells also possess a more insidious property; the ability to migrate from their site of origin. This is the most feared aspect of cancer; the ability to metastasise. To metastasise, cancer cells have to detach from their original location, invade a blood or lymphatic vessel and travel in the circulation to a distant site to establish a new cellular colony. At every step, they must escape many controls that keep cells within normal limits. Cellular suicide from lack of anchorage is one of the safe guards that maintain the integrity of tissues. Cells cannot usually just float away from their original site and establish themselves elsewhere. Cancers can but is not understood how.

Blood circulation explains why various metastatic cancers spread preferentially to certain tissues. Circulating tumour cells usually get trapped in the first vascular bed (or network of capillaries) that they encounter. The first vascular bed encountered by the blood leaving most organs is in the lungs; only the intestines send their blood to the liver first. Accordingly, the lungs with their large vascular bed and high volume of circulating blood are the most common site of metastases. Photodynamic therapy for lung tumours is an effective treatment with out the need for invasive surgery.

2.3 Historical Perspective of PDT

The basic concept of PDT, namely the irradiation of tumours with visible light following administration of a photosensitising drug, dates from the turn of the century. In 1903 Tappeiner and Jesionek used topically applied eosin and sunlight to treat skin cancer patients.¹ The results of this work are unclear and apparently were not followed up.

While a number of photosensitisers can be considered for localisation and possible therapy of tumours, the porphyrins have received much attention.² Lipson et al.³ reported tumour fluorescence using Haematoporphyrin derivative (HpD) and reported the first use of HpD to treat cancer. In 1975 Dougherty⁴ reported that HpD activated by red light could cause complete eradication of transplanted mouse mammary tumour without excessive damage to the surrounding skin.

2.4 Light Delivery Systems

The requirement for light sources and delivery systems in PDT is to achieve adequate irradiation throughout the target tissue volume. This means having both enough optical power within the appropriate photoactivation wavelength band of the photosensitiser and a good matching of the spatial distribution of the power with the size shape and location of the tumour. This can only be achieved by determining the size and shape of the tumour and knowing the optical characteristics of the tissue to be irradiated.

The light sources that have been used for clinical PDT are either wavelength-filtered lamps or lasers. Wavelength filtered lamps are beneficial to large easily accessible areas but are of limited use for the treatment of in vivo PDT. Sunlight has also been used for treatment of large skin areas but is not generally applicable due to the low intensity at 630nm and the practical problems of light delivery and control.

Laser Sources

The standard current light source for clinical PDT is a tuneable dye laser pumped by either an argon ion laser or a copper vapour laser producing a wavelength of 630nm. The wavelength needed for PDT depends on the absorption bands of the photosensitiser. Using a porphyrin based photosensitiser the wavelength needed is 630nm, the reasons being discussed later in this chapter. An advantage of the argon ion laser is the ability to detect tumour fluorescence by using its 514.5nm transition. The dye laser has great flexibility since the wavelength can be tuned over tens of nanometers with a single dye, with different dyes providing different spectral ranges. An obvious choice of laser would seem to be the HeNe laser, which is simple, reliable and emits light at 632.8nm however the low power is its limiting factor. However the HeNe laser can be used for experimentally determining the optical properties of tissue. A gold vapour laser is an alternative to the HeNe. This system produces 3W, 627.8nm of 50ns pulses and 10K pulses per second and eliminates the necessity of dyes.

The main advantage of the laser as a light source for PDT is the ability to couple high powers efficiently into single small core optical fibres for endoscopic use. Power ranges from 5-20 W for the lasers giving about 1-4W of red light from the dye and

about 80% may be coupled into a single fibre. Unfortunately cost, size and lack of flexibility of the equipment are the main down falls.

Other sources of light have been suggested as possible alternatives. These include wavelength-filtered lamps, light emitting diodes, laser diodes and the use of combined lasers. Light emitting diodes have the advantage of being reliable, cheap and compact, whereas the laser diode is more expensive. Unfortunately, 630nm diodes are not powerful enough to compete with the large laser systems unless arrays of diodes are used.

Optical fibres

Irradiation of inaccessible areas such as bronchial tumours requires the use of optical fibres. These fibres usually consist of a fused silica core surrounded by a cladding with a lower index of refraction. This cladding consists of either doped fused silica or silicone rubber and is usually protected by a Teflon jacket. The attenuation of light in silica fibres is very small for wavelengths in the visible and near infrared part of the spectrum but molecular vibrations of the silica dioxide molecule limit the far infrared region.

Endobronchial treatments of tumours usually require a more distributed irradiation than is obtained from an end cut fibre. It is therefore useful to use fibres equipped with diffusing tips. The commercially available diffusing tips are usually made of an epoxy resin or polymer. The diffusing tips are 2-3 mm diameter spheres attached to the end of

the fibre or 1-3cm cylindrical lengths with a diameter of 1.5 – 2.5mm. These have been used intralumenally to irradiate tumours lying along the inside of bronchi or the oesophagus. They may also be mounted within transparent cylindrical applicators to irradiate uniformly the surface of larger body cavities such as the rectum or vagina. Cylindrical diffusing fibres emit light over a large surface area with a resulting lower power density and are therefore chosen for interstitial PDT.

PDT in the human lung is more difficult than most treatment areas for several reasons. The light distributor is generally introduced through the biopsy channel of a bronchoscope the maximum internal diameter of which is 2.5mm. This is therefore the maximum diameter of the light diffuser that may be inserted. A percentage of bronchial tumours are located at the junction between two bronchi and it is necessary to use both forward firing light delivery systems and cylindrical light diffusers. The delivery of a uniform power density from an emitting straight cut fibre will have a forward peaked distribution. The formation of blood clots at the fibre tip may result in carbonisation and a subsequent quenching of light transmission and possible damage to the fibre. The dose delivered to regions in the vicinity of the straight cut fibre thus requiring the fibre tip to be placed at a distance away from the tumour surface which is not practical in this environment. These problems can be overcome by using a collimating microlens between the fibre and the tissue.

2.5 Clinical Applications

The ability to launch high optical power into single optical fibres extends enormously the clinical applications of lasers since it permits remote (endoscopic, intravascular, intracavity and interstitial) delivery of precisely controlled therapeutic energy to tissue deep within the body with minimal damage to intervening structures.

While there are cases of PDT for almost every anatomical site and histological type of solid cancer the use of PDT appears to be most encouraging for solid tumours of the bronchus, oesophagus, bladder, head, neck, skin and eyes. The majority of patients exposed to this treatment modality have been advanced cases in whom all conventional therapies have failed. Nevertheless there is now evidence to suggest that long term survival / cure can be achieved in early stages of cancer.

In vivo biological response in human lung cancer

The first patient to receive PDT for lung cancer was treated by Hayata et al.⁵ Three days following injection of 2.5mg/kg Hpd the patient received 180J/cm² of 630nm laser light with a further treatment of 120J/cm² on the 7th day after Hpd injection.

Patients are injected with the porphyrin based photosensitiser at 2mg/kg of bodyweight before being irradiated some 12-48 hours later by a laser generating 630nm and 200 J/cm² for tumour tissue. The optimum amount of photosensitiser and applied light is not known and could vary for each patient. There has been little or no experimental

data on the light distribution through in vivo tissue with or without photosensitiser being present. There has been experimental work carried out on in vitro optical properties of lung tissue with few researchers using human lung tissue. This thesis will provide the optical penetration depth of light for both in vivo and in vitro lung tissue, hence enabling the surgeon to better estimate the amount of light to be used for PDT.

Treatment is undertaken under general anaesthetic using a rigid bronchoscope for ventilation and suction purpose. In surgical centres the fiberoptic instrument is introduced through the rigid for localisation of tumour and placement of the diffusing fibre.

Generally the tumour will be necrotic one-day post treatment and slight bleeding and inflammation from the surrounding mucosa will occur. In advanced cases of cancer there is risk of postoperative problems. Post treatment debridement is an essential part of endoscopic PDT since debris of considerable size (2cm) may require removal by the surgeon.⁶ Failure to do so may result in lung collapse and infective complications. Two such pieces of tumour were removed from separate patients and used experimentally to obtain their optical properties, detailed later in this thesis. For larger lesions multiple treatments are frequently needed especially if the tumour has obstructed the lumen.

Moghissi's method of bronchoscopic PDT

Every patient had bronchial biopsy prior to admission for PDT and had positive histological diagnosis of cancer. Prior to treatment bronchoscopic examination was carried out on every patient in order to map out the topography of the tumour within the bronchial tree and assess severity of obstruction. In all cases the aim is to irradiate the tumour with $200\text{J}/\text{cm}^2$ of 630nm light. This is achieved by selecting the appropriate diffuser with optimal length for tumour size and by calculating the treatment time necessary for a given output. The dose given for PII is 2mg/kg of body weight administered by slow intravenous injection. The treatment is typically 630nm light produced by a 15W copper vapour laser pumping a dye laser, for a period of 500s with an energy of 400mW and with a 1.0cm long diffusing ended fibre

Under general anaesthesia the patient is bronchoscoped using a Negus type or Moghissi - Jessop rigid bronchoscope placed in the trachea. This principally is to enable positive pressure ventilation through the venturi port using a jet ventilator or hand operated injector. This also facilitates suction and debridement. The flexible fiberoptic bronchoscope is then introduced through the rigid instrument already in place in the trachea thus allowing visualisation of the optical fibre, which is introduced through the biopsy channel. The optical fibre and its attached diffuser is placed into the tumour for interstitial treatment or over the area for intraluminal surface irradiation. On termination of treatment initial debridement of the bronchus is carried out. One week later the patient is rebronchoscoped for the purpose of further debridement of the bronchial tree. Sometimes necrotic tumour material together with very thick secretions and fibrin form a relatively large size mass requiring the use of a biopsy or foreign body removal

forceps for its disposal. All PDT is carried out in the operating theatre where the patient is monitored throughout the procedure. Assessments are made at one week, one month, three months and six months and then six monthly intervals.

Solar photosensitivity

Although most patients can be safely exposed to moderate sunlight after 1 month, solar photosensitivity in patients injected with Hpd or PII can last for 9 months. Patients have been severely burnt through their clothes after 8 weeks of one injection of PII when exposed to the noon sun for 1h.⁷

Photobleaching

It had been assumed that porphyrin was photochemically stable during treatment and could be activated indefinitely to produce the desired therapeutic effect. It has been demonstrated the possible photooxidation of Hpd in cells treated in culture.² A photochemical change during treatment can be monitored both by loss in tissue fluorescence and loss of extractable porphyrin from the tissue. This photobleaching process occurs concurrent with the cellular inactivation and tissue damage due to the photodynamic process and can be exploited to protect normal tissue during PDT. The photobleaching effect has not been studied in vivo during treatment. Tissue samples have been taken before and after PDT treatment and confirm that photobleaching of the photosensitiser does occur, but to what effect on the treatment is unknown. The absorption of light by the photosensitiser is an essential but unknown factor during

treatment. The amount of light supplied, the photo bleaching process of the photosensitiser and tissue type will all effect the distance the light travels and hence the amount of PDT activated destruction.

2.6 Chemistry of Heamatoporphyrin Derivative

A chromophore compound, such as porphyrin, that is capable of causing light induced reactions in molecules that do not absorb light may be called a photosensitiser. Porphyrin fluorescence in tumour tissue was first achieved when red fluorescence from experimental animal sarcomas exposed to light was observed.¹

Numerous porphyrins have been tested as *in vivo* photosensitisers of experimental animal tumours. Lipson et. al.⁸ while seeking to improve the tumour localising characteristics of haematoporphyrin (Hp), developed haematoporphyrin derivative (Hpd). Hpd is a mixture of compounds obtained by reacting Hp with acetic acid in the presence of sulphuric acid. Hp in turn is obtained from the haemoglobin of natural blood. Hpd has superior localisation and photosensitising properties both *in vitro* and *in vivo* compared with the parent Hp.

Since Hpd is a complex mixture of porphyrins, models which treat this material as a single compound are incomplete. Because of the complex nature of Hpd, it is not always clear which components of the product are responsible for cellular photosensitisation. Tumour localising contaminants may therefore be responsible for the reported capacity of Hpd to photosensitise tumour cells in culture and in human tumours.⁹

In 1981 Dougherty¹⁰ separated HpD and identified a new component of the mixture representing approximately 50% of the mixture, this was called Diheamatoporphyrin ether (DHE) as shown in figure 2.1. It has a strong tendency to self-associate and it is this that may be responsible for long periods of retention of HpD and DHE in tumours. Photofrin[®] II (PII) is the commercial name for a mixture enriched in DHE.

Photosensitisers such as Hp, HpD and PII possess absorption spectra that make them excellent *in vitro* photosensitisers but they are only moderately effective *in vivo* photosensitisers. These chromophores have an intense absorption band between 400 and 630 nm.¹¹ The evaluation of porphyrin photosensitisation in solution and in cells is that they can utilise light throughout the visible light spectrum. Unfortunately *in vivo* and clinical applications of PDT using porphyrins must utilise the wavelength of 630nm, corresponding to the weakest porphyrin absorption band as seen in figure 2.2. This is due to the absorption band of haemoglobin being greater than that of the porphyrin absorption band except at 630nm.

The optical penetration depth in tissue i.e. depth at which light intensity is reduced to 37% of its initial value is approximately 2.5 - 4.5 mm for 630 nm light.¹² The optical penetration depth for human lung tissue has been reported to be from 0.2mm to 2mm and is given in Table 5.1 later in this thesis. Depending on different theoretical models and experimental procedures used the optical penetration depth for *in vitro* lung tissue samples will rarely be the same, hence an *in vivo* value for the optical penetration depth is required.

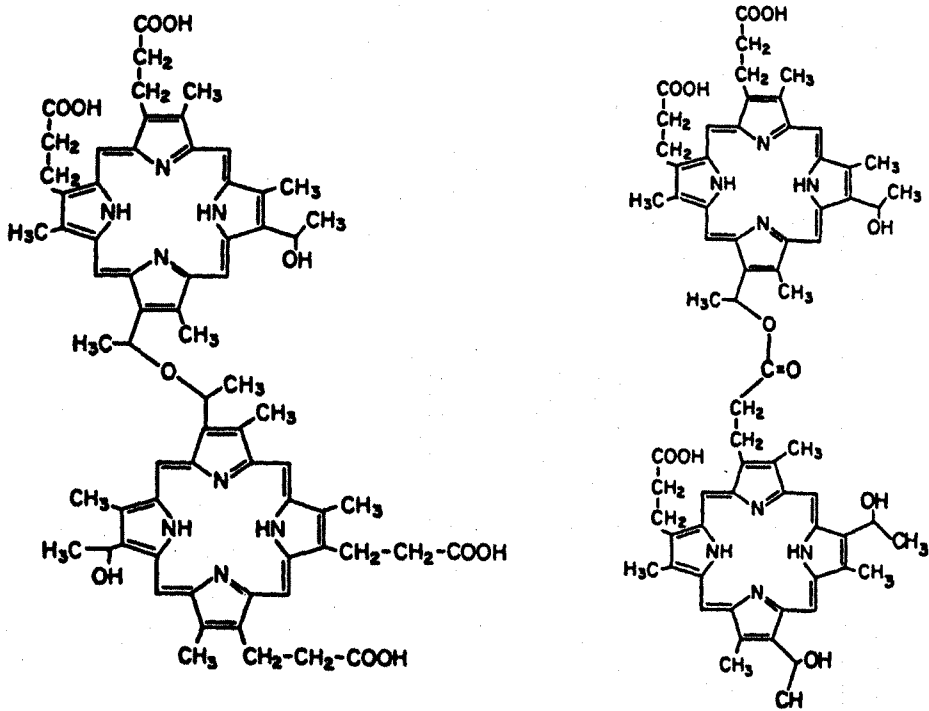


Figure 2.1 Dihaematoporphyrin ester (left) and ether (right)²

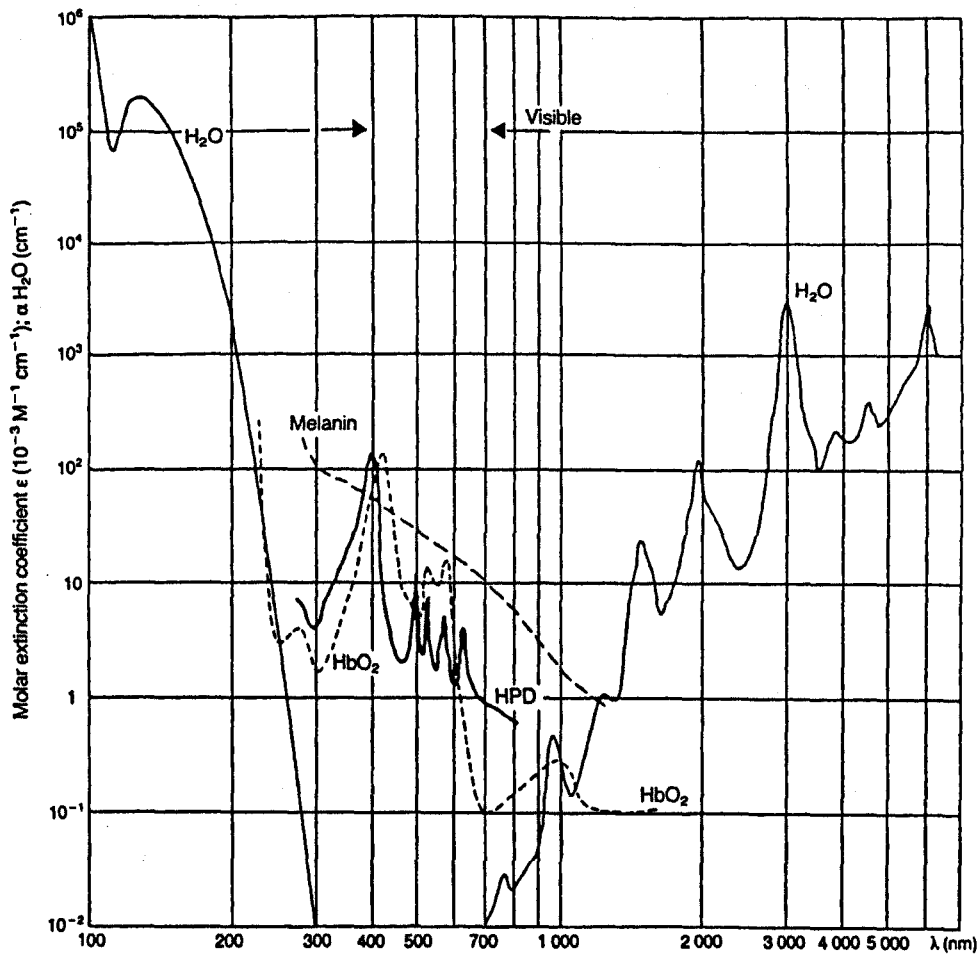


Figure 2.2 Absorption coefficient spectrum of water and haemoglobin (HbO_2), melanin and haematoporphyrin derivative (HPD)¹¹

Second generation photosensitisers offer potential advantages over PII including chemical purity, enhanced tumour to normal tissue selectivity and major absorption bands at wavelengths greater than 650nm. The greater the wavelength the further the light will travel through the tissue due to the absorption band of haemoglobin decreasing with increasing wavelength. Unfortunately from approximately 700nm the absorption band of water increases with increased wavelength. However there is a window for future photosensitisers having their absorption bands between 700nm – 900nm as seen in figure 2.2.

2.7 Singlet Oxygen

The most important common feature of all sensitisers is the possibility that these compounds can transform absorbed light energy into chemical energy. Most photosensitisers currently used, are organic dyes and therefore they exhibit the usual electronic structure of singlet states (total electron spin momentum $S=0$) and triplet states ($S=1$) where the triplet energy is smaller than the corresponding excited singlet state as in figure 2.3. Absorption of light results in formation of excited singlet states followed by the formally forbidden intersystem crossing to triplet states.¹³ These result in intermolecular transfer reactions and ultimately culminate in the release of highly reactive cytotoxic species. Porphyrin sensitised photodamage seems to be mediated mainly by singlet oxygen which has a lifetime and diffusion distance in a cellular environment limited by its reactivity.¹⁴

Each dielectric state is divided into a large number of vibrational states. The excited triplet state is generally endowed with the greatest reactivity due to its spin

Activation Mechanism of HpD

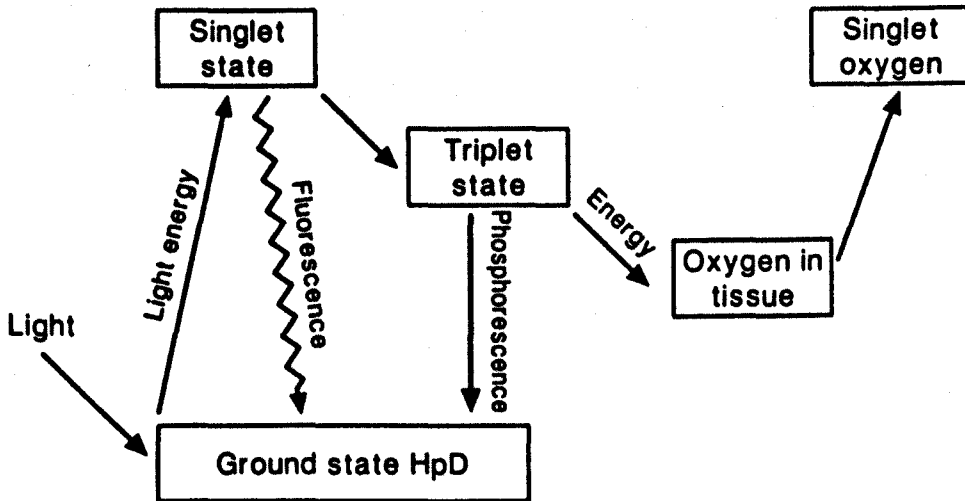


Figure 2.3 Mechanism of Activation of HpD¹⁶

configuration and its long fluorescence lifetime of 1ms - 1s compared to the singlet state of only 0.1 - 100ns. This is one of the reasons why energy transfer can take place from the triplet state to other molecules.¹⁵

In the presence of oxygen two competing reactions of the excited sensitiser can occur. These processes are called Type I and Type II reactions as in figure 2.4. An excited sensitiser state (S*) can either react with the substrate or solvent (Type I) or with oxygen (Type II), this is the experimental definition of the two processes.¹⁶

The Type I reaction results in either a hydrogen atom or electron transfer yielding radicals, or radical ions giving rise to a wide variety of possible further reactions.

Type II reaction is the absorption of a photon of light which will excite the porphyrin molecule to an excited and short lived singlet state and emit light in the form of fluorescence. Studies have shown that the most effective photosensitisers will undergo intersystem crossing from the excited singlet state to the more stable and longer lived triplet state of the molecule.

Moan¹⁷ has estimated that the diffusion distance in cells to be about 0.1 μ m. Therefore cell damage mediated by singlet oxygen will occur close to its site of generation and can affect virtually all cellular and molecular components due to its wide and varied sensitiser distribution within the cells.

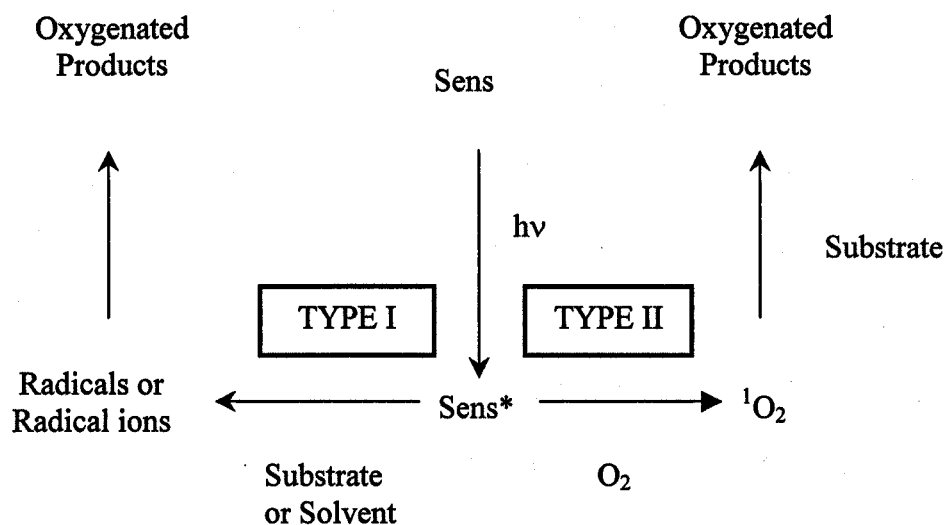


Figure 2.4 Type I and Type II Photosensitised Oxidation reactions¹⁹

2.8 Sensitiser Distribution in Cells and Tissues

The relatively high uptake and long retention of Hpd and similar photosensitisers in tumours is the basis of PDT and the first step towards this treatment is the delivery of photosensitiser to the target tissue. The photodestruction of the sensitiser during PDT is shown to result in an upper limit of the photodynamic dose which can be delivered by the laser. This limit results in the opportunity to make total photodynamic dose uniform to considerable depths 1 - 2 cm. The existence of thresholds for permanent tissue damage affords protection of normal tissue from the large light doses required to achieve this limiting dose deep in the tissue. The differential therapeutic effect also depends upon allowing a time interval for the injected material to clear from the circulation and the normal tissue. The time interval between injection and treatment ranges from 12- 72 hours.¹⁸

Most sensitisers studied to date are distributed to and retained by normal and neoplastic tissues. What varies considerably between sensitisers are the time intervals between administration and peak sensitiser tissue levels and sensitiser retention in tissues. 48h after administration of an injection of PII into a human, the photosensitiser had cleared significantly in normal tissue while about 30% of the sensitiser was still present in the lung 75 days after drug administration.¹⁹

Tissue uptake of sensitisers has been well analysed, however the sensitiser distribution within the tumour tissue has not been well defined. There is much speculation on the mechanism of tumour retention and accumulation of photosensitisers. However, it is

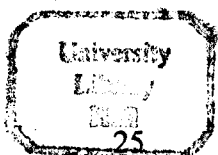
well established that the selectivity of tumour targeting by most photosensitisers varies for different tissues and is often unpredictable.²⁰

The pH in tumours is low compared with the pH in surrounding healthy tissue. Cells take up more of the porphyrins at low pH than at normal tissue pH.²¹ This low pH in tumours may contribute to the selective porphyrin phototherapy. Results also show that Hpd localises in cells by spontaneous diffusion process and then are distributed to lipophilic sites within the cell.²² Another factor for photosensitiser localisation in tumours is simple pooling of the sensitiser due to leaky vasculature and poor lymphatic drainage.

2.9 Molecular and Cellular Effects

Multiple processes appear to be involved in PDT mediated tumour necrosis. Pharmacological and photosensitising responses associated with PDT on neoplastic cells, microvasculature, and on circulating components of the blood have been documented.²³

Despite the work done in well defined cell culture systems the relative contribution of the extracellular and intracellular Hpd to the photodestruction of tumour tissue is still unknown. It is questionable how relevant in vitro studies are since the in vivo physiological milieu of the tumour cell such as blood supply, pH, oxygen, tension, temperature and serum content of the medium immediately surrounding the cell obviously will be important.²⁴



The significance of direct tumour cell death i.e. plasma membrane and organelle damage in tumour destruction remains unclear. It is possible that some direct tumour cell death precedes and induces vessel damage. Damage to blood vessels during and after PDT is marked by two processes. Vessel constriction and platelet aggregation occur very early during light treatment. Fluid and macromolecular leakage occurs in vessels shortly after the completion of light treatment and produces tissue oedema. These events contribute to blood flow stasis and produce regional tissue hypoxia. The destruction of tumour cells is also believed to be a result of this hypoxia and the accompanying deprivation of nutrients. The mechanisms that produce vessel damage remain largely unknown.²⁵

Cells repeatedly treated with PDT can become more resistance to subsequent treatments.²⁶ This resistance is not due to reduced uptake of PII. Cells of similar origin may exhibit differences in sensitivity towards PDT, which again are not due to differences in cellular uptake of the sensitiser.

There are three main targets of PDT, cell membranes, organelles and chromosomes (DNA).

Membrane damage

The membrane environment differs from the surrounding medium not only in polarity, water content and dielectric constant but membranes are heterogeneous structures. Membranes are present at a variety of domains with which sensitisers can associate and from which they can act²⁷. Membrane photomodification has been repeatedly identified as a critical target leading to cell killing or inactivation. This is true not only for the

plasma membrane but also for membranes of intracellular organelles such as mitochondria and lysosomes. The phenomenon appears to be ubiquitous.

After irradiation of PDT, the outer cell membrane swells and blebs are formed which can be seen by an ordinary microscope. This type of damage can be repaired provided the damage is not too severe but usually cells will disrupt.²⁸ As seen by biochemical methods potassium is lost. In addition, certain forms of glucose are inhibited as well as various strains of amino acids after irradiation.²⁹ Membrane damage is much more important after one hour incubation with HPD than after twelve to eighteen hours. With increasing incubation time the porphyrin gradually reaches more sensitive sites in the cells therefore outer cell membrane damage is rather unimportant for cell inactivation over longer periods.³⁰

Cellular Effects

At the cellular level, the mechanism of action that produces cytotoxicity has not been totally elucidated. Organelles such as lysosomes and the nucleus were shown to be damaged by HPD photosensitisation but not to such an extent as mitochondria damage.³¹ This effect of porphyrin photosensitisation on cells is largely localised to membranous structures and most studies emphasise the importance of protein damage in the alteration of the membrane function.

The photosensitisation of mitochondria was greatest 24 -72 hours after injection of the sensitiser. At those times there remained some photosensitisation of the plasma membrane of tumour cells and within the mitochondrion.³² However most

photosensitiser was inner membrane localised, less was in the outer membrane and little or none found in the intermembrane space.³³ Permeation of lysosomal membranes is also a primary step of porphyrin photosensitisation in cells and leads to the conclusion that protein inactivation is involved. This can take place at very low fluence rates and under certain conditions might be a determining factor in cell apoptosis.³⁴

Enzymes

The deleterious effects of several photosensitised reactions on living organisms can be explained in terms of photochemical induced modifications of DNA. Low doses of light given to Hpd labelled cells inhibit their proliferation for a few hours after the treatment.³⁵ However provided the light dose is not too large the growth rate returns to normal. This may indicate damage to the mitotic (cell division) apparatus. Processes involving DNA itself are also affected by PDT treatment although the nucleus contains very small amounts of Hpd. The synthesis of DNA is very sensitive to PDT with only low doses of Hpd and light reducing the DNA synthesis almost to zero, with no effect on cell survival.³⁶

Vascular effects

PDT acts by destroying vasculature, which reduces the supply of nutrients and oxygen. Treatment has a selective effect on tumour tissue even in regions of the tumour where the photosensitiser concentration is similar to that in the adjacent normal tissue. Vessel constriction and stasis have been observed within the first minutes of PDT.³⁷ It was

speculated that tumour cure was dependent on vascular damage rather than on direct tumour cell death. Increase in tumour interstitial pressure, an alternative measure of vessel permeability has been observed after PDT.³⁸

The time interval between initiation of damage and vascular occlusion may vary from tumour to tumour and with different sensitisers but eventual vessel occlusion seems to be a general phenomenon accompanying PDT. The major determinant for vascular photosensitivity appears to be the level of circulating photosensitiser.³⁹

2.10 Hyperthermia

Optimal delivery of light to the tumour is of paramount importance in PDT and the most effective way of delivering laser light to the tumour tissue is through an optical fibre. Fibres that are used to deliver light to human lung tumours have been observed to have congealed blood on the fibre tip after PDT.

The optical power used during PDT is one to two orders of magnitude lower than the power utilised in laser surgery (10 - 30 W). Nevertheless, since the time exposure in PDT is long compared to the times scale required for thermal diffusion the heated region will be large. The depth of the therapy region is limited by the absorption of light in tissue. A predominant part of the optical energy is converted to heat through this absorption. The thermal properties of living tissue are governed by three different mechanisms, the ability to transport heat by thermal conduction, the ability to store heat and finally the ability to transport heat through the vascular system.

The blood that flows into a given region at arterial blood temperature will rapidly obtain the local temperature once transported through the capillary system. The blood flowing out of a locally heated region thus carries a thermal energy stored by the specific heat of the blood. Blood flow in tumours varies considerably among different tumour types. Even in the same tumour the distribution of vasculature and blood flow is quite diffuse. The capacity of tumour blood flow to increase upon heating appears to be rather limited compared to normal tissue blood flow. Consequently, heat dissipation by blood flow in tumours is slower than that in normal tissue and thus the tumour temperature rises higher than that in normal tissue during heating. Preferential heating of tumours may not always be achieved, as the blood perfusion in some tumours remains greater than in the surrounding normal tissue.⁴⁰

Upon heating, the intratumour environment becomes acidic, hypoxic and nutritionally deprived due to vascular damage. An acidic and nutritionally deprived environment greatly increases the thermosensitivity of tissue and inhibits the recovery of tissue from thermal damage. Assuming that vascular damage is one major mode of action in PDT treatment the rationale for using a combination of PDT followed by hyperthermia treatments is apparent.⁴¹

Most malignant cells are found to be more sensitive to heat than normal cells. This differential cell kill is partly lost for temperatures above 45°C and all cells are killed rapidly in temperatures exceeding 50°C.⁴² Table 2.1 summarises the temperature ranges of successive transformations. At about 45°C tissue retraction related to conformational changes and membrane alterations occurs. Beyond 60°C is the range of protein

Temperature	Effects on tissue
43-45 °C	Conformational changes Retraction
50°C	Hyperthermia (cell mortality)
60°C	Reduction of enzyme activity Protein denaturation
80°C	Coagulation Membrane permeabilisation
100°C	Carbonisation Vaporisation and ablation

**Table 2.1 Physical principles of photothermal processes:
Conversion of electromagnetic radiation into heat increases
the tissue temperature.¹¹**

denaturation, resulting in tissue coagulation. The temperature limit at which tissues become carbonised is about 80°C and vaporisation occurs beyond 100°C.

Hyperthermia is not required for PDT toxicity and substantial cell destruction can occur in the absence of increased tissue temperature.

2.10 References

1. Dougherty T J, *Onc / Hem.* **2** (2),83 (1984)
2. Moan J, *LIMS* **1**, 5 (1986)
3. Lipson R L, Gray M J, Baldes E J, *Proc 9th int. Cancer Congr* 1966,393
4. Dougherty T J, *J Nat. Can. inst.* **55**, 115 (1975)
5. Hayata Y, Kato h, Konaka C, Ono J, Matsushima Y, Yoneyama K, Nishimiay K, *Chest* **82**, 10 (1982)
6. Moghissi K, Parsons R, Dixon K, *LIMS* **8**, 269 (1993)
7. Mang T S, Dougherty T J, Potter WR, Boyle DG, Somu S, Moan J, *Photochem. Photobiol.* **45** (4), 501 (1987)
8. Lipson R L, Baldes E J, Olsen A M, *J. Thorac. Cardiovasc. Surg.* **42**, 623 (1961)
9. Jom G, Tomio L, Reddi E, Rossi E, Corti L, Zorrat P L, Calzavana F, *British J. of Cancer* **48**, 307 (1983)
10. Dougherty T J, *Photochem. Photobiol.* **38**, 377 (1983)
11. Boulnois J L, *LIMS* **1**, 47 (1986)
12. Wilson B C, In Ben Hur E Rosenthal I eds *Photomedicine* vol 2 CRC Press **27** 177 (1987)
13. Patterson M, *Photochem. Photobiol. B:(5)*, 69 (1990)
14. Weishaupt K R, Gomer C J, Dougherty T J, *Cancer Res.* **36**, 2326 (1976)
15. Schenkk G, *Ind. Eng. Chem.* **55**, 40 (1963)
16. Foote C S, *Photochem. Photobiol.* **54** (5), 659 (1991)
17. Moan J, *Photochem. Photobiol. B:* **6**, 343(1990)
18. Potter W R, Mang S, Dougherty T J, *Photochem. Photobiol.* **46** (1), 97 (1987)

19. Photodynamic Therapy, Henderson B W and Dougherty T J, New York, Marcell Dekker, (1992)
20. Richter A M, Cenrutisola S, Sternburg E D, Polphin D, Levy J G, Photochem. Photobiol. B 5, 231 (1990)
21. Moan J, Cancer lett. 9, 327 (1980)
22. Shulok J R, Wade M H, Lin C W, Photochem. Photobiol. 51 (4), 451 (1990)
23. Kessel D, Photochem. Photobiol. 44 (4), 489 (1986)
24. Nelson J S, Lian L H, Berns M W, Photochem. Photobiol. 46 (5), 829 (1987)
25. Chaudhuri K, Keck R W, Selman S H, Photochem. Photobiol. 46 (5), 823 (1987)
26. Moan J, Berg K, Photochem. Photobiol. 55 (6), 931 (1992)
27. Valenzano D P, Photochem. Photobiol. 46 (1), 147 (1987)
28. Moan J, Johannessen J V and Christensen T, Am. J. Pathol. 109, 184 (1982)
29. Porphyrins in Tumor Phototherapy, Andreoni A, Cubeddy R (eds), Dubbelman T, New York, Plenum 167 (1984)
30. Kosaki, Mie. Med. J. 1, 55 (1956)
31. Moan J, J. Cancer 39, 394 (1979)
32. Gomer S J and Rucder N, Cancer Res. 43, 2622 (1983)
33. Hilf R, Gibson S L, Penney D P, Ceckler T L, Bryant R G, Photochem. Photobiol. 46, 809 (1987)
34. Reyftmann J P Kohen E, Morliere P, Santus R, Koher C, Mangel W F, Dubertket L, Hirshberg J, Photochem. Photobiol. 44 (4), 461 (1986)
35. ChristensenT, Br. J. Cancer 44, 433 (1981)
36. Bugelski P J, Porter C W and Dougherty T J, Cancer Res. 41, 4606 (1981)

37. Star W M, Marijnissen H, Vandenbergblok A E, Versteeg J A C, Franken K A P, Reinhold H J, *Cancer Res.* **46**, 2532 (1986)
38. Fingar V H, Wieman T J, Wiehle S A, Cerrito P B, *Cancer Res.* **52**, 4914 (1992)
39. Bellnier D A, Dougherty T J, *Photochem. Photobiol.* **49**, 369 (1989)
40. Song C W, *Cancer Res. Supl.* **44**, 4721s (1984)
41. Mattiello J, Hetzel F, Vandenheede L, *Photochem Photobiol.* **46** 873 (1987)
42. Svaasand L O, Dougherty T J, *Med. Phys* **10**, 1 (1983).

3 Derivation of the diffusion approximation from transfer theory

3.1 Introduction

Human tissue is an optically turbid media; when photons propagate through such tissue they are scattered and absorbed by the particles in the tissue. For the progress of photodynamic therapy and laser surgery of diseased tissues to be enhanced, accurate measurements of the optical properties of human tissue are required. Mathematical descriptions of light absorption and scattering are important in understanding these interactions.

A mathematical description of the propagation and scattering characteristics of light can be formulated from two different approaches; analytical theory and transport theory¹. The analytical theory starts with Maxwell's equations taking into account the statistical nature of the medium and wave propagation. This is the most fundamental approach but the drawback is the mathematical complexities involved². Transport theory deals with the transport of energy through a medium containing particles. It is assumed in transport theory that there is no correlation between fields and therefore the addition of powers rather than the addition of fields holds. The basic differential equation which arises is called the equation of transfer and is equivalent to Maxwell - Boltzmann collision equation used in kinetic theory of gases.³ The general solution is not known and accurate solutions are limited to simple conditions or slab geometries.

A frequently used approximation for the radiative transfer equation is described by the diffusion approximation.¹ It is with this approximation that an expression concerning the diffuse nature of the fluxes inside a random medium may be derived as a solution to the equation of transport. The diffusion approximation has been widely used for describing light propagation in biological tissue where scattering dominates over absorption.

Experimental determination of the optical properties of tissue requires not only the solution to the transport equation in the experimental geometry but also suitable relations between this solution and the optical properties

3.2 Radiative Transfer Equation Derivation

If a medium consists of random particles which vary randomly in time and space, then the waves in such a medium must vary randomly in amplitude and phase. The photons are assumed to be either scattered elastically by particles of the medium or absorbed and that the light is taken to be unpolarised.⁴ Following Ishimaru¹ the wave propagation and scattering characterisations must be described in two steps. The scattering and absorption characteristics of a single particle scatterer are determined and the contributions from many scatterers are analysed.

Cross-sections and Scattering Amplitude

A particle in space is illuminated by an incident plane wave E_i in the direction z . The scattered field $E_s(z)$ is observed in the direction defined by a unit vector \hat{o} at a distance R as in figure 3.1.

When the distance $R < D^2/\lambda$ (D being the typical diameter of the particle) the field E_s has complicated amplitude and phase variations due to the geometry of the particle causing interference. However when the observation point is said to be in the far field ie $R > D^2/\lambda$ it is assumed the scattered field behaves as a spherical wave. The scattering amplitude $f(\hat{o}, \hat{i})$ can now be defined and represents the amplitude, phase and polarisation of the scattered wave in the far field in the direction \hat{o} .

Consider an incident power flux density S_i on a particle, then the scattered power flux density is defined as S_s at a distance R in the direction \hat{o} . The differential scattering cross section is defined as

$$\sigma_d(\hat{o}, \hat{i}) = \lim_{R \rightarrow \infty} \left[\frac{R^2 S_s}{S_i} \right] = |f(\hat{o}, \hat{i})|^2 = \frac{\sigma_t}{4\pi} p(\hat{o}, \hat{i}) \quad (3.1)$$

where σ_t is the total cross-section and $p(\hat{o}, \hat{i})$ the probability function called the phase function which will be dealt with later. The differential cross section may be defined physically as the cross section of a particle which would cause the observed scattered power flux density in the direction of \hat{o} to be extended uniformly over one steradian of solid angle about \hat{o}

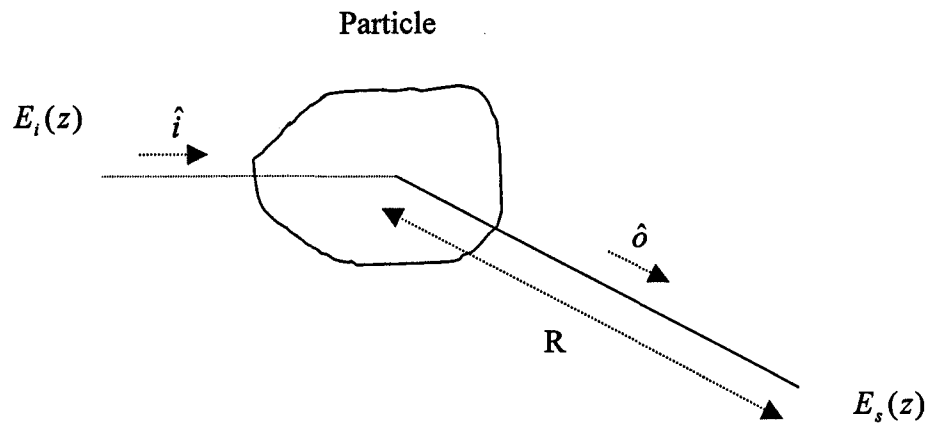


Figure 3.1 Plane Wave $E_i(z)$ incident upon a particle and a scattered field $E_s(z)$ observed in the direction $\hat{\theta}$ at a distance R .

Consider now the total observed scattered power at all angles surrounding the particle. The cross section of a particle, which would produce this amount of scattering, is called the scattering cross section σ_s

$$\sigma_s = \int_{4\pi} \sigma_d d\omega = \int_{4\pi} |f(\hat{o}, \hat{i})|^2 d\omega = \frac{\sigma_t}{4\pi} \int_{4\pi} p(\hat{o}, \hat{i}) d\omega. \quad (3.2)$$

$d\omega$ is the differential solid angle

Consider the total power absorbed by a particle. The cross section of a particle which would correspond to this much power is called the absorption cross section, σ_a .

The total cross section σ_t is the sum of the absorption and scattering cross sections defined as

$$\sigma_t = \sigma_s + \sigma_a \quad (3.3)$$

Specific Intensity

Specific intensity is the most important and fundamental property to be defined in the radiative transfer equation since it deals with the propagation of intensities. An intensity $I(z)$ can be defined as the flow of wave energy at a point z in a random medium whose frequency, phase and amplitude of the wave undergo some random variation in time. Hence, the magnitude and direction of its power flux density vector will vary continuously in time. The average power flux density within a unit solid angle in a direction given by a unit vector \hat{s} is $I(z, \hat{s})$ as in figure 3.2; this quantity is called the specific intensity or radiance and is measured in $\text{Wm}^{-2}\text{sr}^{-1}$.

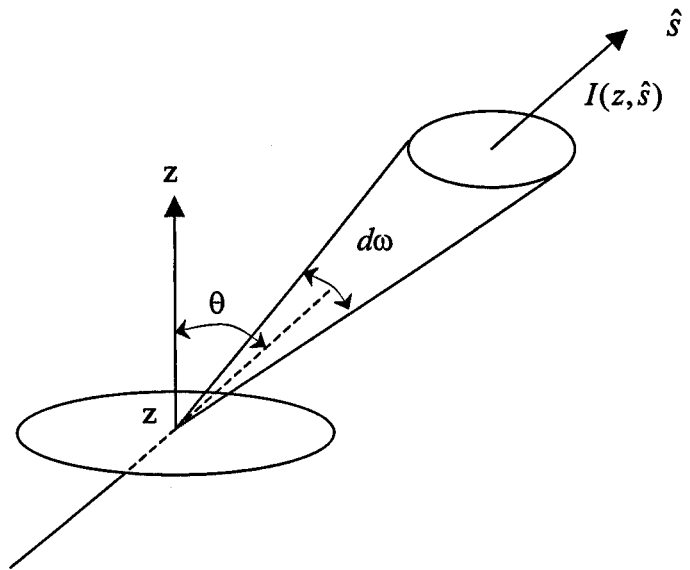


Figure 3.2 Specific intensity $I(z, \hat{s})$ in a random medium.

Consider the specific intensity at a plane boundary between two media with refractive indices n_1 and n_2 as in figure 3.3. The amplitude reflection coefficient R and amplitude transmission coefficient T for a plane wave incident on a plane boundary are given by

$$R = \frac{E_r}{E_i}$$

$$T = \frac{E_t}{E_i}$$
(3.4)

When the electric fields (E) are polarised in the plane of incidence $R_{||}$ and $T_{||}$ or when the electric fields are polarised perpendicular to the plane of incidence R_{\perp} and T_{\perp} the coefficients become

$$R_{||} = \frac{n_1 \cos \theta_2 - n_2 \cos \theta_1}{n_1 \cos \theta_2 + n_2 \cos \theta_1}, \quad T_{||} = \frac{2n_1 \cos \theta_1}{n_2 \cos \theta_1 + n_1 \cos \theta_2}$$

$$R_{\perp} = \frac{n_1 \cos \theta_1 - n_2 \cos \theta_2}{n_1 \cos \theta_1 + n_2 \cos \theta_2}, \quad T_{\perp} = \frac{2n_1 \cos \theta_1}{n_1 \cos \theta_1 + n_2 \cos \theta_2}$$
(3.5)

Where θ_1 is the angle of incidence and reflection and θ_2 is the angle at which the transmitted wave passes through the medium with refractive index n_2 . The reflected specific intensity I_r is related to the incident specific intensity I_i through

$$I_r = |R|^2 I_i$$
(3.6)

where R = either $R_{||}$ or R_{\perp} depending on the polarisation. If the wave is completely unpolarised then

$$|R|^2 = \frac{1}{2} \left(|R_{||}|^2 + |R_{\perp}|^2 \right)$$
(3.7)

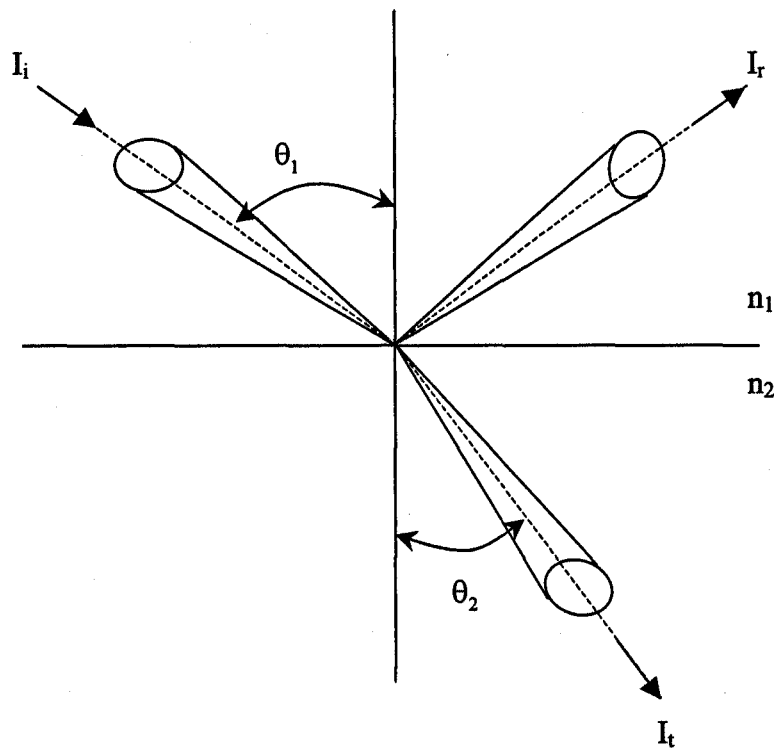


Figure 3.3 Specific intensities at a plane boundary between two homogeneous media.

A specific intensity $I(z, \hat{s})$ incident upon a cylindrical elementary volume with unit cross section and length ds which contains ρds particles, where ρ is the number of particles in a unit volume and is called the number density, see figure 3.4. Each particle absorbs a power $\sigma_a I$ and scatters a power $\sigma_s I$ therefore the decrease in the specific intensity over the volume is

$$\begin{aligned} dI(z, \hat{s}) &= -\rho(\sigma_a + \sigma_s)I(z, \hat{s})ds \\ &= -\rho(\sigma_t)I(z, \hat{s})ds \end{aligned} \tag{3.8}$$

The rate of change through this volume is expressed as

$$\frac{dI(z, \hat{s})}{ds} = -\rho(\sigma_t)I(z, \hat{s}) \tag{3.9}$$

This rate of change refers to $dI(z, \hat{s})$ by a section through the volume giving the attenuation through a thin slice at the point z , inclined in the direction \hat{s} .

This is called the Loss Term.

The specific intensity also increases due to a portion of the intensity incident on this volume from other directions \hat{s}' scattered into the direction \hat{s} and is added to the intensity $I(z, \hat{s})$.

Consider a wave incident in the direction \hat{s} on a particle in a volume ds giving the incident flux density through a small solid angle $d\omega'$ as

$$S_i = I(z, \hat{s}')d\omega \tag{3.10}$$

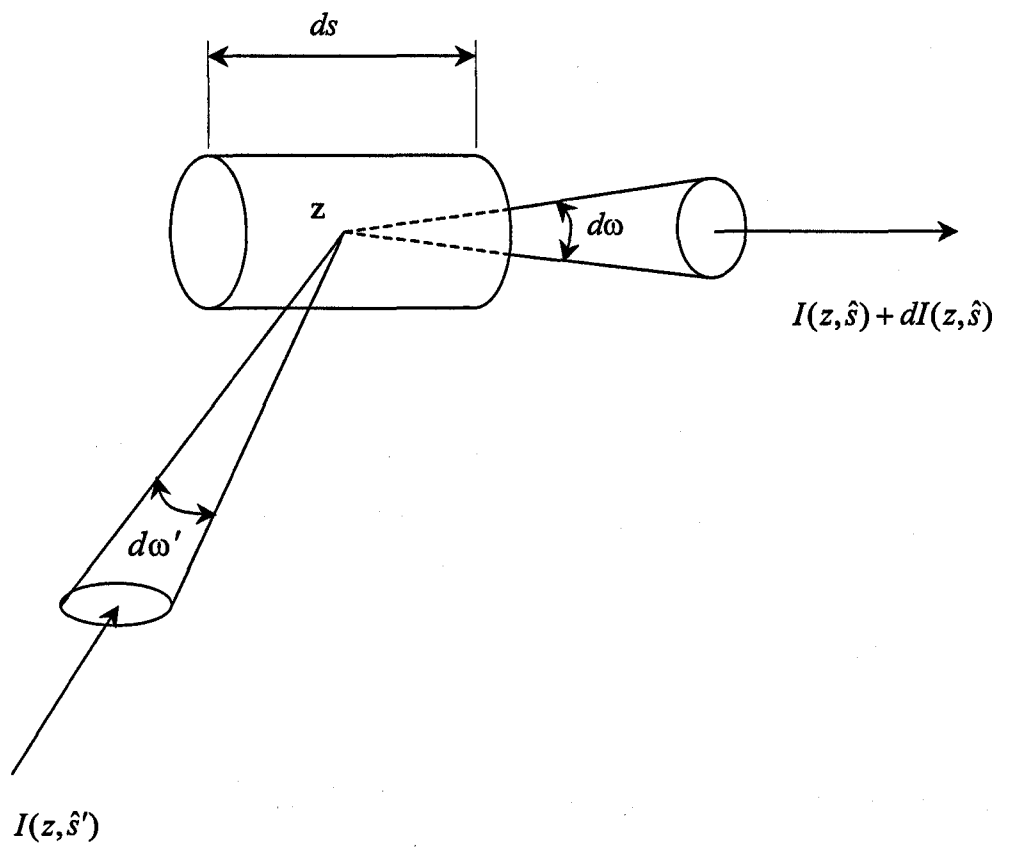


Figure 3.4 Specific intensity scattering incident upon a elementary volume dz

The power flux density of the wave scattered by a single particle S_s in the direction \hat{s} at a distance R from the particle is given by

$$S_s = \left[\frac{|f(\hat{s}, \hat{s}')|^2}{R^2} \right] S_i \quad (3.11)$$

where $f(\hat{s}, \hat{s}')$ is the scattering amplitude

The scattered specific intensity in the direction \hat{s} due to S_i is therefore

$$\begin{aligned} S_s R^2 &= |f(\hat{s}, \hat{s}')|^2 S_i \\ &= |f(\hat{s}, \hat{s}')|^2 I(z, \hat{s}') d\omega' \end{aligned} \quad (3.12)$$

The incident flux from all directions of \hat{s}' is now taken into account and the specific intensity scattered into the direction \hat{s} by ρds particles in the volume ds is given by

$$\int_{4\pi} \rho ds |f(\hat{s}, \hat{s}')|^2 I(z, \hat{s}') d\omega' \quad (3.13)$$

where the integration over all ω' is taken to include the contributions from all directions \hat{s}' .

The rate of change in the specific intensity can be written as

$$dI(z, \hat{s}) = \int_{4\pi} \rho d\hat{s} |f(\hat{s}, \hat{s}')|^2 I(z, \hat{s}') d\omega' \quad (3.14)$$

$$\frac{dI(z, \hat{s})}{d\hat{s}} = \int_{4\pi} \rho |f(\hat{s}, \hat{s}')|^2 I(z, \hat{s}') d\omega' \quad (3.15)$$

and the scattering amplitude can be written as before

$$|f(\hat{s}, \hat{s}')|^2 = \frac{\sigma_t}{4\pi} p(\hat{s}, \hat{s}') \quad (3.16)$$

Finally the Gain Term becomes

$$\frac{dI(z, \hat{s})}{d\hat{s}} = \frac{\rho\sigma_t}{4\pi} \int_{4\pi} I(z, \hat{s}') p(\hat{s}, \hat{s}') d\omega' \quad (3.17)$$

and by combining this with equation 3.9 the Equation of Transfer is obtained:

$$\frac{dI(z, \hat{s})}{d\hat{s}} = \frac{\rho\sigma_t}{4\pi} \int_{4\pi} I(z, \hat{s}') p(\hat{s}, \hat{s}') d\omega' - \rho\sigma_t I(z, \hat{s}) \quad (3.18)$$

In this equation: $I(z, \hat{s})$ is the specific intensity in ($\text{Wm}^{-2}\text{sr}^{-1}$) at a point in space z in the direction of the unit vector \hat{s} .

$d\hat{s}$ is an element of volume;

$\rho\sigma_t$ is the attenuation coefficient;

$p(\hat{s}, \hat{s}')$ is the phase function which is the probability for scattering of a photon from the direction \hat{s}' into \hat{s} ;

$d\omega'$ is an element of solid angle about ω' .

The equation of transfer describes the loss of specific intensity due to absorption and scattering out of the volume and the gain due to the scattering into the volume.

3.3 The Diffusion approximation for slab geometry

Slab geometry

The derivation of the diffusion equation from the equation of transfer follows the treatment of Ishimaru¹. There is no general solution to the equation of transfer under all conditions and therefore simplified geometries and models are required⁵. The accuracy of the diffusion equation is affected by the ratio of scattering to absorption, the scattering anisotropy, and the distance from light sources and boundaries.⁶ It is assumed in the diffusion approximation that the diffuse intensity encounters many particles and is scattered almost uniformly in all directions. The angular dependence cannot be constant otherwise the flux would be zero and there would be no net power propagation. The diffuse intensity should therefore have slightly more magnitude in the general direction of net flux flow than in the backward direction.

An accepted way of dealing with the equation of radiative transfer is to adopt the simplified model using slab geometry and applying the diffusion approximation^{5 7}. This rigid geometry allows derivation of a solution to the equation in terms of fluxes within a slab of material, which contains random particles.

For slab geometry a slab of material is assumed to be illuminated by a collimated beam of monochromatic light of infinite diameter, perpendicularly incident upon a parallel homogeneous and isotropic layer of material with thickness d but otherwise unbound. By making the slab infinite across its surface the incident beam and subsequent specific

intensity depends only on the dimension Z representing the direction of flow. The transport equation⁸ can then be written as

$$u \frac{du}{dz} I(z, u) = -\Sigma_t I(z, u) + \frac{\Sigma_t}{2} \int_{-1}^1 I(z, u') P(u, u') du' \quad (3.19)$$

where $I(z, u)$ is the radiance ($\text{Wm}^{-2}\text{sr}^{-1}$); θ is the angle between the direction of propagation and the direction of flow z as shown in figure 3.5 and Σ_t is the attenuation coefficient previously written as $\rho\sigma_t$.

The phase function $P(u, u')$ in sr^{-1} represents the probability that light is scattered from the direction u' into the direction u . The phase function depends on the angle between u and u' only, implying that the scattering particles are randomly distributed. The normalisation condition imposed on the phase function $P(u, u')$ is

$$\frac{1}{2} \int_{-1}^1 P(u, u') du' = \frac{\sigma_s}{\sigma_a + \sigma_s} = W_0 \quad (3.20)$$

which is termed the albedo W_0

Radiance and diffuse intensities

The one-parameter diffusion approximation to the transport equation follows straightforwardly from equation (3.19) with the following assumptions. First; divide the specific intensity into an almost diffuse term and a collimated reduced incident term that depends on the original nature of the incident light.⁹

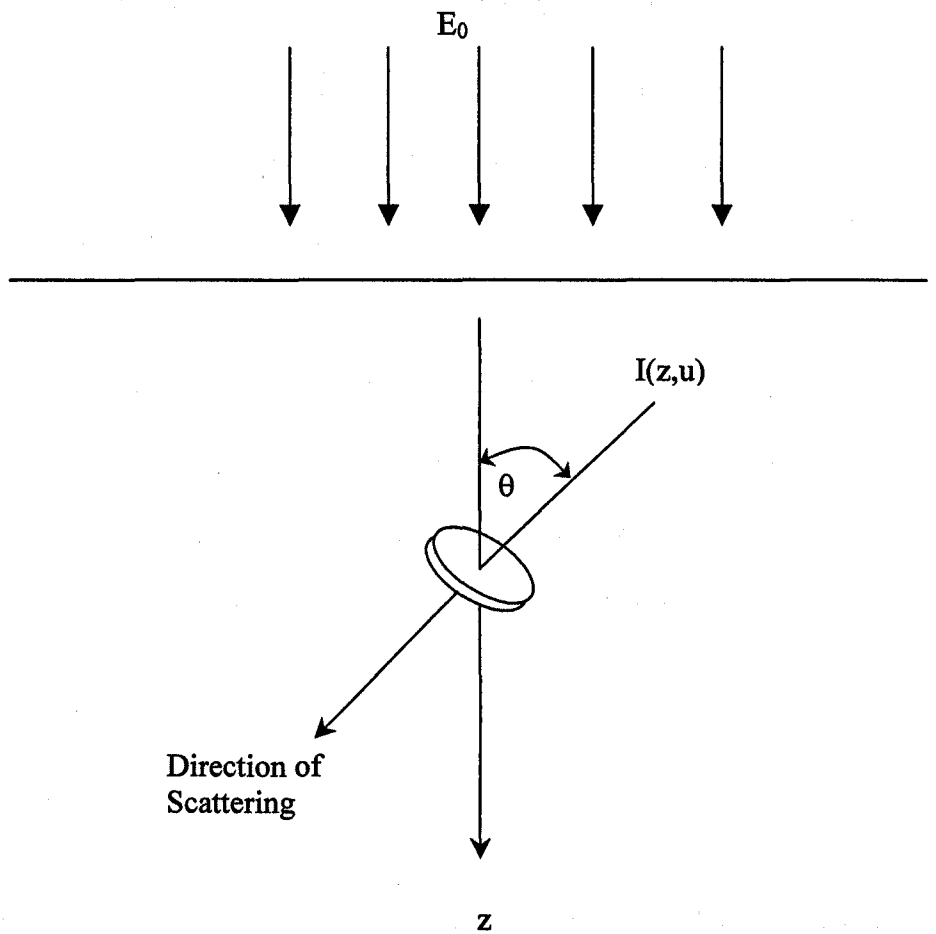


Figure 3.5 Slab of material illuminated by a monochromatic collimated beam with infinite width. Specific intensity $I(z, u)$ is incident upon a volume dz situated within the homogeneous isotropic medium of random particles.

$$I(z, u) = I_d(z, u) + I_r(z, u) \quad (3.21)$$

The diffuse radiance terms $I_d(z, u)$, represents the photons that have been scattered at least once and can be represented exactly by an infinite sum of Legendre Polynomials. $I_r(z, u)$ the reduced part of the incident intensity contains light which has not yet undergone any interaction with the medium.

The reduced intensity part can be easily obtained from the equation of radiative transfer theory. Assume a wave enters a volume V containing many particles the flux incident on the material varies according to the equation of radiative transfer. The part of the flux that decreases due to absorption and scattering is called the reduced incident intensity and satisfies the equation

$$u \frac{dI_r(z, u)}{dz} = -\sum_t I_r(z, u) \quad (3.22)$$

note that the reduced incident intensity can be either collimated or diffuse light depending on the incident beam.

For a collimated beam which is parallel to the reduced intensity $u=1$ (parallel to Z); this is called the collimated incident intensity and

$$1 \cdot \frac{dI_c(z)}{dz} = -\sum_t I_c(z) \quad (3.23)$$

where $I_c(z) = I_r(z, u)$ when $u=1$

This is the collimated rate equation. It has been assumed that there is no contribution to the collimated part due to scattering from the diffuse intensity.

In the derivation of the radiative transfer equation it is assumed that there are no sources. However using the incident beam as a source only describes the scattered light. To overcome this a source term is added to the RHS of the radiative transfer equation. The reduced intensity, which is a loss term for the collimated beam, is now considered as a source term for the diffuse intensity. From Ishimaru¹ the source function is

$$S_r(z, u) = \frac{\sum_t}{2} \int_0^1 P(u, u') I_c(z, u) du' \quad (3.24)$$

In slab geometry $u' = 1$ so

$$S_r(z, u) = \frac{\sum_t}{2} P(u, 1) I_c(z) \quad (3.25)$$

Adding this source function to the radiative transport equation as a gain term gives

$$\begin{aligned} u \frac{dI_d(z, u)}{dz} = & -\sum_t I_d(z, u) + \frac{\sum_t}{2} \int_{-1}^1 I_d(z, u') P(u, u') du' \\ & + \frac{\sum_t}{2} P(u, 1) I_c(z) \end{aligned} \quad (3.26)$$

The equation of radiative transfer is now expressed in collimated and diffuse rate equations (3.23) and (3.26) and are of the form given by Van Gemert⁸.

In the diffusion approximation it is assumed that $I_d(z, u)$ is slightly anisotropic.

Diffusion approximation using Legendre Polynomials

The incident beam can either be included in $I(z, u)$ or treated separately as a source. In the former case $I(z, u)$ consists of a diffuse term and a strongly forward collimated

term. In the diffuse part of the specific intensity it is the phase function which is of interest. The general expression for the phase function is a series expansion in terms of the Legendre Polynomials,¹⁰

$$P(u, u') = \sum_{n=0}^{\infty} W_n P_n(u) P_n(u') \quad (3.27)$$

where $P_n(u)$ is the n th Legendre Polynomial with properties

$$P_0(u) = 1; \quad P_1(u) = u; \quad P_n(u = 1) = 1 \quad (3.28)$$

$$\int_{-1}^1 P_n(u) P_m(u) du = \begin{cases} 2(2n+1)^{-1}, & \text{if } n = m \\ 0 & \text{if } n \neq m \end{cases}$$

The full expansion has $n+1$ terms and the first few are shown in Arkfen¹¹

The diffuse part of the specific intensity can be written

$$I_d(z, u) = \sum_{n=0}^{\infty} I_n(z) P_n(u) \quad (3.29)$$

hence

$$I_d(z, u) = I_0(z) + I_1(z)u + I_2(z) \frac{1}{2}(3u^2 - 1) + \dots \quad (3.30)$$

Taking the first two terms, since approximations of higher orders are neglected, the diffuse intensity can be assumed to be

$$I_d(z, u) = I_0(z) + I_1(z)u \quad (3.31)$$

An alternative name for the diffusion approximation is the P1 approximation. This approximation is valid if $\sigma_a \ll \sigma_s(1-g)$ except near boundaries or sources¹². The first term in equation (3.31) represents a flux, which is perfectly independent of angle and gives no contribution to the total flux. The first contribution to the total flux comes from the P1 term ie $I_1(z)u$. It is assumed that the contributions of higher order terms to the overall solution are small and therefore can be neglected.

Fluxes

In the diffusion approximation, the assumption is made that the diffuse intensity is slightly anisotropic. The diffuse intensity should therefore have slightly more magnitude in the direction of the net flux flow than in the backward direction.

Consider an amount of power dp flowing through a small area da within a solid angle $d\omega$, then

$$\frac{dp}{da} = I(z)d\omega \quad (3.32)$$

where $I(z)$ is the intensity at a point z . The area will depend on the direction from which it is observed,

$$I(z, u) = \frac{dp}{da'} \frac{1}{d\omega} \quad (3.33)$$

where $da' = u da$

$$dp = I(z, u) u da d\omega \quad (3.34)$$

dp is now termed the power flux

Consider the total flux passing through a small area da on a surface A at a point z . This flux is given by integrating dp over a solid angle in the forward direction, ($0 \leq u \leq 1$) and can be written as

$$p = \int I(z, u) u da d\omega = F_+(z) da \quad (3.35)$$

where $F_+(z)$ is the forward diffuse flux density and can be defined as

$$F_+(z) = 2\pi \int_0^1 I(z, u) u du \quad (3.36)$$

Similarly there will be a backward flux density $F_-(z)$ for the flux flowing through da in the backward direction ($-1 \leq u \leq 0$)

$$F_-(z) = 2\pi \int_{-1}^0 I(z, u) u du \quad (3.37)$$

Both F_+ and F_- are net photon energy fluxes in the positive and negative z directions and are measured in Wm^{-2} .

The total flux density can be expressed as the component of the flux density vector $F_d(z)$ in the direction of flow z perpendicular to the surface

$$F_d(z) = F_+(z) - F_-(z) \quad (3.38)$$

Substituting the diffuse intensity equation (3.31) into equation (3.36)

$$F_+(z) = 2\pi \left[\frac{1}{2} I_0(z) + \frac{1}{3} I_1(z) \right] \quad (3.39)$$

A similar approach for the negative flux produces

$$F_-(z) = \pi \left[I_0(z) - \frac{2}{3} I_1(z) \right] \quad (3.40)$$

combining equations (3.39) and (3.40) gives the total flux

$$F_d(z) = \frac{4}{3} \pi I_1(z) \quad (3.41)$$

As before there is a forward and negative flux flowing within the medium, such that $F_+(z)$ is a positive flux travelling in the positive Z direction and $F_-(z)$ is a diffuse negative flux flowing in the negative Z direction. Consider a forward collimated flux at a point z where the reduced collimated intensity $I_c(z)$ is used

$$F_c(z) = 2\pi \int_0^1 u I_c(z) du \quad (3.42)$$

the forward direction is given by the integrals and a delta function that forces the direction of scatter hence the forward collimated flux is defined as

$$F_c(z) = 2\pi I_c(z) \quad (3.43)$$

which is identical to van Gemert.⁸

Space Irradiance

The quantity of interest in light dosimetry is the radiant energy fluence rate, also called the space irradiance.¹³ This is the integral of the specific intensity over all solid angles

and corresponds to the radiant energy flux incident on a small sphere. The space irradiance is expressed as

$$\phi(z) = 2\pi \int_{-1}^1 I(z, u) du \quad (3.44)$$

This is associated with the diffuse specific intensity and hence by using equation (3.31) the diffuse space irradiance becomes

$$\phi_d(z) = 4\pi I_0(z) \quad (3.45)$$

or

$$I_0(z) = \frac{1}{4\pi} \phi_d(z) \quad (3.46)$$

Hence using the total diffuse flux equation (3.41) and equation (3.46) the diffusion equation can be written in terms of the specific intensity

$$I_d(z, u) = \frac{1}{4\pi} \phi_d(z) + \frac{3}{4} \frac{1}{\pi} F_d(z) \quad (3.47)$$

where $I_d(z, u)$ is the diffuse radiance term of the specific intensity; $\phi_d(z)$ is the diffuse space irradiance and $F_d(z)$ is the total diffuse flux.

Diffusion equation derivation

Having now established the radiative transfer equation and a solution in the form of energy fluence rate and diffuse fluxes, it is possible to derive an equation representing the diffuse nature of the fluxes. The final steps for obtaining a solution of the diffuse radiative transfer equation is firstly to integrate over u from -1 to 1 (representing the volume energy balance) and secondly to multiply it by u and integrate again over u from -1 to 1 (representing the volume flux balance). Taking the diffuse equation for radiative transfer equation (3.31) and integrating between 1 and -1 over u .

$$\begin{aligned} \frac{d}{dz} \int_{-1}^1 I_d(z, u) u du &= -\sum_t \int_{-1}^1 I_d(z, u) du + \frac{\sum_t}{2} \int_{-1}^1 \int_{-1}^1 I_d(z, u') P(u, u') du' du \\ &+ \frac{\sum_t}{2} \int_{-1}^1 P(u, 1) I_c(z) du \end{aligned} \quad (3.48)$$

and substituting equation (3.23) and (3.26) for the diffuse and collimated intensities.

The expression is then written

$$\frac{d}{dz} \int_{-1}^1 I_d(z, u) u du = -\sum_a \int_{-1}^1 I_d(z, u) du + \sum_s I_c(z) \quad (3.49)$$

This is identical to Van Gemert⁸, Star⁷ and Ishimaru¹.

For the diffusion equation an expression in diffuse space irradiance is required. Therefore to obtain this expression the radiative transfer equation is multiplied by u and integrated between 1 and -1 to give terms of $F_d(z)$ and $\phi_d(z)$ (representing the volume flux balance)

$$\begin{aligned} \frac{d}{dz} \int_{-1}^1 I_d(z, u) u^2 du &= \Sigma_t \int_{-1}^1 I_d(z, u) u du + \frac{\Sigma_t}{2} \int_{-1}^1 \int_{-1}^1 I_d(z, u') P(u, u') du' u du \\ &+ \frac{\Sigma_t}{2} \int_{-1}^1 P(u, 1) I_c(z) u du \end{aligned} \quad (3.50)$$

$$\frac{d}{dz} \int_{-1}^1 I_d(z, u) u^2 du = -[\Sigma_a + (1-g)\Sigma_s] \int_{-1}^1 I_d(z, u) u du + \Sigma_s g I_c(z) \quad (3.51)$$

Van gemert,⁸ Star⁷ and Ishimaru¹ all have identical or similar equations for the volume flux balance.

The mean cosine of scatter g is defined (also known as the asymmetry parameter) as

$$g = u = \frac{\frac{1}{2} \int_{-1}^1 u P(u, 1) du}{\frac{1}{2} \int_{-1}^1 P(u, 1) du} = \frac{\frac{1}{3} W_1}{W_0} \quad (3.52)$$

Combinations of equations (3.39), (3.40), and (3.41) with equations (3.49) and (3.51) yields the final set of equations needed for the diffusion approximation and for the conversion of the Kubelka – Munk coefficients into Radiative transfer coefficients (detailed in chapter 5)

$$\frac{dF_c(z)}{dz} = -(\Sigma_a + \Sigma_s) F_c(z) \quad (3.53)$$

$$\begin{aligned} \frac{dF_+(z)}{dz} = & - \left[2\Sigma_a + \frac{3}{4} \{ \Sigma_a + (1-g)\Sigma_s \} - \Sigma_a \right] F_+(z) + \\ & \left[\frac{3}{4} \{ \Sigma_a + (1-g)\Sigma_s \} - \Sigma_a \right] F_-(z) + \\ & \frac{\Sigma_s}{4} (2+3g) F_c(z) \end{aligned} \quad (3.54)$$

$$\begin{aligned} -\frac{dF_-(z)}{dz} = & - \left[2\Sigma_a + \frac{3}{4} \{ \Sigma_a + (1-g)\Sigma_s \} - \Sigma_a \right] F_-(z) + \\ & \left[\frac{3}{4} \{ \Sigma_a + (1-g)\Sigma_s \} - \Sigma_a \right] F_+(z) + \\ & \frac{\Sigma_s}{4} (2-3g) F_c(z) \end{aligned} \quad (3.55)$$

The term diffusion approximation is clarified when the diffuse part of equation above is rewritten

$$\begin{aligned} \frac{d^2 [F_+(z) + F_-(z)]}{dz^2} = & 3\Sigma_a [\Sigma_a + (1-g)\Sigma_s] [F_+(z) + F_-(z)] - \\ & \frac{3}{2} \Sigma_s [\Sigma_s + (1-g)\Sigma_a] F_c(z) \end{aligned} \quad (3.56)$$

converting $[F_+ - F_-]$ into the diffuse fluence rate $\phi_d(z)$

$$\left[\frac{d^2}{dz^2} - D^{-1} \Sigma_a \right] \phi_d(z) = -3 \Sigma_s [\Sigma_s + (1+g)\Sigma_a] F_c(z) \quad (3.57)$$

This is the same as Van Gemert.⁸

where the diffusion coefficient D is defined as¹⁴

$$D = \{ 3[\Sigma_a + \Sigma_s(1-g)] \}^{-1} \quad (3.58)$$

The absorption coefficient should be much smaller than the scattering coefficient and the slab thickness much larger than the mean free path

Close to a boundary or a source, light can be highly forward scattered and under this condition various different forms of the phase function are used for a more realistic prediction of the nature of the light distribution. The Henyey Greenstein phase function is often used with modified forms using a delta function to account for highly forward scattering medium.

3.4 References

1. Wave propagation and scattering in random media, Ishimaru A, Academic Press, New York, (1978)
2. Ishimaru A, Appl. Opt. **28**,12 (1989)
3. Wilson B C, Patterson M S, Phys. Med. Biol. **31** (4), 327 (1986)
4. Marleen K, Star W, Storchi P, Appl. Opt. **27** (9), (1988)
5. Jacques S L, Prahl S A ,Lasers Surg. Med. **16**, 494 (1987)
6. Star W, Proc SPIE **5** dosimetry of laser radiation in medicine and biology
7. Star W M, Marijnissen J P A, van Gemert M J C, Phys. Med. Biol. **33**, (4), 437 (1988)
8. van Gemert M, Welch A J, Star W, Motamedi M, Cheong W, LIMS **2**, 295 (1987)
9. Marleen K, Star W M, Pascal R, Storchi M, Appl. Opt. **27** (9) (1988)
10. Reynolds L, Johnston C C, Ishimaru A, Appl Opt. **15**, 2059 (1976)
11. Mathematical methods for physicist, Arken G, New York, Academic Press (1971)
12. Furutsu K, J. Opt. Soc. Am. **70**, 360 (1980)
13. Profio A E, Doiron D R, Med. Phys. **8**, 190 (1981)
14. Groenhuis R A J, Ferwerda H A, Ten Bosch J J, Appl. Opt. **15**, 2059, (1978)

4 Goniophotometry

4.1 Introduction

For radiation in the region of 630nm the transition from a collimated to diffuse beam occurs in the first few hundred micron of penetration in the tissue. In many medical applications, this is the most critical region and knowledge of the scattering function that characterises it is necessary in understanding the behaviour of the light. This scattering function is referred to as the phase function. The scattering phase function describes the probability per unit solid angle of scattering into angle θ , with $\theta = 0^\circ$ and 180° corresponding to forward and backward scattering respectively. The measurement of the phase function requires samples that are thin enough to ensure single scattering dominates. At 630 nm single scattering dominates in soft tissues for thickness less than $150 \mu\text{m}^1$.

The experimental arrangement for measuring the angular dependence of light scattered by tissue is shown in figure 4.1 and is referred to as a goniophotometer. In this the detector is rotated about the sample in a plane, and the scattered light flux measured at each angle θ . Refraction at the sample glass slides should be minimised by placing the samples at the centre of a cylindrical tank containing an index-matched liquid. These measurements have provided useful information about light scattering in pig's lung, human necrotic lung tissue and Soyacal (an optical phantom). Other researchers have documented values for the phase function of various tissues; these will be reviewed later.

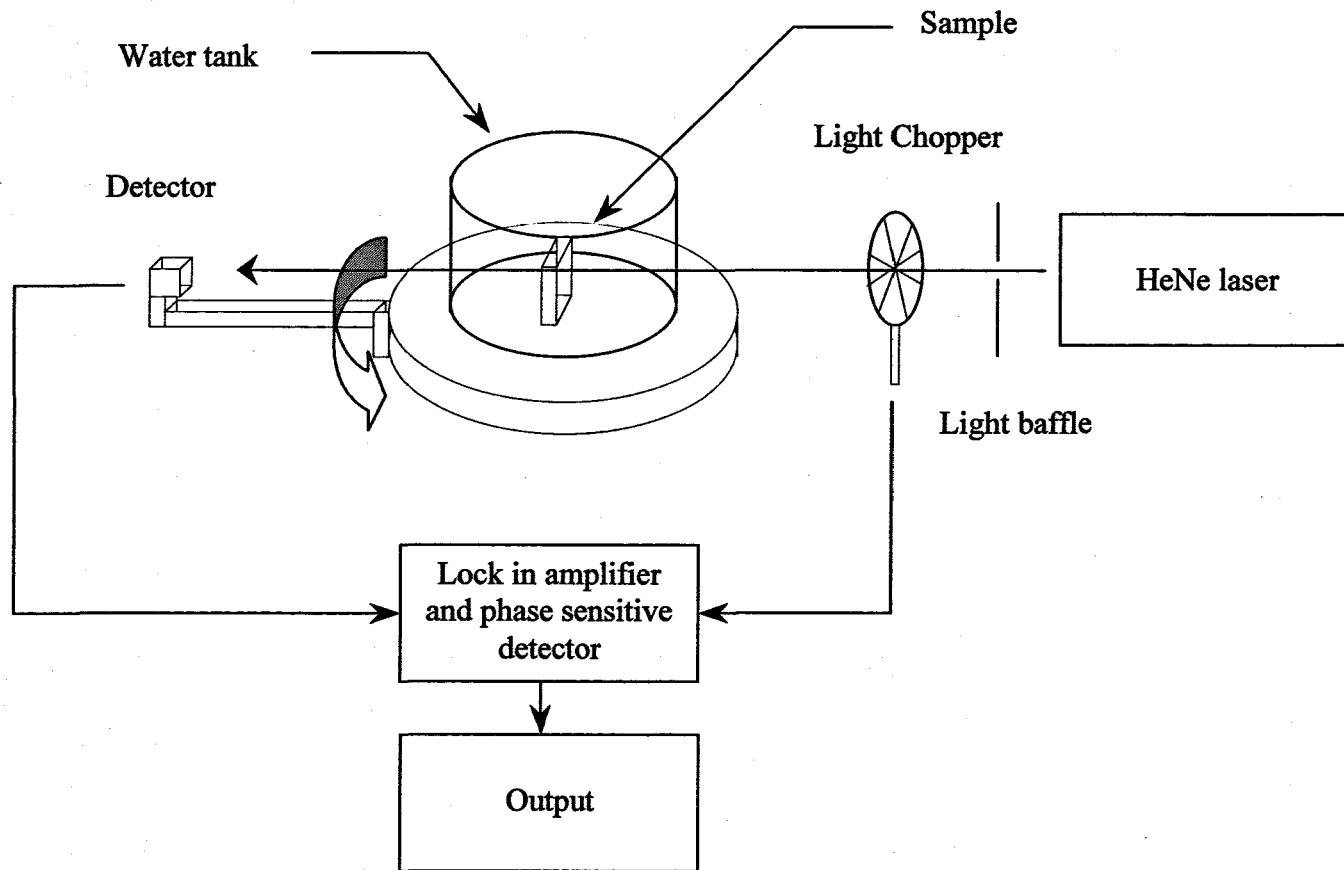


Figure 4.1 Goniophotometer apparatus for phase function measurements. HeNe laser light enters the water filled tank, strikes the sample and is then scattered. The light is detected by a photodiode positioned on a rotating arm.

The aim of the work discussed in this chapter is to characterise the phase function for human necrotic lung samples, pig lungs with and without blood and Soyacal (an intravenous feed). The experiments were conducted with a HeNe laser at 632.8nm, since Photodynamic therapy for lung cancer is carried out at this wavelength.

4.2 Phase Function

When light strikes a particle the angle at which the light is reflected is a function of the size and shape of the particle, the angle of incidence, and of the surrounding medium and the incident wavelength. In general each particle will have a different scattering profile. This scattering profile is called the phase function. The phase function represents the amount of scattered power and is not related to the phase of the wave. The name “phase function” has its origins in astronomy where it refers to lunar phases². The phase function is a complex concept for biological media since it is difficult to isolate absorbing and scattering particles in the complex tissue structure. Experimental methods can be devised to estimate the phase function rather than assuming an isotropic scattering applies.

The choice of phase function is an important decision in any calculation of multiple or single scattering. The main single scattering characteristics are the albedo and the phase function also known as the asymmetry parameter and will be discussed in depth later. The phase function is a probability distribution; consequently the normalisation condition requires the integral of the phase function over all angles to equal unity.

$$\int_{4\pi} p(\hat{s}, \hat{s}') d\omega = 1 \quad (4.1)$$

Where the phase function $p(\hat{s}, \hat{s}')$ describes the amount of light scattered from the direction denoted by the unit vector \hat{s} into the direction \hat{s}' and $d\omega$ is a differential solid angle in the direction of s . This does not allow the phase function to describe the absorption of light by the particle since the phase function is a description of the distribution of scattering by the particle.

For simplicity an average phase function which describes the scattering process is used. This average phase function is constrained by assuming that the probability of scattering from one direction into another is a function only of the angle between the two directions hence

$$p(\hat{s}, \hat{s}') = p(s \cdot s') = p \cos \theta \quad (4.2)$$

The simplest of the phase functions is that of the isotropic scattering and is described by

$$p(s \cdot s') = \frac{1}{4\pi} \quad (4.3)$$

The phase function has units of sr^{-1} . and the factor of $1/4\pi$ results from normalisation. When the phase function is not isotropic, the mean cosine of scatter is used to describe the degree of anisotropy. This is denoted by g and is defined as the integral over all angles of the phase function multiplied by the cosine of the angle.

$$g = \int_{4\pi} p(s \cdot s')(s \cdot s') d\omega \quad (4.4)$$

Various researchers have used different phase functions depending on the type of tissue used. A brief explanation of these phase functions is necessary to facilitate an understanding of their results.

Eddington phase function

The simplest and most popular approximation to the equation of radiative transfer is the Eddington approximation³. Simple approximations like the Eddington are capable of coping with the highly asymmetrical phase functions typical of particle scattering.

$$P_{Edd}(\cos \theta) = \frac{1}{4\pi} \{1 + 3g' \cos \theta\} \quad (4.5)$$

where g' is the asymmetry factor. With this approximation the transport equation may be reduced into a diffusion equation as in Ishamaru². Such a solution provides a qualitative picture of radiative transport in a media which is not highly forward scattering and is therefore not suitable for tissue.

Delta Eddington phase function

The Delta Eddington⁴ function is used to describe forward peaked scattering.

$$P(\cos \theta) \approx P_{\delta-Edd}(\cos \theta) = \frac{1}{4\pi} \{2f\delta(1 - \cos \theta) + (1 - f)(1 + 3g' \cos \theta)\} \quad (4.6)$$

where f is the fractional scattering into the forward peak. As $f \rightarrow 1$ the phase function becomes exactly a delta function and as $f \rightarrow 0$ the phase function reduces to

the Eddington approximation. The delta function forces the result to a particular direction.⁵

To have the same mean cosine of scatter (g) as the original phase function,

$$g = f + (1 - f)g_{de} \quad (4.7)$$

Henye - Greenstein phase function

The Henye - Greenstein formula is often used to describe scattering from blood cells.⁶ The Henye - Greenstein function is not based on a mechanistic theory of scattering, but was chosen by the two physicists to approximate Mie scattering. The phase function used is

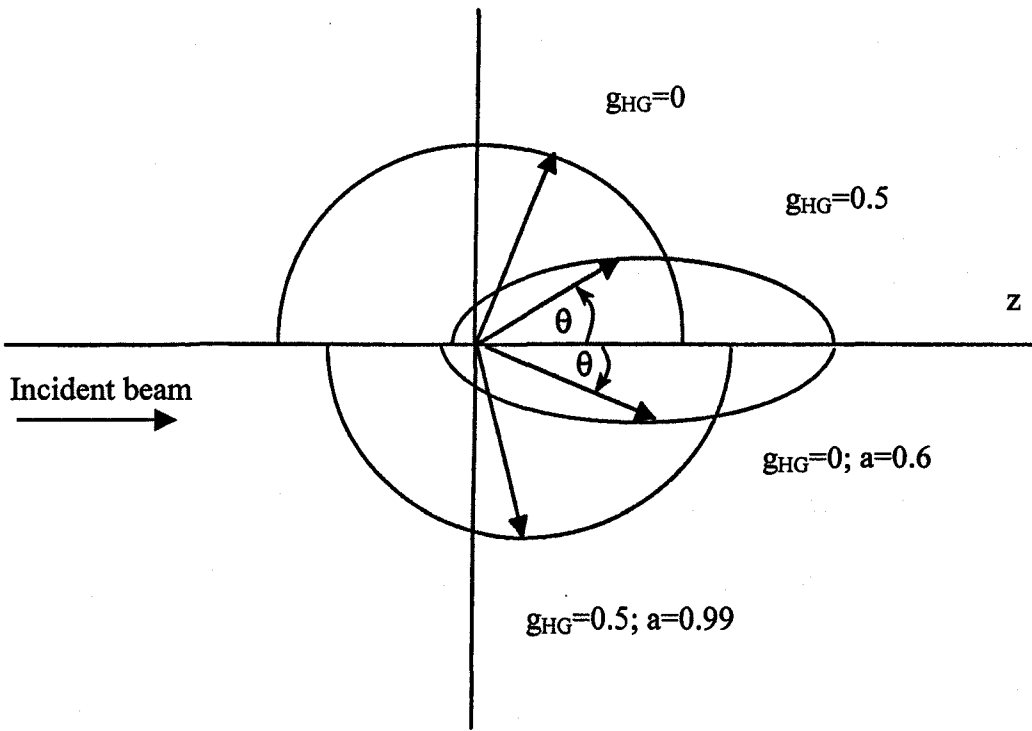
$$P_{HG}(\cos\theta) = \frac{1}{4\pi} \frac{1 - g_{HG}^2}{(1 + g_{HG}^2 - 2g_{HG} \cos\theta)^{3/2}} \quad (4.8)$$

The Henye - Greenstein phase function depends only on the anisotropy coefficient that varies between 0 and 1, as the scattering varies from isotropic to a completely g_{HG} forward directed scattering pattern as in figure 4.2.

The Henye - Greenstein term was combined with an isotropic scattering term to create a composite phase function to characterise scattering from samples of human dermis⁷ and is referred to as the modified H-G term.

$$P_{m-HG}(\cos\theta) = \frac{1}{4\pi} \left[\beta + (1 - \beta) \frac{1 - g_{HG}^2}{(1 + g_{HG}^2 - 2g_{HG} \cos\theta)^{3/2}} \right] \quad (4.9)$$

(a) Phase function



(b) Diffusion pattern

Figure 4.2 (a) Henyey - Greenstein phase function for $g_{HG} = 0$ and $g_{HG} = 0.5$ as a function of angle θ with the z axis. The amplitudes have been normalised. (b) Diffusion pattern for two combinations of g_{HG} and $a = \Sigma_s/\Sigma_t$ (albedo) as a function of angle with the z-axis. For isotropic scattering the diffusion pattern can be forward peaked if there is sufficient absorption. Conversely, the diffusion pattern can be nearly isotropic even if the scattering is forward peaked, provided absorption is sufficiently small¹².

Where β represents the amount of light scattered isotropically and the second term is the Henyey Greenstein function. The factor β was necessary to account for the amount of backscattered light in excess of that described by the H- G function, especially where thicker samples were used as multiple scattering increased the isotropic component.

$$g = (1 - \beta)g_{HG} \quad (4.10)$$

where g_{HG} is the average cosine angle for the Henyey – Greenstein term only.

To fit the modified Henyey – Greenstein phase function to the measured phase function where the albedo of the tissue is unknown then it is convenient to include an arbitrary multiplication factor χ in the expression for the phase function.

$$aP_{meas}(\cos\theta) = \chi P_{m-HG}(\cos\theta) \quad (4.11)$$

and

$$\chi = 4\pi a \quad (4.12)$$

where a is the albedo. Hence,

$$P_{meas}(\cos\theta) = \chi \left[\beta + (1 - \beta) \frac{1 - g_{HG}^2}{(1 + g_{HG}^2 - 2g_{HG} \cos\theta)^{3/2}} \right] \quad (4.13)$$

4.3 Goniophotometer apparatus

A sample was placed at the centre of a 16.3 cm diameter tank with 2 mm thick walls and held in place with two pair of opposing hair springs. The tank was filled with distilled water prefiltered to $2\mu\text{m}$ to minimise light scattering from dust or other particle contaminants. The water tank reduced both specular reflection at the microscope slide faces and the refraction of scattered photons.

A Helium Neon laser delivered a 38mW beam normal to the sample. The beam passed through a 1mm diameter pin hole and a Roufin Sinar light chopper operating at 100 Hz with its reference signal connected to a Brookdial Electronics phase sensitive detector type 411. A light baffle was placed between the laser and the tank to reduce the background light from the laser tube. Scattered light was measured with a photodiode of area 1mm^2 , located on the detector arm and connected to a phase sensitive detector and Brookdial Electronics low noise amplifier type 411, the output of which was fed to a Thurlby Digital Intelligent Multimeter type 1905a. The detector arm from the goniophotometer apparatus of radius 19.1 cm was manually rotated about the sample in the plane of the laser beam every 2 degrees with a resolution of ± 0.1 degrees and with a full 360 degrees movement. Forward and backward scattering distributions were measured in this way but the radial profile was extrapolated around 90 degrees and 180 degrees due to the sample holder and size of detector blocking the laser beam.

Neutral density filters were placed between thin samples and the detector to avoid saturation. The raw data from the photodiode was subjected to a series of calculations to account for specular reflection and refraction effects at the sample boundary. This

yielded a description of the light that exited the tissue at a given angle θ_{exit} as opposed to the observed angle θ_{obs} .

4.4 Tissue preparation

All pig lung samples used in these experiments were obtained within 4 hours of resection. The pig lungs were thoroughly rinsed both internally and externally with 0.9% saline to remove any excess blood. The lung tissue was then cut into small pieces ensuring no membrane or bronchiole cartilage was included. These sections were combined with lung sections from six other pig lungs and then homogenised. This procedure was carried out five times. The homogenate was then stored until the onset of the experiments. By combining the sections from a number of lungs any variation attributable to a given sample was greatly reduced.

Before each tissue sample was placed on the microscope slide, the combined thickness of the two microscope slides was measured and recorded using a micrometer. The micrometer had one $5\mu\text{m}$ glass bead adhered to the surface of each jaw face and positioned so that the beads were adjacent each other when the jaws were closed. The beads would now act as the reference point for measuring the thickness. The micrometer was reset to zero and had an accuracy of $\pm 0.5\mu\text{m}$. This alteration to the micrometer was necessary as the face area of each jaw was approximately half the tissue sample size and an accurate measurement of the sample thickness was essential.

Polymer sheets of known thickness ranging from 25 μm to 400 μm were then placed onto a microscope slide. The sample thickness ranges were 25, 35, 50, 75 and 100 μm , with an increase of thickness every 50 μm thereafter. There was no water or saline added to the tissue while on the microscope slide. The sample was then gently compressed between either microscope slide to the known polymer thickness. The microscope slides were then sealed using a glass adhesive cured in UV light for thirty seconds. This ensured that blood did not leach from the sample into the water surrounding the cell and also prevented the sample from dehydrating. The thickness of the combined sample was then recorded with the initial thickness of the two microscope slides being deducted. The microscope slides was measured at the centre of the tissue and at the edges of the slide to ensure uniform thickness of the tissue sample. The samples were used within 30 minutes with no significant degradation occurring during this period.

The second set of experiments involved using bloodless tissue. This was achieved by placing the tissue from the homogenate into a hand held test tube homogeniser with saline. By gently aggravating the tissue the blood seeped out of the tissue and into the saline; this was repeated until no discoloration of the saline was observed. Each sample was then placed in saline for 10 minutes, after which the tissue was then mounted on the microscope slides as before.

The two human necrotic tumours measuring approximately 2cm long and 0.5cm in diameter were frozen within 20 minutes of resection. The tumours were not from the same patient but both tumours were from the patients bronchiole. The tumour was cut into small pieces and homogenised using a hand held homogeniser. Care was taken

when homogenising the tissue, as enthusiastic aggravation would lead to blood loss from the tissue. The tissue was then frozen until experimental work began. One necrotic tumour was frozen for 1 month and the other for several days. The samples were prepared as before with a “sandwich effect” between the glass slides.

Soyacal, a fat emulsion was used as the reference material to the system. The aqueous suspension of 10% Soyacal, the stock solution for this series of experiments, contained 100g fractionated soya bean oil, 6g fractionated egg phospholipids and 11.25g glycerol made up to 500ml with water. The mean particle size was measured and found to be $444 \pm 84\text{nm}$.⁸ The Soyacal was further diluted with de - ionised water filtered to $2\mu\text{m}$ to a 1% aqueous solution and stored in a fridge for no longer than 4 hours. The dilution was accomplished using 10ml and 100 ml pipettes and with a 1l measuring flask with errors of +/- 0.1, 0.5 and 2.5ml respectively.

The freezing microtome method for achieving thin samples was not employed. Lung tissue due to its nature is sponge like. After being microtomed the lung tissue appears to have holes in the sections, due to the aveoli. These holes can account for a considerable amount of the surface area of the sample. Air bubbles caught in the sample between the microscope slides are another problem. This can be reduced using a drop of saline but care has to be taken not to dilute the sample and cause miss readings.

4.5 Data analysis

The experiments used tissue held between two glass slides and submerged in deionised water. Due to the differing refractive indices of the media, corrections for reflection and refraction must be made.

At the surface boundary between two optical media, a fraction of the incident light is reflected. For light travelling in a dielectric medium of refractive index n_1 that is incident on a dielectric of index n_2 the fraction reflected at normal incidence is given by,

$$R = \frac{(n_1 - n_2)^2}{(n_1 + n_2)^2} \quad (4.14)$$

The total transmission through an optical element is the product of its surface transmissions and its internal transmission. For a plane parallel glass plate of index $n_2 = n$ and in air $n_1 = 1$ the transmission of the first surface is given by,

$$T = 1 - R = 1 - \frac{(1 - n)^2}{(n + 1)^2} \quad (4.15)$$

When some of the radiation is absorbed the transmission T is given as,

$$T = e^{-ax} \quad (4.16)$$

where the thickness is x and the absorption coefficient is a .

The light transmitted through the first surface is partially transmitted by the medium and goes on to the second surface, where it is partially reflected and partly transmitted. The reflected beam passes back through the medium where it hits the first surface again and

is partially reflected and transmitted and so on. The resulting transmission can be expressed as the infinite series

$$T_{1,2} = T_1 T_2 (K + K^3 R_1 R_2 + K^5 (R_1 R_2)^2 + K^7 (R_1 R_2)^3 + \dots) \quad (4.17)$$

Transmission at a given angle (θ) can be given as

$$T(\theta) = \frac{T_1 T_2}{1 - R_1 R_2} \quad (4.18)$$

where T_1 and T_2 are the transmissions of the two surfaces, R_2 and R_1 are the reflectances of the surfaces, and K is the transmittance of the medium between them which is assumed to be equal to 1.

This calculation for $T(\theta)$ considers the reflections within the glass slide between the tissue/glass and glass/saline interface.

The refractive index of the glass slide n_g was given to be 1.54 and the refractive index of prefiltered de-ionised water as 1.33. Jacques and Prahl⁹ quotes the refractive index of the bloodless tissue as 1.37. This was based on the generalisation that the refractive index of tissue would vary from 1.33 – 1.5 for water content between 100 to 0 percent. The water content of tissue varies from 70 – 85 percent.

When $\theta = 0$ the Fresnel reflection can be calculated using equations 4.15 - 4.18. For a saline / glass interface $R_1 = 0.0054$ and for a glass / tissue interface $R_2 = 0.0034$ yielding the resultant reflectance $R_f = 0.009$ (0.9 %).

The data was also transformed by a series of calculations to achieve an actual description of the light that exited the tissue at any given angle compared to the observed light at a given angle.¹⁰

(1) The Scattered light was detected by a photodiode with the output voltage signal producing the analog of the collected power in watts. Since the phase function used in the radiative transfer equation describes the distribution of light scattered once, the phase function is equal to the scattering function $I(\theta)$ for an incremental tissue thickness divided by a normalisation factor. Normalisation is necessary because only the scattered light has contributed to the observed $I(\theta)$, and much of the light has passed through the sample undisturbed. Division by $(1-r_s)$ corrected for the specular reflectance ($r_s = 0.009$) from the front glass slide as the incident beam entered the tissue.

$$P(\theta_{obs}) = \frac{V(\theta_{obs})}{V_d(1-R_f)} \quad (4.19)$$

where $V(\theta_{obs})$ is the voltage at the observed angle and V_d is the direct beam voltage.

(2) The solid angle ω of the collection area is given by

$$\omega = \frac{A_d}{R_g^2} \quad (4.20)$$

A_d is the detector area and R_g is the radius of the goniometer arm. The observed power P_{obs} was divided by the solid angle yielding the radiant intensity $R(\theta)$.

$$R(\theta) = \frac{P(\theta)}{\omega} \quad (4.21)$$

Since radiant intensity from a planar surface is observed to diminish at oblique angles, according to a $\cos(\theta)$ factor,¹¹ it is necessary to correct for this viewing angle.

$$R_c(\theta) = \frac{R(\theta)}{|\cos(\theta)|} \quad (4.22)$$

The refraction at the tissue / glass / saline interfaces causes the solid angle to expand as light exited the tissue, especially at oblique angles of observation (n^2 -Law)¹². The radiant intensity was corrected for this refraction. The angles (θ_1) and (θ_{obs}) are defined in figure 4.3.

$$R_{cf}(\theta) = R_c(\theta) \frac{|\cos(\theta_1)|n_1^2}{|\cos(\theta_{obs})|n_3^2} \quad (4.23)$$

(5) Fresnel Reflection at the interfaces allowed only a fraction $f(\theta)$ of the light to escape and reach the detector.

$$I(\theta_{obs}) = \frac{R_{cf}}{f(\theta)} \quad (4.24)$$

Where,

$$f(\theta) = T_1 T_2 (1 + R_1 R_2 + (R_1 R_2)^2 + (R_1 R_2)^3 + \dots) \quad (4.25)$$

The portion of the light reflected from the surface of an ordinary dielectric material i.e. glass is given by¹³

$$R_{1,2} = \frac{1}{2} \left[\frac{\sin^2(\theta_i - \theta_t)}{\sin^2(\theta_i + \theta_t)} + \frac{\tan^2(\theta_i - \theta_t)}{\tan^2(\theta_i + \theta_t)} \right] \quad (4.26)$$

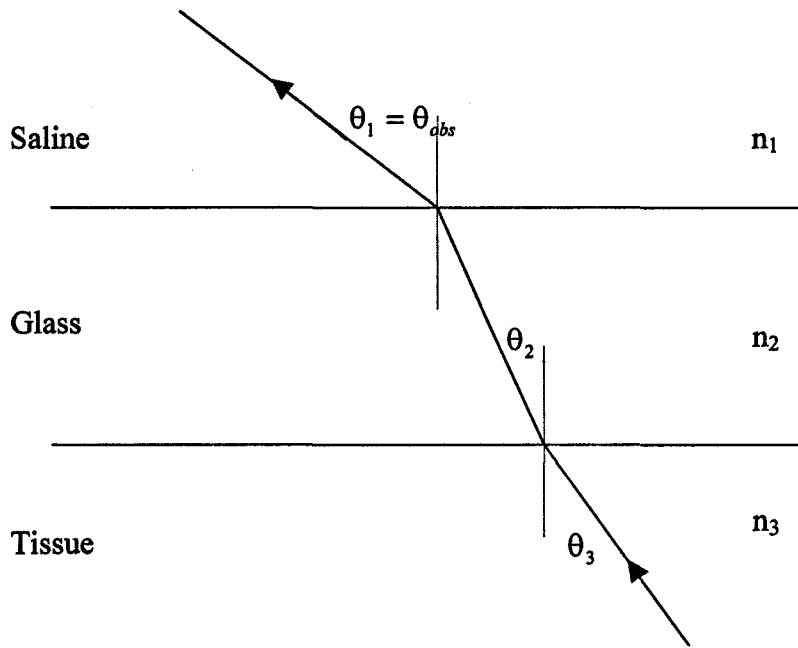


Figure 4.3 The refraction of light at the tissue/glass/saline interfaces as light escapes the tissue. The indices of refraction are 1.37 for dermis, 1.54 for glass and 1.33 for water.

Where θ_i and θ_t are the angles of incidence and transmission respectively. The first term gives the reflection of the light that is polarised in the plane of incidence and the second term the reflection for the orthogonal plane.

The angles were calculated using snells law:

$$\begin{aligned}\theta_1 &= \theta_{obs} \\ \theta_2 &= \arcsin(\sin(\theta_1) \frac{n_1}{n_2}) \\ \theta_3 &= \arcsin(\sin(\theta_1) \frac{n_1}{n_3})\end{aligned}\tag{4.27}$$

This calculation of $f(\theta)$ considers the reflections within the glass slide between the tissue/glass and glass/saline interface.

(6) The value $I(\theta_{exit})$ was then attributed to the true angle of exitance from the tissue θ_{exit} as opposed to the observed angle θ_{obs} , by correcting for the refraction at the tissue/glass and glass/water interfaces.

$$\theta_{exit} = \theta_1\tag{4.28}$$

This series of calculations yielded the radiant intensity of light $I(\theta_{exit})$ in W/sr for a 1W incident beam as it excited the tissue. The corrections become increasingly more important at widely scattered angles and enable proper evaluation of the scattered light.

Measurements of the angular light distribution for pig lung samples with and without blood is shown in figure 4.4 for 30 μ m and 300 μ m thick samples. Since the light distribution from 0 $^\circ$ to -180 $^\circ$ was almost identical to that from 0 $^\circ$ to 180 $^\circ$, it was omitted in this figure. The measured radial profile was between 0 $^\circ$ -75 $^\circ$ in the forward direction

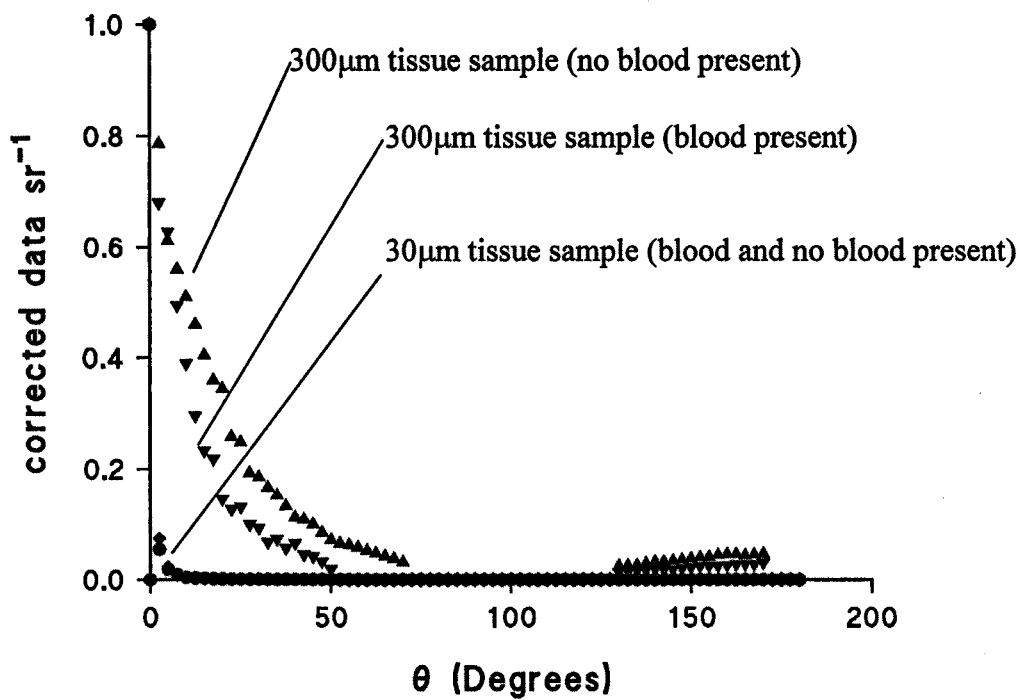


Figure 4.4 corrected angular distributions of scattered light 30 μm and 300 μm thick lung samples

and $130^\circ - 170^\circ$ in the backward direction and was extrapolated around 90° and 180° . The measured radiance around 90° (perpendicular to the laser beam) did not represent the real scattering pattern due to the increased path length of the scattered light in the sample and the physical practicalities of holding the sample in place. Backward scattered light was also extrapolated around 180° due to the physical size of the detector obstructing the incoming laser beam.

4.6 Least square fit

The modified Henyey – Greenstein was found to accurately represent the phase function for tissue.¹⁴ Using equation (4.13) to specify the radiant intensity $I(\theta)$ the modified Henyey Greenstein phase function can be found.

$$I(\theta_{exit}) = \chi \left[\beta + (1 - \beta) \frac{1 - g_{HG}^2}{(1 + g_{HG}^2 - 2g_{HG} \cos \theta)^{3/2}} \right] \quad (4.29)$$

An assumption of the modified H – G phase function is that light scattered in the backward direction is scattered isotropically. The fraction of light scattered in the backward direction ($\chi\beta$) is determined by averaging values for $I(\theta_{exit}) +130^\circ < \theta < +170^\circ$ and $-130^\circ < \theta < -170^\circ$ and by extrapolating values between $\pm 90^\circ < \theta < \pm 180^\circ$ that were unobtainable. The scale factor χ depends on the optical depth and albedo of the sample. The factor β is the fractional component of the isotropic scattering and was needed to account for backscattered light in excess of that described by the H - G phase function.

The forward transmitted light is used to find the two parameters g_{HG} and χ by transforming equation (4.29) into the form $y=mx+c$,

$$(I(\theta_{exit}) - \chi\beta)^{-2/3} = \left\{ \frac{-2g_{HG}}{[\chi(1-\beta)]^{2/3}(1-g_{HG}^2)^{2/3}} \right\} \cos \theta + \frac{(1+g_{HG}^2)}{[\chi(1-\beta)]^{2/3}(1-g_{HG}^2)^{2/3}} \quad (4.30)$$

Where $x = \cos \theta$, $m =$ the slope and c is the y intercept.

A plot of $(I(\theta_{exit}) - \chi\beta)^{-2/3}$ versus $\cos \theta$ with a least square fit in the range $\cos \theta \geq 0.85$ was used to find the slope and intercept for each tissue sample. An example is shown in figure 4.5. As the angle of scatter increased the errors between points increased and therefore it was necessary to use the least square fit in the range $\cos \theta \geq 0.85$. The parameters g_{HG} and χ can now be recovered in terms of the calculated intercept c , slope m and the fraction of light scattered isotropically backward ($\chi\beta$).

$$g_{HG} = -\frac{c}{m} - \sqrt{\frac{c^2}{m^2} - 1} \quad (4.31)$$

$$\chi = \left[\frac{\left(\frac{-2g_{HG}}{m} \right)^{3/2}}{1-g_{HG}^2} \right] + \chi\beta \quad (4.32)$$

Using the scale factor χ the fractional component β of the isotropic scattering in the backward direction ($\chi\beta$) can be found

$$\beta = \frac{\chi\beta}{\chi} \quad (4.33)$$

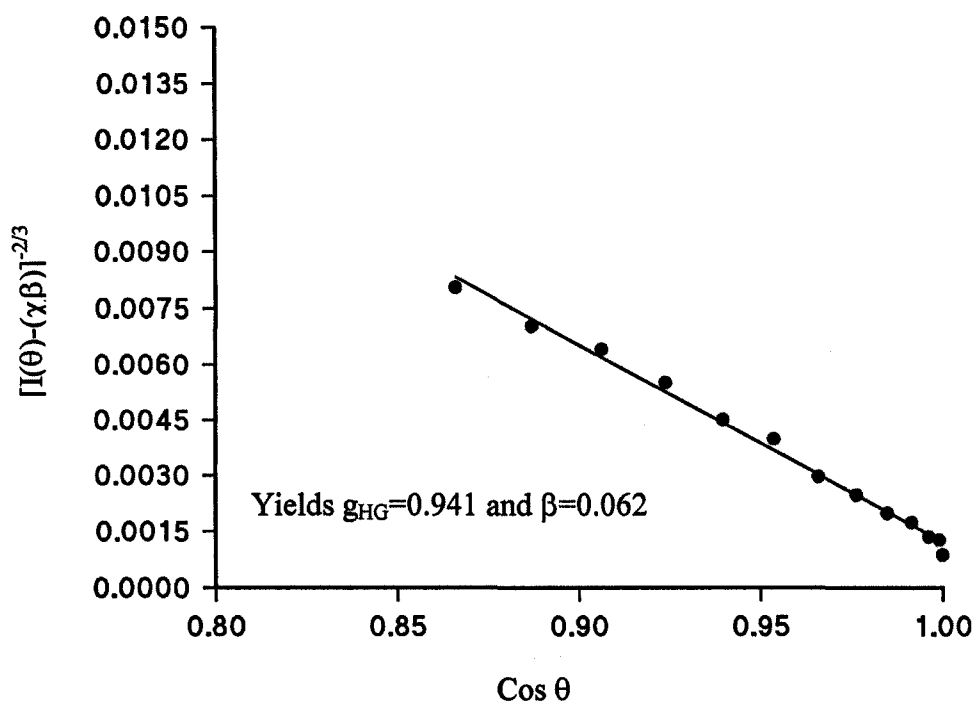


Figure 4.5 Specification of Henyey-Greenstein phase function for 50 μm tissue sample (without blood) least square fit $\cos\theta > 0.85$ yields slope and intercept

4.7 Results/Discussion

In most tissue samples, it is hard to obtain the degree of optical uniformity required for accurate measurements due to the very nature of the tissue. After each set of measurements was taken the tissue sample was repositioned in the holder so that the laser illuminated the same sample in a different place. Each sample was repositioned five times to achieve an average measurement per tissue sample. This was repeated five times with different samples of similar thickness to give an average value for a given thickness. Standard errors were used for the tissue samples with the error being quoted on the final result.

The raw data recorded from the photodiode was subjected to a series of calculation steps as in equations 4.19 – 4.28 to achieve a description of the light that exited the tissue at a given angle θ_{exit} as opposed to the light that was observed at a given angle θ_{obs} from the goniophotometer. The value $I(\theta_{\text{exit}})$ was then attributed to the true angle of exitance from the tissue θ_{exit} as opposed to the observed angle, θ_{obs} in consideration of the refraction of the refraction at the tissue / glass and glass / saline interfaces.

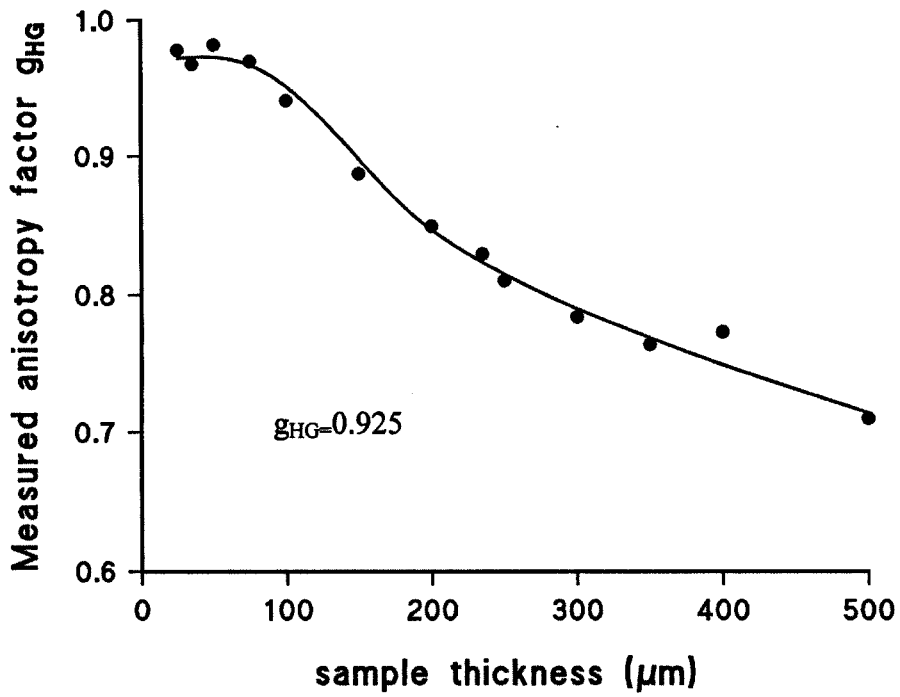
By plotting a graph of $\cos\theta$ versus the forward-directed component of the radiant intensity $[I(\theta_{\text{exit}}) - \chi\beta]^{\frac{2}{3}}$ as shown in figure 4.5 the gradient and intercept were obtained. Placing these into equations 4.31 – 4.33 the Henyey – Greenstein phase function g_{HG} and the isotropic scattering term β were obtained.

Each tissue sample data was processed as before to yield a Henyey – Greenstein phase function g_{HG} and isotropic scatter term β . These were then plotted against the sample

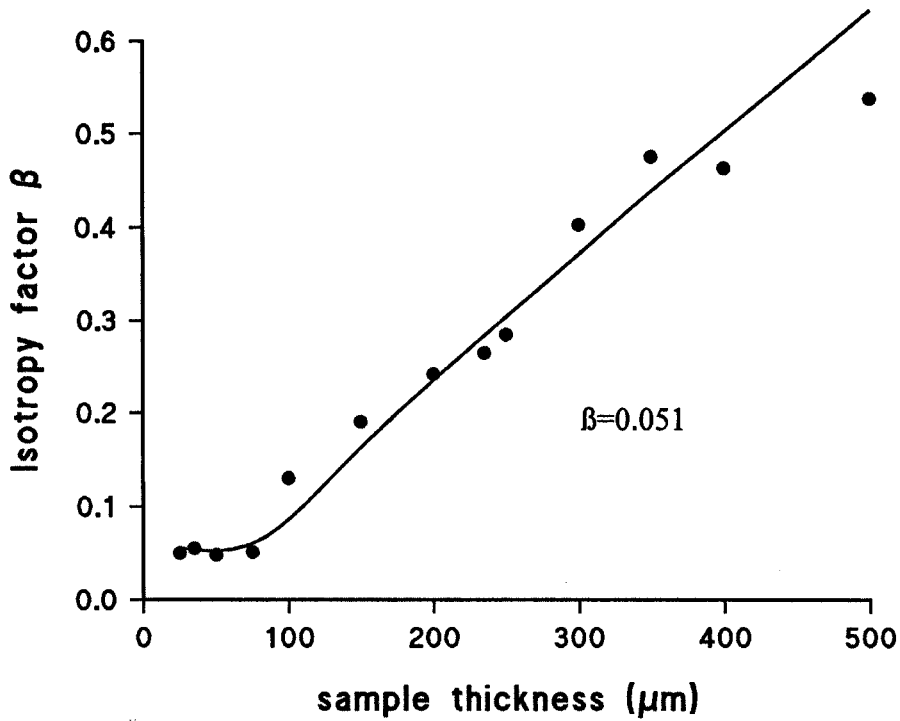
thickness as shown in figure 4.6(a) and 4.6(b) for tissue samples with blood and figure 4.7(a) and 4.7(b) for tissue samples without blood. As the sample thickness decreases the scattering pattern becomes increasingly forward – directed, with the isotropic term β decreasing and the forward peaked g_{HG} increasing. Single scattering in the samples is observed to occur in tissue thickness below $100\mu\text{m}$ where the values of g_{HG} and β approach constant values. The extrapolation to near zero thickness of these constant values yields g_{HG} and β . Values for g_{HG} and β obtained in this way for samples with and without blood and are given in table 4.1. The average cosine of scatter from equation 4.10 is also given in table 4.1.

The H – G phase function and the isotropic scatter β for human necrotic lung tissue is given in figure 4.8(a) and 4.8(b) respectively. The sample thickness range from $25\mu\text{m}$ to $300\mu\text{m}$ for both graphs. Each sample was repositioned in the holder 5 times as before, but only one measurement for each thickness was possible for each of the two resected necrotic tumours. Table 4.1 includes the data for derived average cosine of scatter and the measured H – G phase function and isotropic scatter.

Measurements with a 1% aqueous solution of Soyacal (10%) for 0.25mm to 2mm thickness samples were taken with 0.25mm step increase in thickness. The angular scattering distributions for these measurements were almost identical showing a forward scattering profile. This suggests that single scattering was dominating and the need for work on lower concentrations was not needed. The HeNe laser light without any sample was confined to a divergence angle of $\pm 2^\circ$. The Henyey – Greenstein phase function for Soyacal was determined to be $g_{HG} = 0.909$ with the light scattered isotropically $\beta = 0.098$. Using equation 4.10 the anisotropy factor $g = 0.82$ was obtained

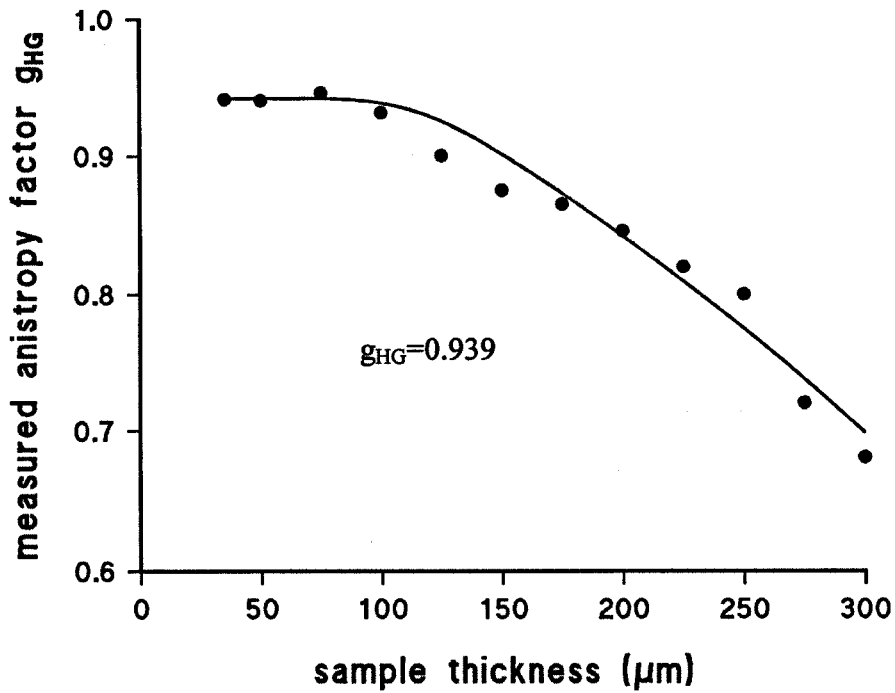


(a)

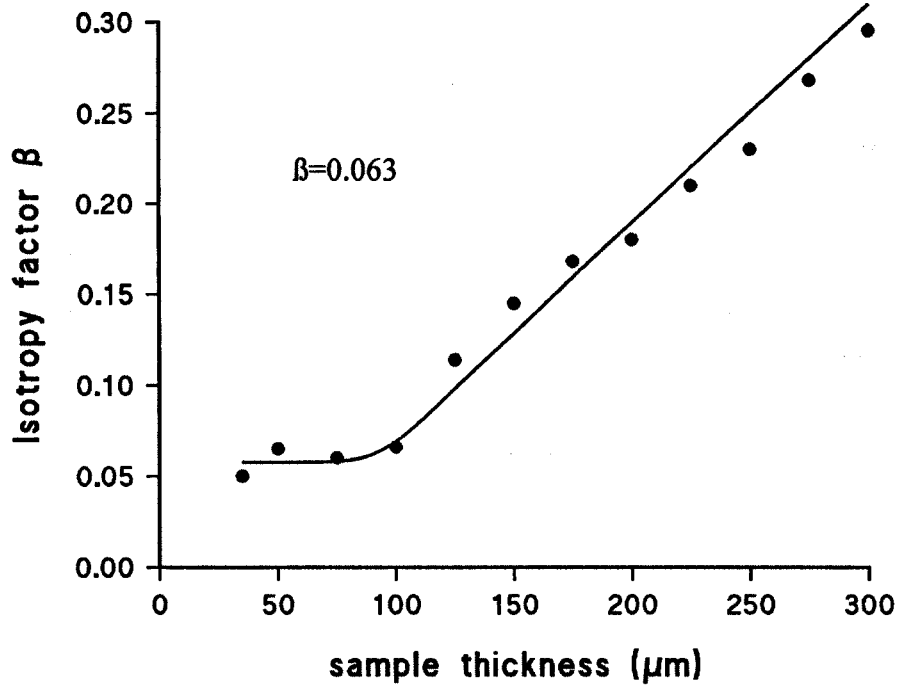


(b)

Fig 4.6(a) The measured anisotropy factor g_{HG} for pig lung as a function of sample thickness. (b) Amount of light scattered isotropically (β) as a function of sample thickness



(a)

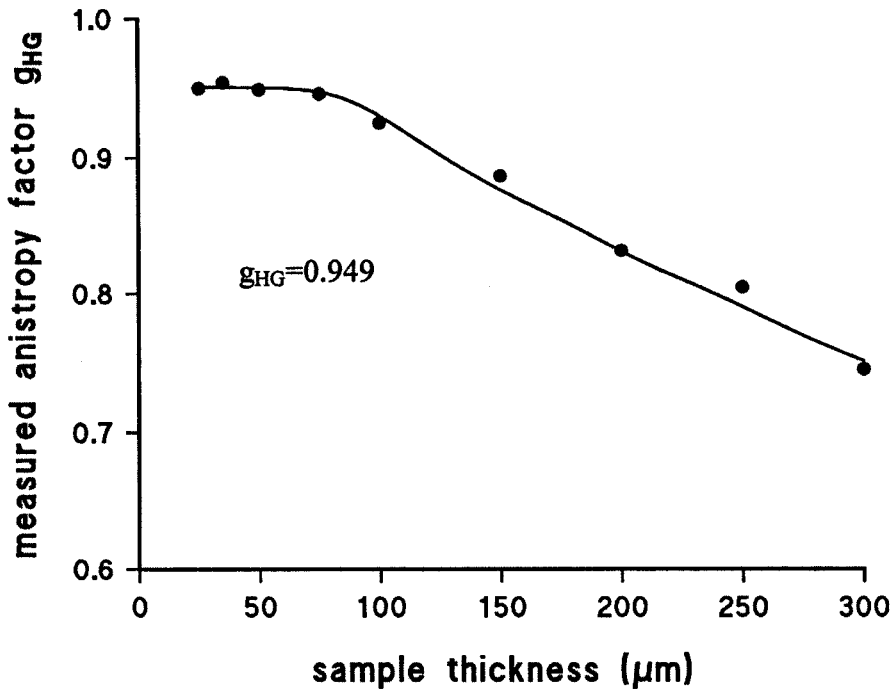


(b)

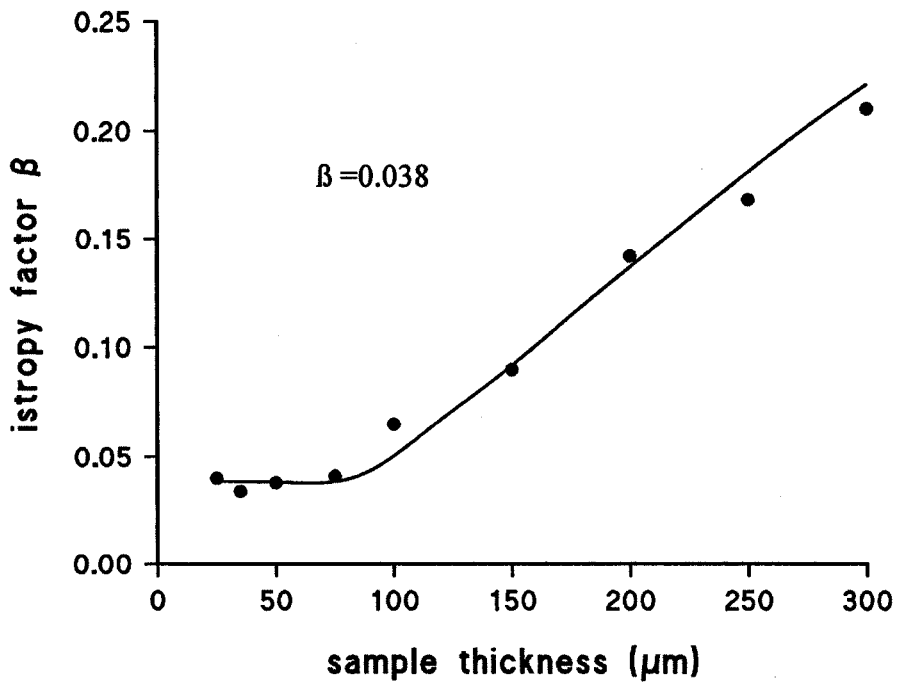
Figure 4.7(a) The measured anisotropy factor g_{HG} for pig lung without blood as a function of sample thickness. (b) Amount of light scattered isotropically β as a function of sample thickness for pig lung with no blood

gHG	β	g	Tissue	references
0.975 ± 0.132	0.051 ± 0.006	0.925 ± 0.016	Pig Lung with blood	Chapter 4
0.939 ± 0.098	0.063 ± 0.005	0.889 ± 0.022	Pig Lung without blood	Chapter 4
0.949 ± 0.111	0.038 ± 0.006	0.913 ± 0.013	Human necrotic tumour	Chapter 4
0.909	0.098	0.82	Soyacal	Chapter 4
0.91	0.1	0.82	Human dermis	⁷
		0.99	Human blood	¹⁵
		0.974	Human blood 1%	¹⁶
		0.690	Nutralilipid 1%	¹⁴
		0.825	Intralipid	¹⁷
		0.83	As above	¹⁸
		0.95	Human lung	¹⁹
		0.95	Human tumour	²⁰
		0.75	Human lung	²¹
		0.965	Chicken muscle	²²

Table 4.1 The average cosine of scatter and the H –G phase function for different media



(a)



(b)

Figure 4.8(a) The measured anisotropy factor g_{HG} for human necrotic lung tissue as a function of sample thickness. (b) Amount of light scattered isotropically β as a function of sample thickness for human necrotic lung tissue

4.8 References

1. Flock S T, Wilson B C, Patterson M S, *Med. Phys.* **14** (5), 836 (1987)
2. *Wave Propagation and Scattering in Random Media*, Ishimaru A, Vol 1 Academic Press, New York (1978)
3. Shettle E P, Weinman J A, *J. of Atm. Sci.* **27**, 1048 (1970)
4. J H Joseph, Wiscombe W J, *J. of Atm. Sci.* **33**, 2452 (1976)
5. *Multiple light scattering, Tables Formulas and applications*, van de Hulst H C, Vol. 2 Academic press, London (1980)
6. Reynolds L, Johnston C, Ishimaru A, *Appl. Opt.* **15**, 2059 (1976)
7. Jacques S L, Alter C A, Prah S A, *Lasers in Life Sci.* **1**, (4), 309 (1987)
8. Driver I, Feather J W, King P, Dawson J B, *Phys. Med. Biol.* **34** (12), 1927 (1989)
9. Jacques S L, Prah S A, *L.I.S.M.* **6** 494 (1987)
10. Jaques S L, Alter C A, Prah S A, *Lasers in life Sci.* **1** (4), 309 (1987)
11. *Principles of optics*, Born M, Wolf E, Oxford Pergamon Press (1970)
12. Keijzer M, Star W M, Storchi P R M, *Appl. Opt.* **27**, 1820 (1988)
13. *Reflectance Spectroscopy*, Wendlant W and Hecht H, J Wiley and Sons, New York, (1966)
14. Star W M, Marijnissen J P, Van gemert M J C, *Phys. Med. Biol.* **33** (4), 437 (1988)
15. Penderson G L, Mc Cormick N L, Reynolds L O, *J. Biophys.* **16**, 199 (1976)
16. Flock S T, Wilson B C, Patterson M S, *Med. Phys.* **14**, (5), 835 (1987)
17. van Staveren H J, Moes C J, Marle J, Prah S A, van Gemert M J, *Appl. Opt.* **31**, 4507 (1991)
18. Star W M, *Photochem. Photobiol.* **46** (5), 619 (1987)
19. Andreola S, Bertoni A, Marchesini R, *Lasers Surg. Med.* **8** Abs. 142 (1988)

20. Qu J, MacAuley C, Lam S, Palcic B., *Appl. Opt.* **34** (31), 333 (1994)
21. Marchesini R, Bertoni A, Andreola S, Melloni E, Sichirollo A, *Appl. Opt.* **28** (12), (1989)
22. Wilson B C, Patterson M S, Flock S T, *Photochem. and Photobiol.* **46** (5), 601 (1987)

5 Reflectance and transmission measurements

5.1 Introduction

Analysis of the interaction of light with tissue requires complete measurements of absorption coefficient, scattering coefficient and the phase function. To evaluate light flux variation in depth with a medium, two different approaches could be used;

1. Direct measurements with a suitable probe¹
2. External description by means of theoretical models.^{2 3}

Various approaches to solve the theoretical models have been used, i.e. the Kubelka-Munk two flux model⁴, the Radiative transfer theory and Monte Carlo computer simulation of individual photon interactions⁵. Agreement between theoretical results is rarely found.

This chapter describes an implementation of the Kubelka-Munk two flux model with the radiative transfer theory for analysing the measurements of optical properties of Soyacal, pigs lung, human lung and human necrotic lung tissue using an integrating sphere. Various techniques for measuring optical properties of tissues have been reported^{6 7 8} over the past ten years. Cheong et al⁹ compiled a list of optical properties for human and animal tissues reported by many researchers. The accuracy of the optical properties for these tissues depends on the experimental conditions utilised and on the theoretical model and data correction techniques used. This explains the significant variations in optical properties reported by researchers for tissue samples.

Other than the goniometric measurements, the majority of techniques to measure the optical properties of tissue involve the use of integrating spheres. For convenience, transmitted flux and reflected flux associated for a one dimensional slab geometry will be called transmission and reflection respectively. An integrating sphere was used to measure the diffuse transmission and reflection of a sample by placing the sample at the front and rear of the integrating sphere. A measurement of the reflection, transmission and the sample thickness allows the determination of Σ_a and Σ_s (absorption and scattering coefficients) by using the Kubelka – Munk two flux model combined with the radiative transfer equation. Use of an integrating sphere as a means to measure the reflectance or the transmittance of a sample is an established technique.^{10 11 12}

5.2 Kubelka-Munk Theory

The transport theory describes the propagation of intensities in randomly distributed particles in terms of the specific intensity $I(r, \hat{s})$. This, in general, is a function of position r and direction \hat{s} in three-dimensional space. For a problem containing a plane parallel random medium illuminated by a plane wave normally incident upon it, the specific intensity is a function of one dimension z and one angle θ . An approximate method called the two - flux theory has been extensively used and is called the Kubelka – Munk (KM) solution.¹³ This is based on a two-stream approximation. Instead of solving the full transfer equation only streams up and streams down are considered. It has been found that the two-flux theory adequately describes the experimental results if the illumination is diffused and the medium causes the light to diffusely scatter.

The Kubelka – Munk solution involves two diffuse fluxes (W/m^2), one travelling in the positive z direction $F_+(z)$, and one travelling in the negative z direction, $F_-(z)$. Within a differential distance dz , the positive flowing flux, F_+ decreases due to absorption within dz and scattering in the backward direction as in figure 5.1

The loss from the forward flux F_+ (W/cm^2) travelling through a very short path length dz due to absorption and scattering is

$$(dF_+)_{loss} = -(K + S)F_+ dz \quad (5.1)$$

Where K and S are the Kubelka – Munk absorption and scattering coefficients respectively. The forward flux is increased due to scattering contribution from the backward flux F_- .

$$(dF_+)_{gain} = SF_- dz \quad (5.2)$$

Similar results hold for F_- except that F_- travels in an opposite direction of dz . F_- decreases by the amount

$$(dF_-)_{loss} = (K + S)F_- dz \quad (5.3)$$

and increases by the amount

$$(dF_-)_{gain} = -SF_+ dz \quad (5.4)$$

The following differential equations are obtained

$$\frac{dF_+(z)}{dz} = -(K + S)F_+(z) + SF_-(z) \quad (5.5)$$

$$\frac{-dF_-(z)}{dz} = -(K + S)F_-(z) + SF_+(z) \quad (5.6)$$

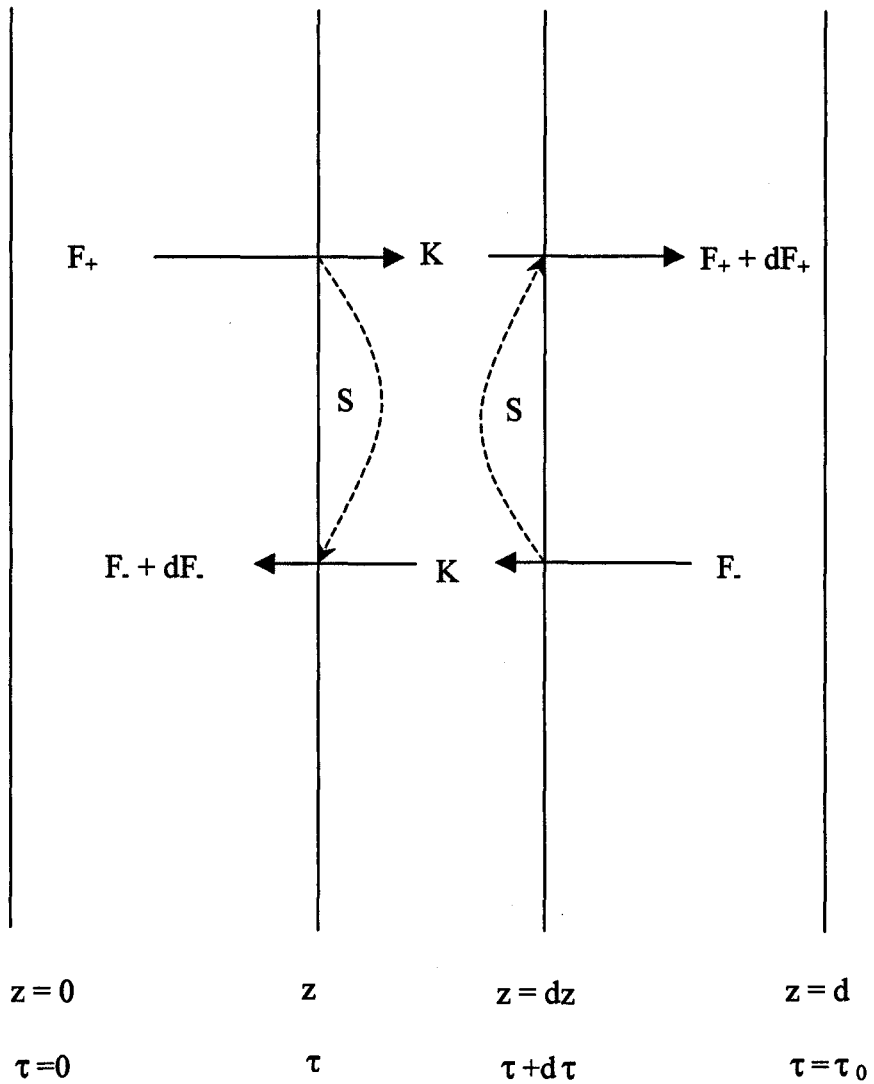


Figure 5.1 Kubelka – Munk theory for positive and negative flowing fluxes F_+ and F_- .
 K and S represent absorption and scattering respectively.

Isotropic scattering, absorption and scattering coefficients can be determined by measuring diffuse reflection and diffuse transmission for a thin slab of tissue. From these measurements the K – M absorption and scattering coefficients, K and S respectively can be calculated using the following relationships.¹⁴

$$S = \frac{1}{bd} \ln \left[\frac{(1 - aR + bR)}{T} \right] \quad (5.7)$$

$$K = (a - 1)S \quad (5.8)$$

where R = Reflection, T = transmission and

$$a = \frac{(1 + R^2 - T^2)}{2R} \quad (5.9)$$

$$b = \sqrt{(a^2 - 1)} \quad (5.10)$$

This method employs an integrating sphere to measure the reflection and transmission values for K and S.

Kubelka – Munk coefficients K and S computed from measurements of diffuse reflection and collimated diffuse transmission can be used to calculate absorption and scattering coefficients of the radiative transfer equations Σ_a and Σ_s .¹⁵

Consider a thin slab of tissue irradiated with diffuse light and assume that the tissue refractive index is equal to that of the environment. Equations (3.49), (3.50) and (3.51) with $F_c(z) = 0$, reduces to a KM like result, with equations (5.5) and (5.6)

$$K = 2\Sigma_a \quad (5.11)$$

$$S = \frac{3}{4} \{ \Sigma_a + (1 - g)\Sigma_s \} - \Sigma_a = \frac{3}{4}(1 - g)\Sigma_s - \frac{1}{4}\Sigma_a \quad (5.12)$$

5.3 Single Integrating Sphere theory

To measure the reflected and transmitted light from a sample using an integrating sphere, the sample is placed at the exit or the entrance ports of the sphere. The integrating sphere theory accounts for the losses caused by absorption at the sphere walls and light escaping the sphere. The power detected depends on the total light remaining within the sphere and on the relative size of the detector (to the total sphere area).^{16 17} Therefore, the voltage given by the detector output will be directly proportional to the total light power incident upon the detector.

With knowledge of the integrating sphere coefficients and by placing a sample at either the exit port or entrance port of an integrating sphere the reflected voltage V_R and transmitted voltages V_T of the sample, when illuminated by either diffuse or collimated light are obtained. The reflectance R and transmittance T (previously mentioned in the Kubelka – Munk model) values for the sample can then be obtained by using the equations presented in this chapter.

In this chapter the notation is as follows:-

P = the Power of the incident light

P_d = the power incident on the detector

R_c = the coefficient for the collimated (specular) reflection

R_{cd} = the coefficient for collimated diffuse reflectance of the sample.

R_d = the coefficient for diffuse reflectance of the sample

A_s = sample area

A = inner surface area of the complete sphere

A_d = the detector area

A_a = the sum of the area of all other ports

m = coefficient of reflectance of the sphere

α = fraction of the total sphere area occupied by the sphere wall

Diffuse irradiance of sample

When light enters an integrating sphere and is incident upon the sphere wall with power P as in figure 5.2(a) the total power reflected is¹⁸

$$mP \tag{5.13}$$

This is for the first reflection and m is the coefficient of reflectance of the sphere wall. Since the source of the light incident upon the sample is diffuse, this measurement is referred to as diffuse incidence light. The reflected power is distributed uniformly over the whole wall as the sphere wall is a Lambertian surface. For the first reflection a detector of surface area A_d will collect

$$\frac{A_d}{A} mP \tag{5.14}$$

where A is the total inner surface of the sphere (including the sphere wall, the detector, the sample and the ports).

The total light collected by the sample is

$$\frac{A_s}{A} mP \tag{5.15}$$

where A_s is the area of the sample.

The total light lost through the ports is

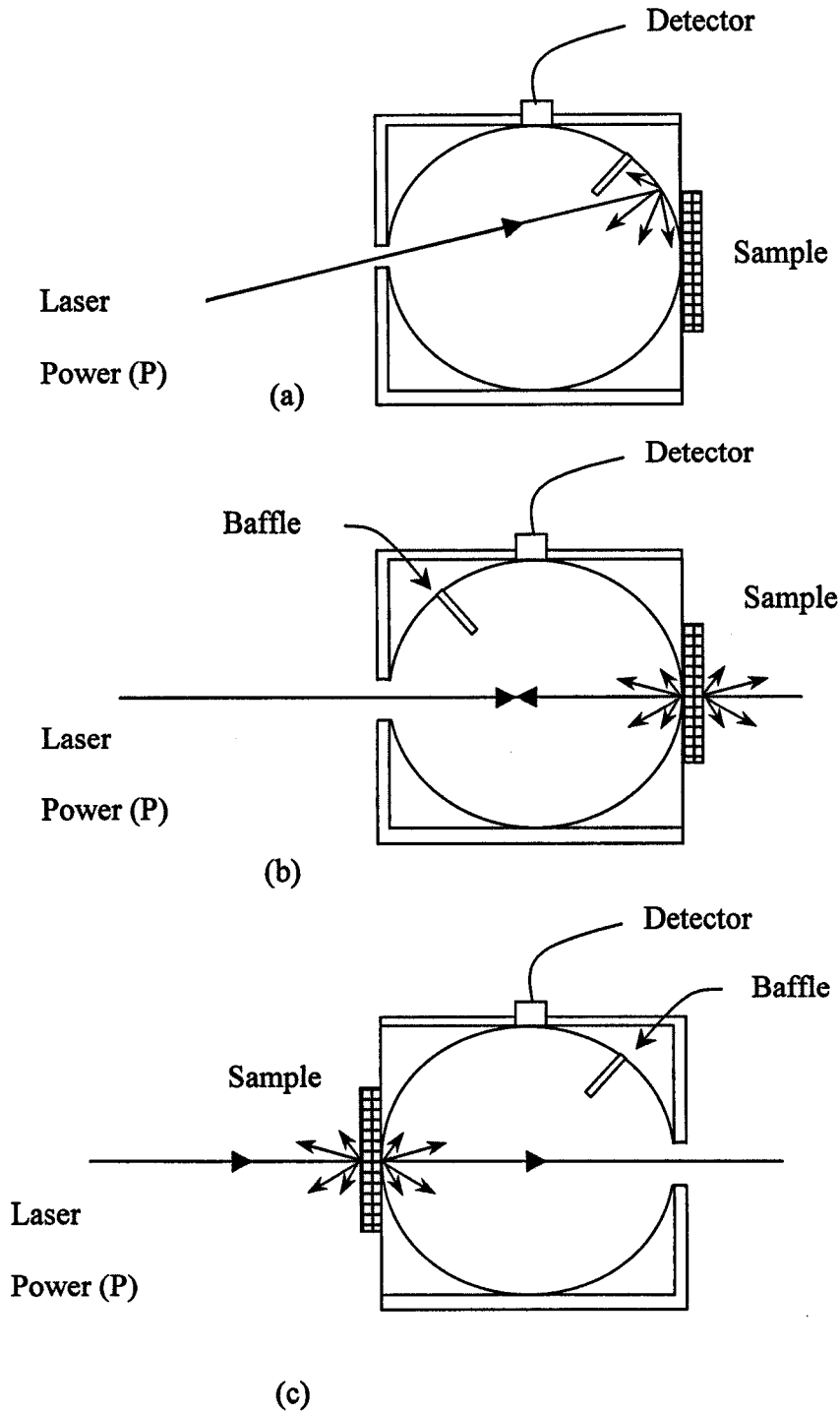


Figure 5.2 Integrating Sphere Measurements: (a) The light beam is incident upon the sphere wall for diffuse irradiance measurements. (b) Collimated light is incident upon the sample for reflection measurements. (c) Beam is incident upon the tissue for transmittance measurements. The light that is not scattered within the sample is then allowed to pass out of the integrating sphere.

$$\frac{A_a}{A} mP \quad (5.16)$$

where A_a is the sum of the areas of all the ports in the sphere

The total light collected by the walls of the sphere from the first reflection is

$$cmP \quad (5.17)$$

$$\text{where } \alpha = \frac{[A - (A_s + A_d + A_a)]}{A} \quad (5.18)$$

A fraction r , where r is the reflection coefficient of the detector, of the total power from the first reflection incident on the detector is reflected by the detector. Similarly a fraction m will be reflected from the wall of the sphere and a fraction R_d will be reflected from the sample (R_d is the diffuse reflection coefficient). The total reflected light of the second reflection will be

$$r \frac{A_d}{A} mP + mcmP + R_d \frac{A_s}{A} mP = mPF \quad (5.19)$$

$$\text{where } F = r \frac{A_d}{A} + m\alpha + R_d \frac{A_s}{A} \quad (5.20)$$

F is the fraction of the total incident light that is diffusely reflected by all the components of the sphere. Now from the second reflection the power is distributed around the sphere so that the detector collects

$$\frac{A_d}{A} mPF \quad (5.21)$$

the wall collects

$$cmPF \quad (5.22)$$

and the sample collects

$$\frac{A_s}{A} mPF \quad (5.23)$$

From the third reflection the detector collects

$$\frac{A_d}{A} mPFF \quad (5.24)$$

and so on i.e. the detector collects from the n th reflection a power of

$$\frac{A_d}{A} mPF^{n-1} \quad (5.25)$$

Summing the collected power for $n=1$ to $n=\infty$, the total power collected by the detector is

$$P_d = \frac{A_d}{A} mP(1 + F + F^2 + F^3 + \dots + F^{n-1} + \dots) \quad (5.26)$$

As $F < 1$ then

$$P_d = \frac{A_d}{A} \frac{m}{1-F} P \quad (5.27)$$

For any one reflection, energy is conserved. Since the source of the light incident upon the source is diffuse it is referred to as diffuse incidence as opposed to collimated incidence in which the light is incident directly upon the sample.

Baffle Effects

A baffle is placed between the incident light striking the wall or sample and the detector. This avoids the direct measurement of specularly reflected light from either the sample or sphere wall. Since the baffle is placed between the first reflected light from either the sphere or sample and the detector, the reflection from the detector is neglected. The reflection from the detector is small compared with the reflection from the baffle, walls and sample.

Diffuse Reflectance

The reflectance measurement of a sample can be generated using diffuse irradiance of the sample by collimated light entering the sphere and irradiating the sphere wall. The total power incident on the detector P_d has been quoted by Pickering et al.¹⁸ to be

$$P_d = \frac{b_1 \left(1 - R_d \frac{A_s}{A} \right)}{1 - b_2 R_d} P \quad (5.28)$$

where P is the power of the incident light, R_d is the diffuse reflectance of the sample for diffuse light and the sphere coefficients b_1 and b_2 are defined as

$$b_1 = \frac{A_d}{A} \frac{m}{1 - m\alpha} \quad b_2 = \frac{A_s}{A} \frac{1}{1 - m\alpha} \quad (5.29)$$

Collimated Incident Light

The diffuse reflection measurement can be generated by collimated light entering the sphere and irradiating the sample as in figure 5.2(b).

$$P_d = \frac{b_1(\alpha R_{cd} - R_c)}{1 - b_2 R_d} P \quad (5.30)$$

where R_{cd} is the diffuse reflectance of the sample for collimated irradiance and R_c is the specular Fresnel reflection of the sample for collimated irradiance. If the collimated light is allowed to pass out of the sphere then $R_c = 0$. It was shown by Pickering et al.¹⁸ that collimated irradiance gives a much more accurate measurement than diffuse light on samples when using an integrating sphere.

To measure the transmittance, a sample situated at the entrance port of the integrating sphere is illuminated with collimated light with power P as in figure 5.2(c). The power collected by the detector P_d will be the sum of the multiple reflected light as for the diffuse intensity. Therefore

$$P_d = \frac{b_1 \alpha T_{cd}}{1 - b_2 R_d} P \quad (5.31)$$

where T_{cd} is the diffuse transmission coefficient of the sample when illuminated by collimated light.

Sphere Measurements

The detected power of relevance to the measurement of optical properties is

$$P_d = \frac{1}{K}(V_1 - V_0) \quad (5.32)$$

where V_1 is the signal in the presence of the light source and V_0 in its absence (V_0 originates from noise and / or stray light) and K is a constant relevant to the detector responsivity.

The incident power P can be measured directly, but measurements relative to the power using a diffusely reflecting plate, coated with the same material as the integrating sphere and termed the standard reference plate R_{ref} are used for convenience.

$$P_{d,ref} = P\phi(R_{ref}, A_s, A, A_a, m) \quad (5.33)$$

where ϕ is the constant for a given sphere geometry.

Combining equations (5.32) and (5.33)

$$P = \frac{P_{d,ref}}{\phi} = \frac{\frac{1}{K}(V_{ref} - V_{ref,0})}{\phi} \quad (5.34)$$

where V_{ref} is the voltage measured with the standard reference plate positioned at the exit port of the integrating sphere and $V_{ref,0}$ is the background measurement with no reference plate as in figure 5.3(a). Combining equations (5.32) and (5.34) the ratio of the detected power to the incident power is

$$\frac{P_d}{P} = \phi \frac{(V_1 - V_0)}{(V_{ref} - V_{ref,0})} = \phi V_{R/T} \quad (5.35)$$

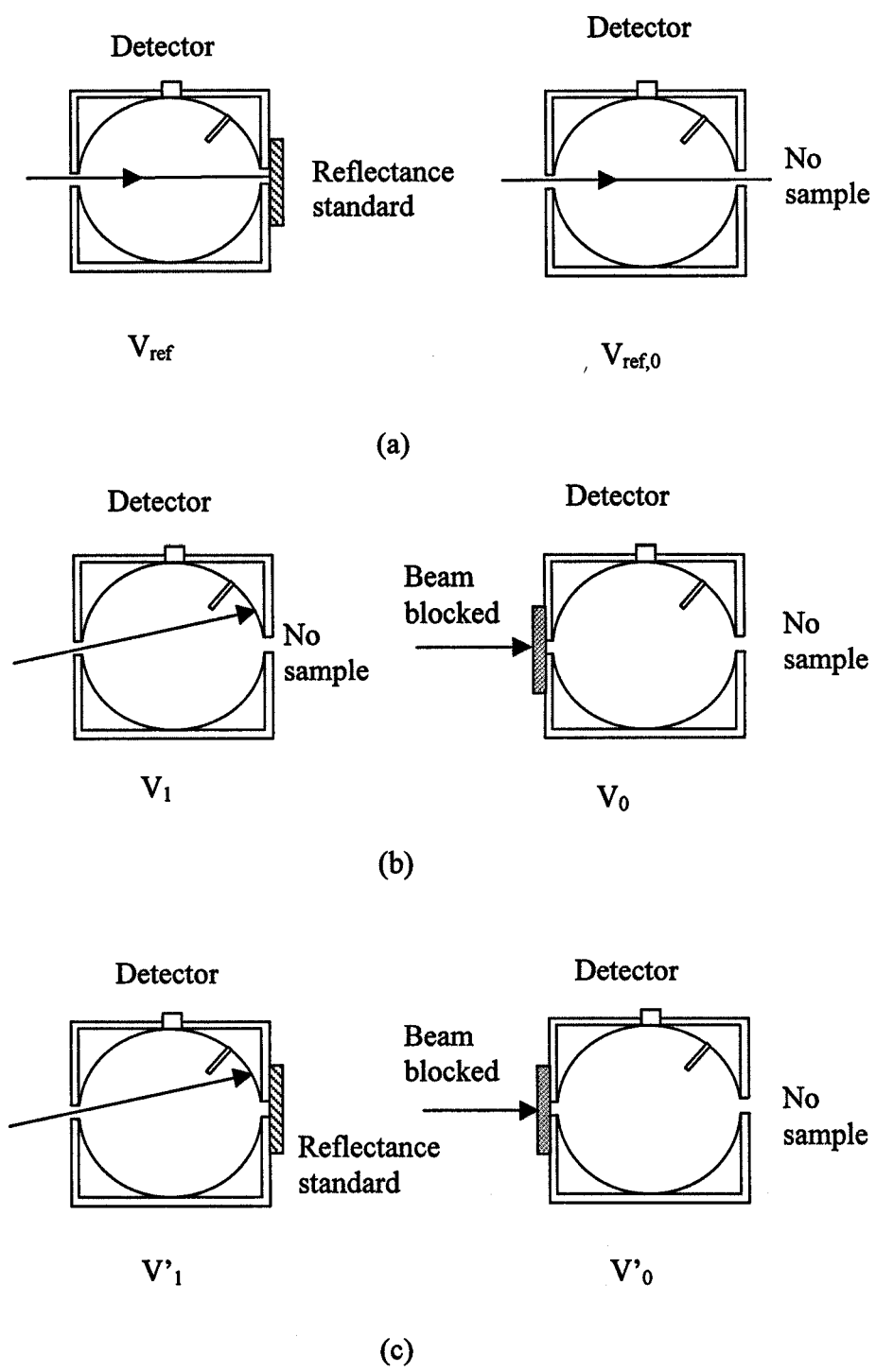


Figure 5.3 Integrating sphere measurements: (a) Reference measurements V_{ref} and $V_{ref,0}$ (b) Determining sphere coefficient b_1 . (c) Determining sphere coefficient b_2

which is independent of K and V_{RT} will be discussed later.

Finally it is noted from equations (5.28), (5.30) and (5.31) the ratio of detected and incident powers can be written as

$$\frac{P_d}{P} \propto b_1 \quad (5.36)$$

and therefore b_1 can be defined as

$$b_1 \equiv b_1 \frac{1}{\phi} \quad (5.37)$$

The need to measure the power is now eliminated and the reflectance of the sample can be determined from four measured voltages ($V_1, V_0, V_{ref}, V_{ref,0}$) and a knowledge of the sphere constants.

The subscript (R/T) after the voltage symbol (ie $V_{R/T}$) indicates the reflection and transmission terms and both have been normalised to a baseline. All values lie between 0 and 1.

$$V_{R/T} = \frac{V_{measure} - V_{nothing}}{V_{ref} - V_{ref,0}} \quad (5.38)$$

where $V_{measure}$ is the measurement of the sample, reflectance standard or sphere wall, $V_{nothing}$ is the measurement when there is no light in the sphere either by passing through the sphere or being blocked at the entrance depending on reflection or transmission measurements. The reference voltages are measured as in figure 5.3a with V_{ref} being measured with the reflectance standard at the exit port and $V_{ref,0}$ measured with the light passing unhindered through the entrance and exit ports of the sphere.

Determining Sphere Coefficients

The sphere coefficient b_1 can be determined when a collimated beam hits the sphere wall (producing diffuse light) with no sample present as in figure 5.3b. Then R_d in equation (5.28) is equal to zero with V_R in place of P_d/P therefore,

$$b_1 = V_R = \frac{V_1 - V_0}{V_{ref} - V_{ref,0}} \quad (5.39)$$

where V_1 is the measured voltage when the collimated beam hits the sphere wall and V_0 is the measured voltage when the beam is blocked from entering the sphere as in figure 5.3(b). The voltage $V_{ref,0}$ can be determined when the beam, normal to the sphere, passes through the entrance and exit ports unhindered and V_{ref} can be obtained when the beam normal to the sphere hits a reflectance standard at the exit port as in figure 5.3(a). The sphere coefficient b_1 was found to be 0.699.

To determine b_2 a standard reference plate is placed at the exit port of the sphere with the collimated light hitting the sphere wall producing diffuse light as in figure (5.3c).

$$V'_R = \frac{V'_1 - V'_0}{V'_{ref} - V'_{ref,0}} \quad (5.40)$$

The measurements V'_1 and V'_0 are made when the beam hits the reflectance standard at the exit port and when the beam is blocked at the entrance port respectively.

Rearranging equation (5.28) with V'_R in place of P_d/P

$$b_2 = \frac{V'_R - b_1 + b_1 R_{ds} \frac{A_s}{A}}{V'_R R_{ds}} \quad (5.41)$$

where R_{ds} is the known diffuse reflectance of the standard reflectance plate given by the manufacturer to be 0.988 hence b_2 was found to be 0.077.

When collimated light is incident on a sample there is a factor α in equation (5.30) which can be resolved by measuring the area of the detector, sample, sphere and sphere ports as in equation (5.18) and was found to be 0.981. By rearranging b_1 and b_2 in equation (5.29) the sphere reflectance (m) was determined

$$m = \frac{-\frac{A_s}{A} + b_2}{\alpha b_2} \quad (5.42)$$

The sphere reflectance (m) was found to be 0.984

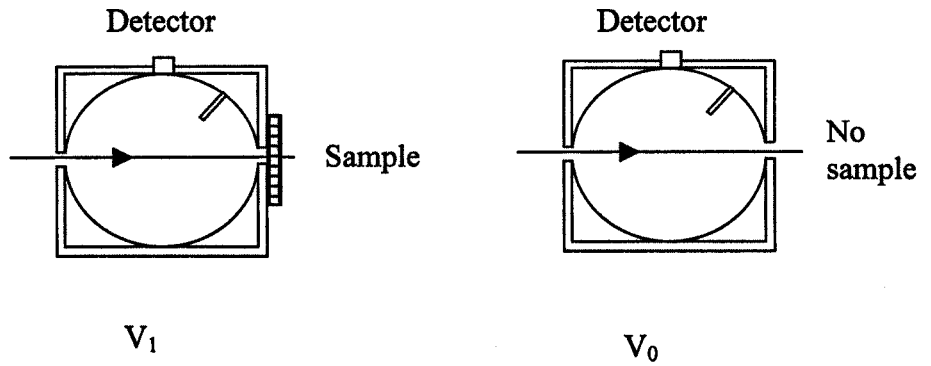
Determining the reflectance R and transmission T

The reflectance and transmission voltages V_R and V_T of a sample can be found using

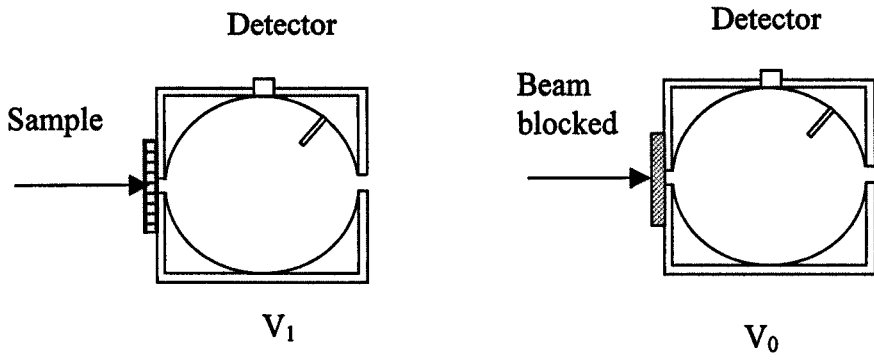
$$V_{R/T} = \frac{V_1 - V_0}{V_{ref} - V_{ref,0}} \quad (5.43)$$

where the reference voltages V_{ref} and $V_{ref,0}$ are measured as before.

To measure the reflectance voltage V_R the sample is placed at the exit port of the integrating sphere and the voltage V_1 measured. The voltage V_0 is obtained by removing the sample and having the exit port empty as in figure 5.4(a). Similarly the transmission voltage V_T is obtained by placing the sample at the entrance port of the integrating sphere and measuring the voltage V_1 . The entrance port is then blocked allowing no light to enter the sphere to determine V_0 as in figure 5.4(b).



(a)



(b)

Figure 5.4. Integrating sphere measurements to determine V_R and V_T

Finally the diffuse reflectance using collimated light R_{cd} of the sample can be determined by using equation (5.30). By replacing P_d/P by V_R and using the sphere coefficients given earlier then the reflectance of the sample can be found. It must be noted that an assumption is made that $R_{cd} = R_d$ and when the light exits the sphere then $R_c = 0$ as in figure 5.4(a). Similarly the diffuse transmission coefficient for collimated light T_{cd} of the sample can be found by using the equation (5.31).

The coefficients R_{cd} and T_{cd} for the reflection and transmission of diffuse light for collimated light are identical to the values R and T respectively given in the Kubelka – Munk two flux model for diffuse light as in equations (5.7) and (5.9).

5.4 Experimental Methods

Three measurements are required to determine three unknowns. Two possible sets of measurements are the diffuse reflection, the total transmission and the collimated transmission or the diffuse reflection, the total transmission and the phase function. For optically thick samples it is impossible for the commonly used collimated on-axis transmission measurement to estimate the residual scattered component of the on-axis transmission. Therefore the latter set of measurements including the phase function were used.

Experimental Apparatus

A four-inch internal diameter integrating sphere was used to measure the diffuse reflection and the total transmission of the samples as in figure 5.5. The integrating sphere had three 1-inch diameter ports and one 0.5-inch diameter port. The unused

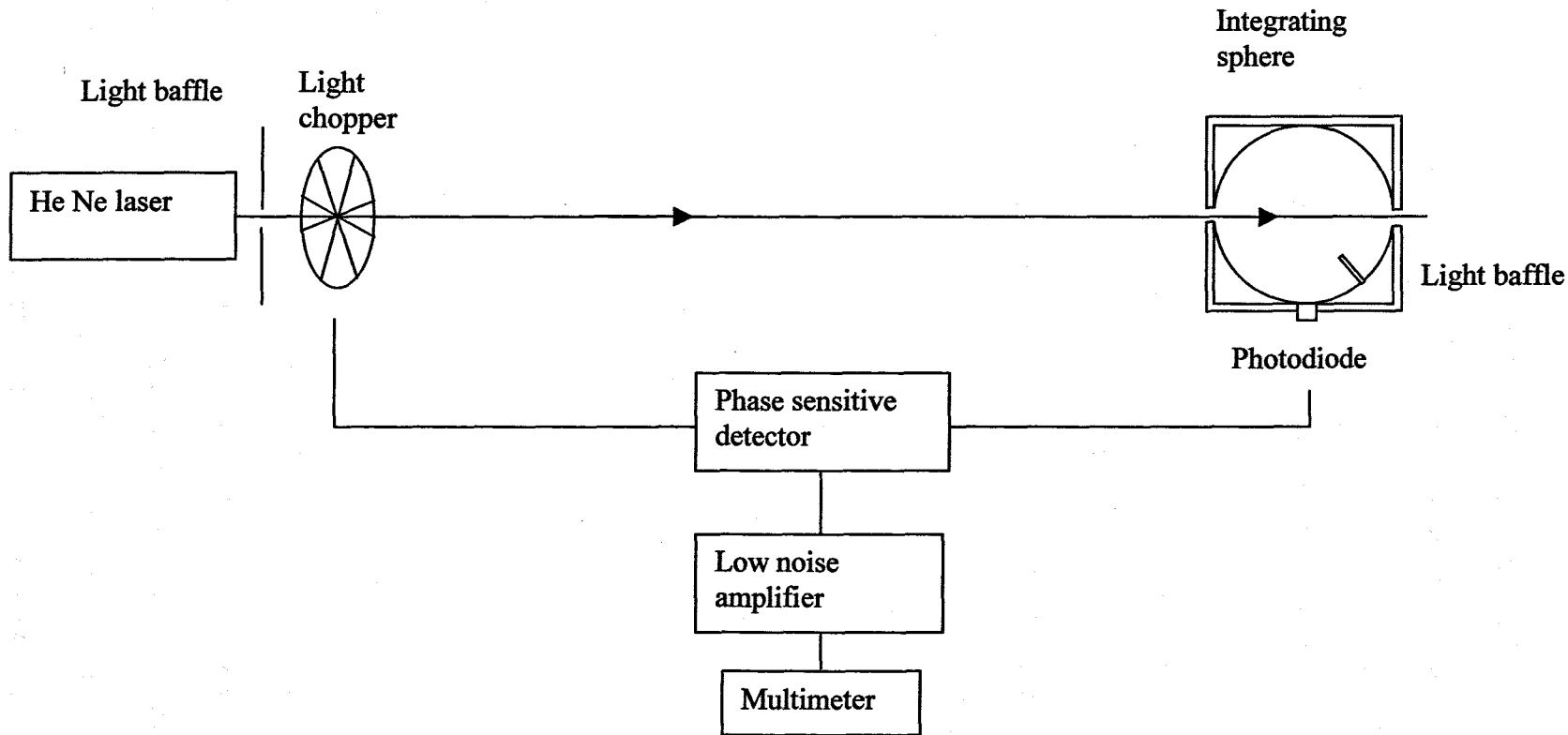


Figure 5.5 Experimental arrangement for measuring the attenuation coefficients Σ_a and Σ_s various samples

ports were covered with standard reference plates with the same coating as the integrating sphere. The sample was placed beside the 0.5 inch diameter port and a one inch entrance port used for the laser beam. The samples were attached to the integrating sphere by two hairsprings. The light baffle was placed between the sample and the detector to reduce directly reflected or transmission measurements.

A 5mm² photodiode placed behind a 3mm diameter hole cut into a standard reflectance plate was connected to a one inch port. A 1mW HeNe laser beam passed through a Rofin Sinar light chopper operating at 100Hz. The light chopper provided a reference signal for a phase sensitive detector and a lockin amplifier, which minimised the noise from the 50 Hz AC pickup and ambient lighting. The voltage from the photodiode was amplified using a Brookdale electronics Ltd. low noise amplifier (450) which was connected to a Thurlby digital intelligent multimeter (1905a). With thin samples it was necessary to place neutral density filters in the path of the laser beam to avoid the detector saturating.

Tissue Preparation

Tissue preparation was achieved using the same method as described in Section 4.4. For pig lung and Soyacal solutions new preparations were made for both the goniophotometer measurements and the integrating sphere measurements. For human necrotic tissue, the sample was used for both goniophotometer and integrating sphere measurements. The tissue was sealed as before between two glass slides with a glass adhesive applied to the surrounding edges of the glass slides. The time interval for both

experiments was no longer than one hour and no significant degradation of the tissue was apparent.

5.5 Results

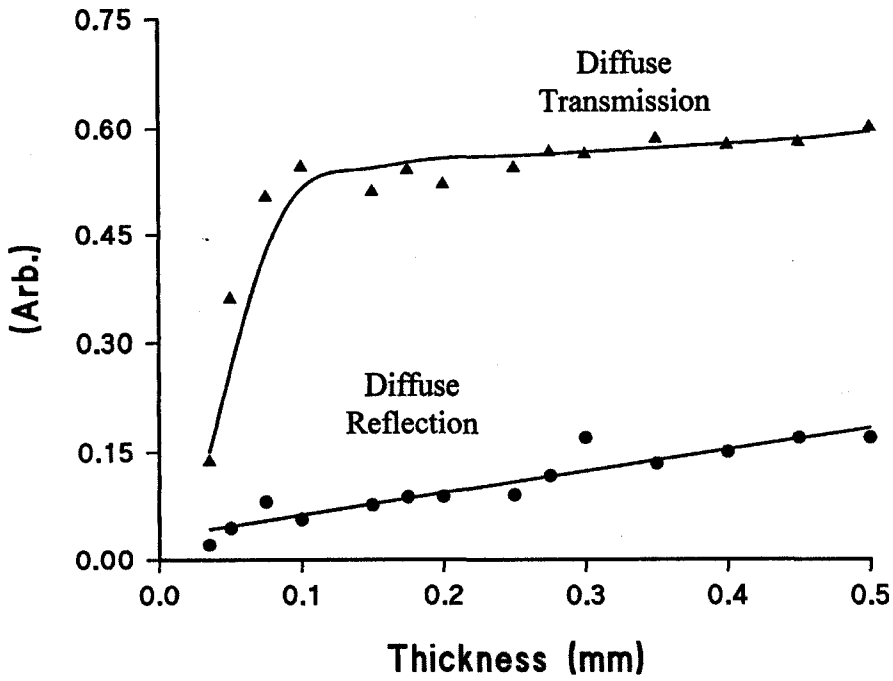
Measurements to find the sphere coefficients b_1 and b_2 (equation 5.29) were made first. These coefficients should remain constant throughout the experiments. This was confirmed by repeating the measurements in the final experiments. The coefficient b_1 was determined by using equation (5.39) and by the method shown in figure 5.3(a) and 5.3(b) to determine the individual components of equation (5.39) ie V_{ref} , V_{ref0} , V_1 and V_0 . The sphere coefficient b_1 was found to be 0.699. The second coefficient b_2 is found in a similar manner by using equation (5.41) and the method illustrated in figure 5.3(a) and 5.3(c) and was found to be 0.077. Using equation (5.42) the sphere reflectance m was found to be 0.984.

The reflection and transmission voltage measurements V_R and V_T of the samples were obtained by using equation (5.43). The values V_{ref} having been found by illuminating the reflectance standard at the exit port and $V_{ref,0}$ found by letting the light pass through the integrating sphere as in figure 5.3(a). The value V_1 was found by either placing the sample at the entrance port or exit port of the integrating sphere and V_0 was found by either blocking the light from entering the sphere or letting the light pass through the sphere as in figures 5.4(a) and 5.4(b).

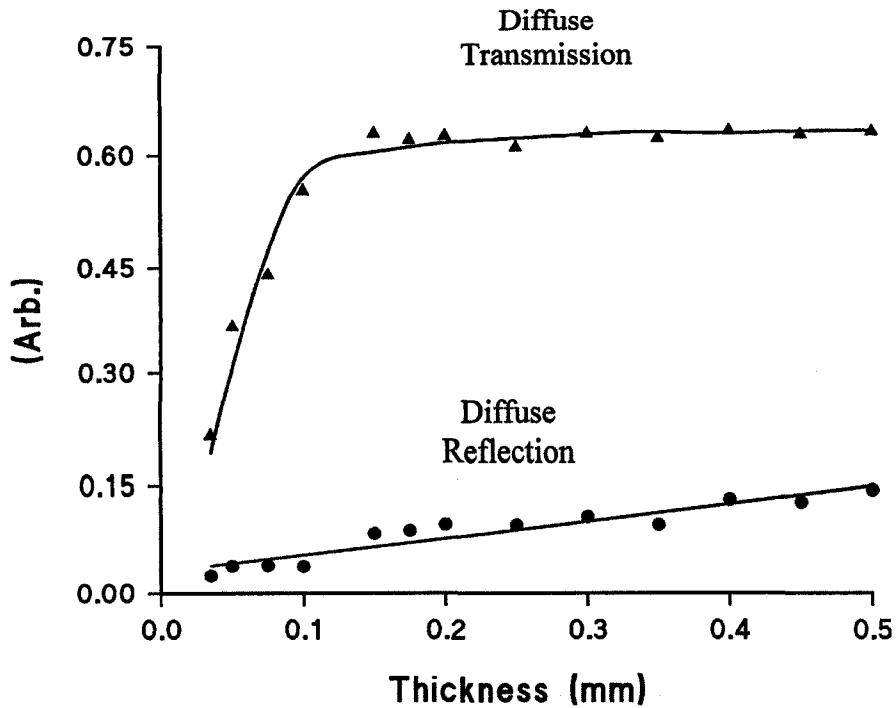
Replacing P_d/P by V_R and V_T in equations (5.30) and (5.31) and making the assumption that the diffuse reflection R_{cd} of collimated light is the same as the diffuse reflection R_d of diffuse incident light then the diffuse reflectance R_{cd} and transmission T_{cd} values for a sample were obtained. The coefficients R_{cd} and T_{cd} are the same as R and T respectively given in the Kubelka – Munk model. Once the reflection R and transmission T values had been obtained from the integrating sphere measurements, the absorption and scattering coefficients for the tissue were then computed based on the Kubelka – Munk solution of the transport equation. The Kubelka – Munk absorption and scattering coefficients K and S were calculated from equations (5.7) - (5.10). It is important to stress K and S must be distinguished from the absorption coefficient Σ_a and scattering coefficient Σ_s of the tissue. Values of K and S appear constant only after a certain optical depth as the light does not reach the diffusion mode for thin samples. Values of K and S were selected from samples whose coefficients do not vary much with respect to sample thickness.

The radiative transfer absorption and scattering coefficients Σ_a and Σ_s were evaluated from the Kubelka – Munk absorption and scattering coefficients K and S by equations (5.11) and (5.12). In equation (5.12) the anisotropy factor g is used. In chapter 4 the anisotropy factor is obtained for pig lung with and without blood, human necrotic tissue and Soyacal. It was these values that were used for each K and S conversion into radiative transfer absorption coefficient Σ_a and scattering coefficient Σ_s .

The measured reflection and transmission coefficients for various sample thickness of pig lung, pig lung without blood, Soyacal and human necrotic tissue can be seen in figures 5.6 and 5.7. Each point is an average of five samples, each sample was



(a)



(b)

Figure 5.6(a) Measured diffuse reflection and transmission for pig lung samples. (b) Measured diffuse reflection and transmission for samples of pig lung with no blood present

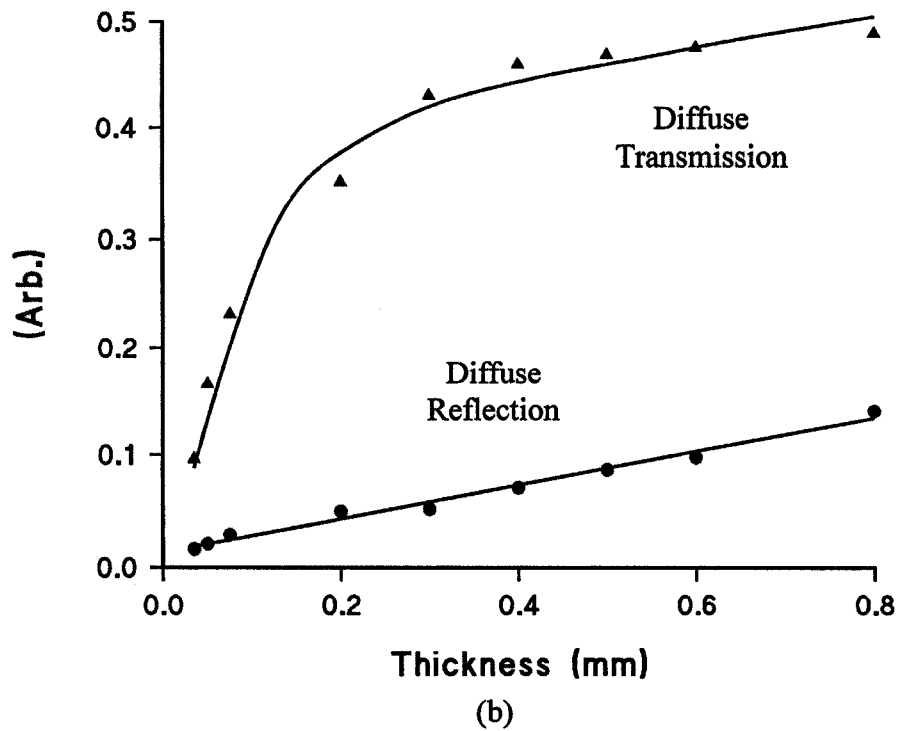
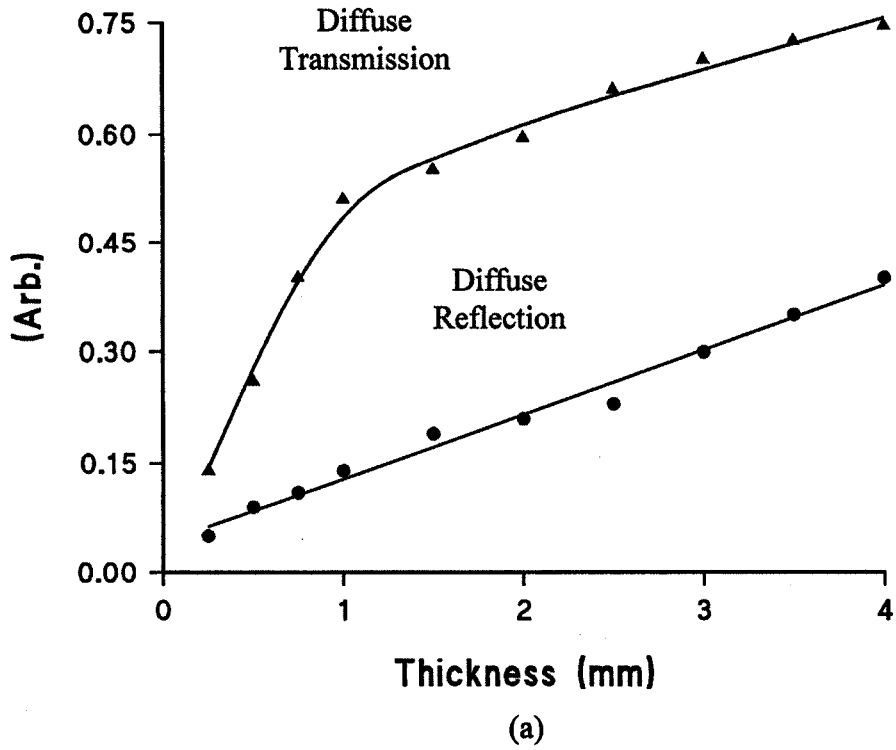


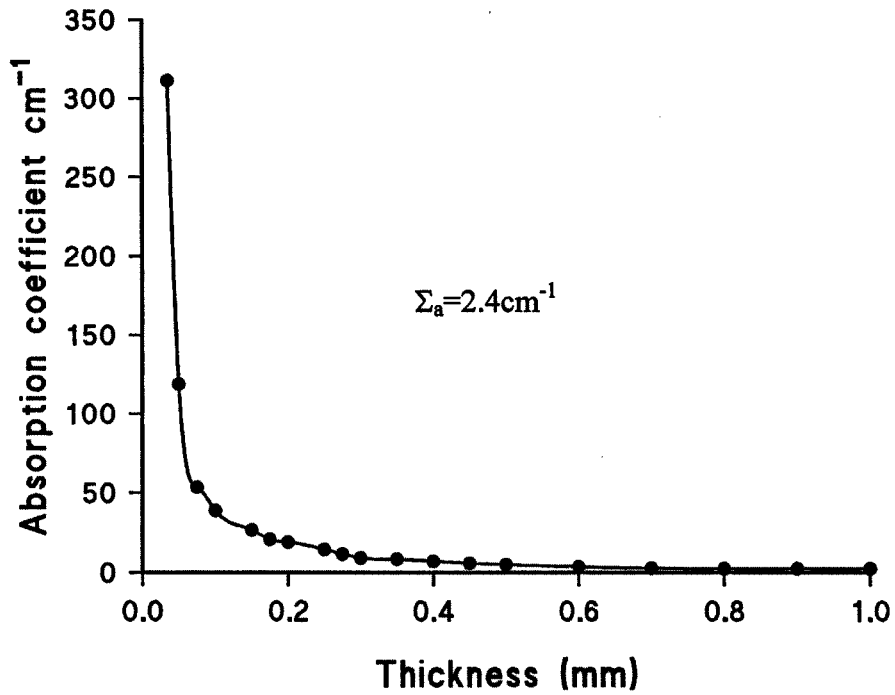
Figure 5.7 (a) Measured reflection and transmission for 1% of 10% Soyacal Solution. (b) Measured reflection and transmission for samples of human necrotic lung tumour

repositioned in the sample holder five times to achieve an average value per sample. Standard errors were quoted on the final results as this error varied significantly from point to point. The thickness of the pig lung samples ranged from 0.025mm to 1mm and the Soyacal cell thickness ranged from 0.25mm to 4mm. Since only one sample for each thickness of human necrotic lung tissue was available, each sample was moved in the sample holder ten times to achieve an average result per sample thickness that ranged from 0.25 μ m to 0.8 mm.

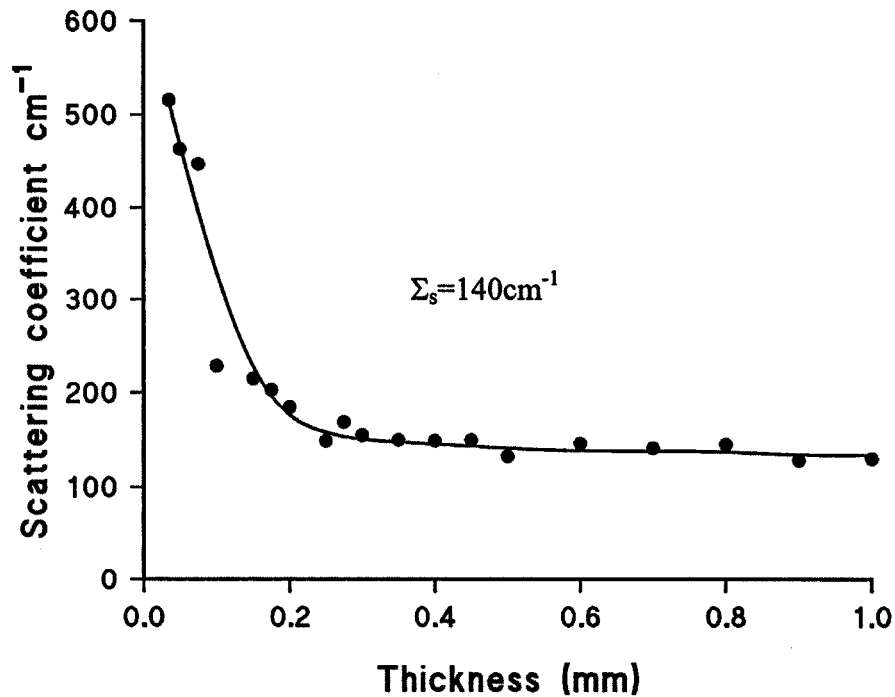
The absorption and scattering coefficients Σ_a and Σ_s for pig lung with and without blood present are plotted against tissue thickness in figures 5.8 and 5.9. Since for thin samples the light does not become diffuse, the values for the absorption and scattering coefficients are obtained from the graphs when the coefficients do not vary much with respect to thickness of the sample. The figures 5.8 and 5.9 yield $\Sigma_a = 2.4 \text{ cm}^{-1}$ and $\Sigma_s = 140 \text{ cm}^{-1}$ for pig lung samples and $\Sigma_a = 1.8 \text{ cm}^{-1}$ and $\Sigma_s = 71 \text{ cm}^{-1}$ for pig lung samples without blood present. Values of $\Sigma_a = 5 \times 10^{-4} \text{ mm}^{-1}$ and $\Sigma_s = 7.5 \text{ mm}^{-1}$ for Soyacal were also computed from the reflection and transmission measurements and are plotted against thickness in figure 5.10. Human necrotic tissue coefficients are plotted against thickness in figure 5.11 and are given as $\Sigma_a = 3.1 \text{ cm}^{-1}$ and $\Sigma_s = 66. \text{ cm}^{-1}$. The values for the coefficients are given in table 5.1.

5.6 Discussion

The theory of the integrating sphere allows an interpretation of reflectance and transmittance measurements of a sample. A large sample diameter compared with the



(a)



(b)

Figure 5.8(a) Absorption coefficient for pig lung computed from Kubelka-Munk theory using Radiative Transfer Theory. (b) Scattering coefficient for pig lung computed from Kubelka-Munk using radiative transfer theory

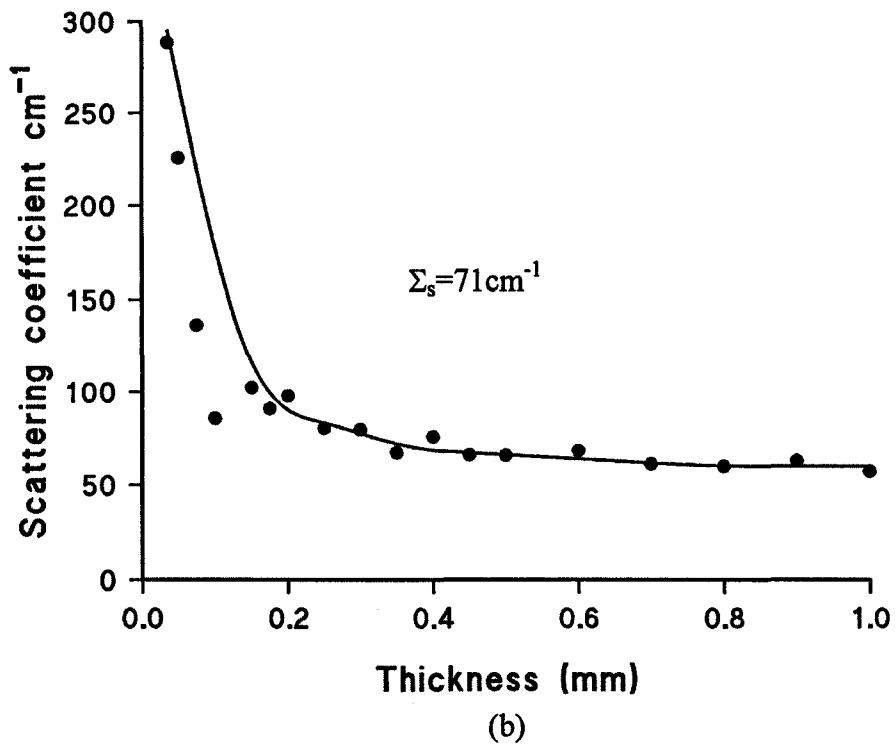
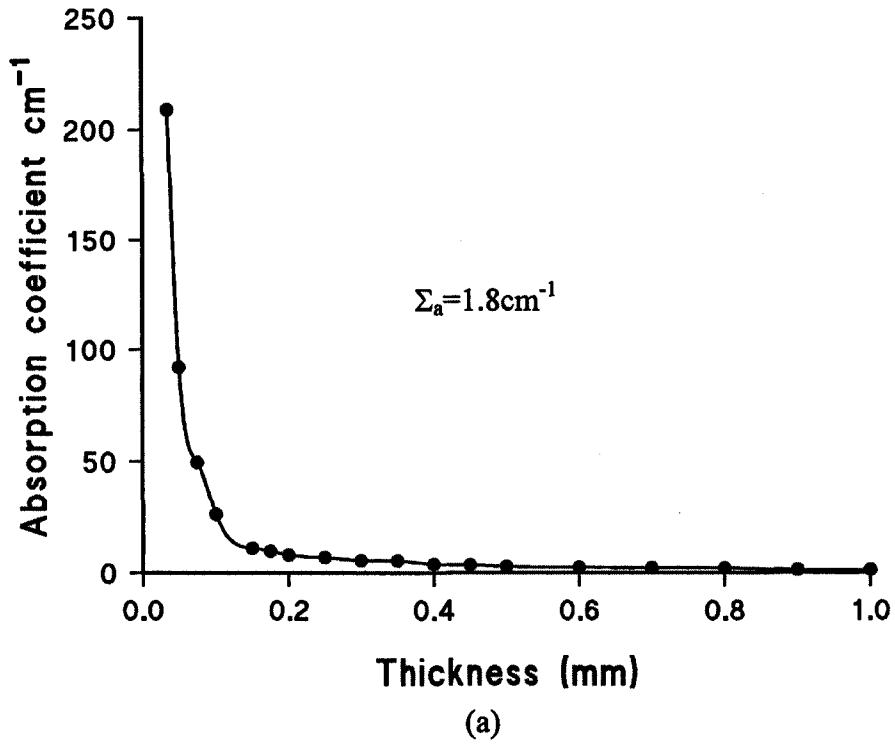


Figure 5.9(a) Absorption coefficient for pig lung (with no blood present) computed from Kubelka-Munk theory using Radiative Transfer Theory. (b) Scattering coefficient for pig lung (with no blood present) computed from Kubelka-Munk using Radiative Transfer Theory

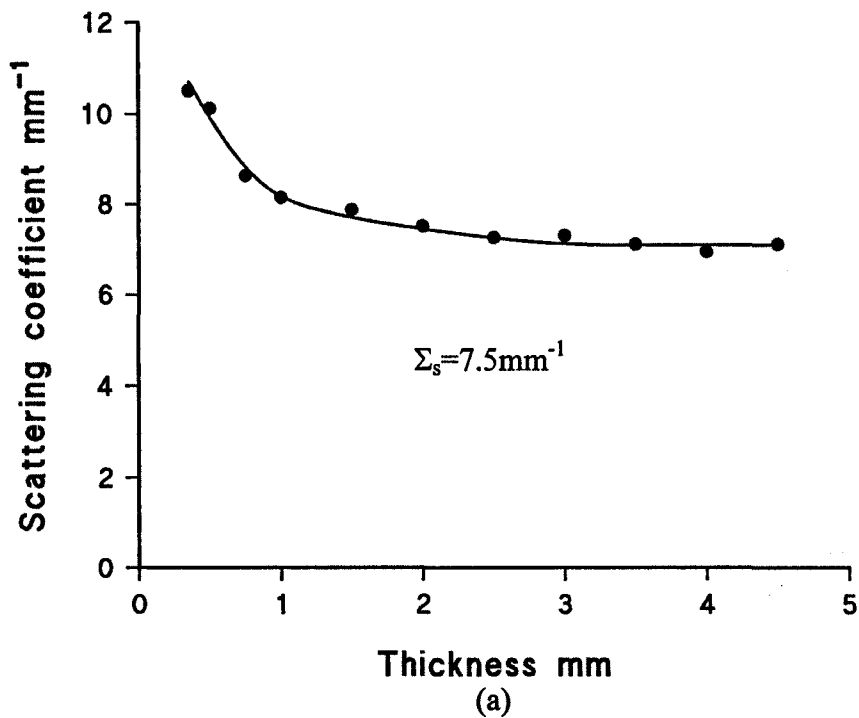
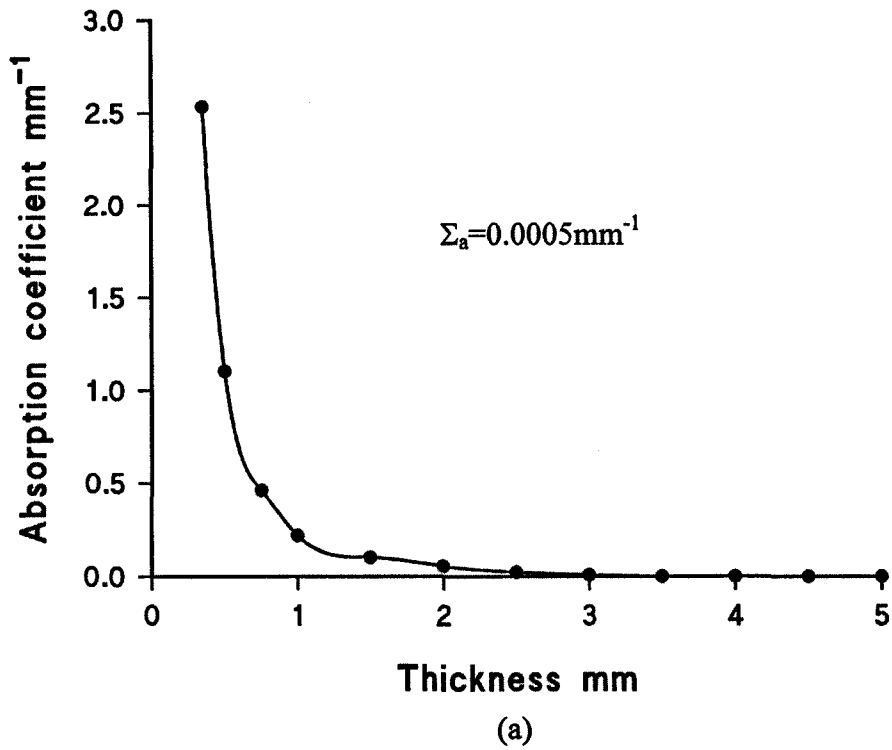


Figure 5.10(a) Absorption coefficient for Soyacal. (b) Scattering coefficient for Soyacal

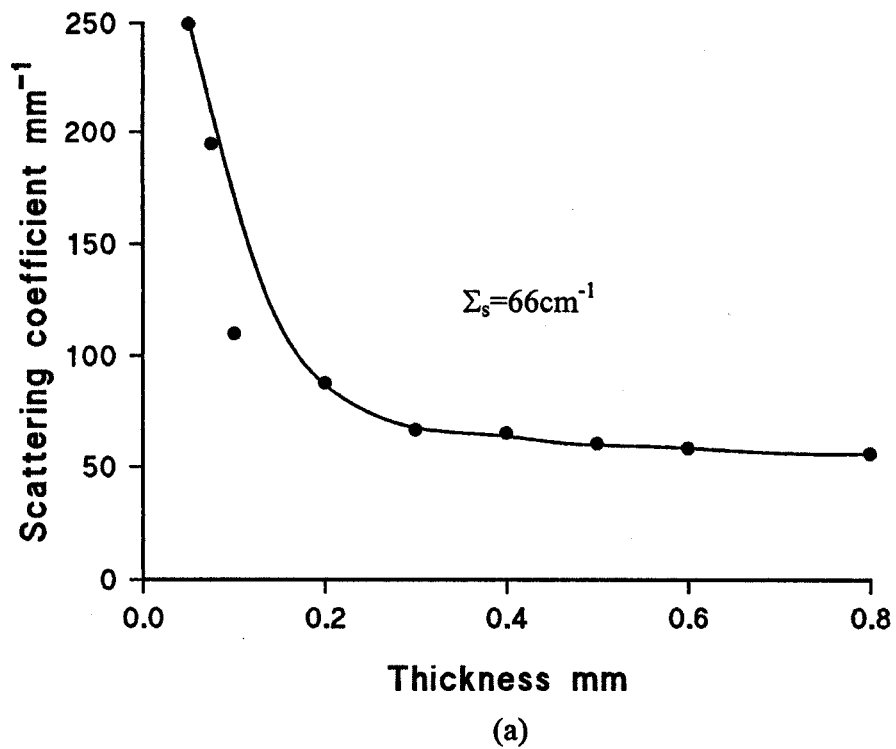
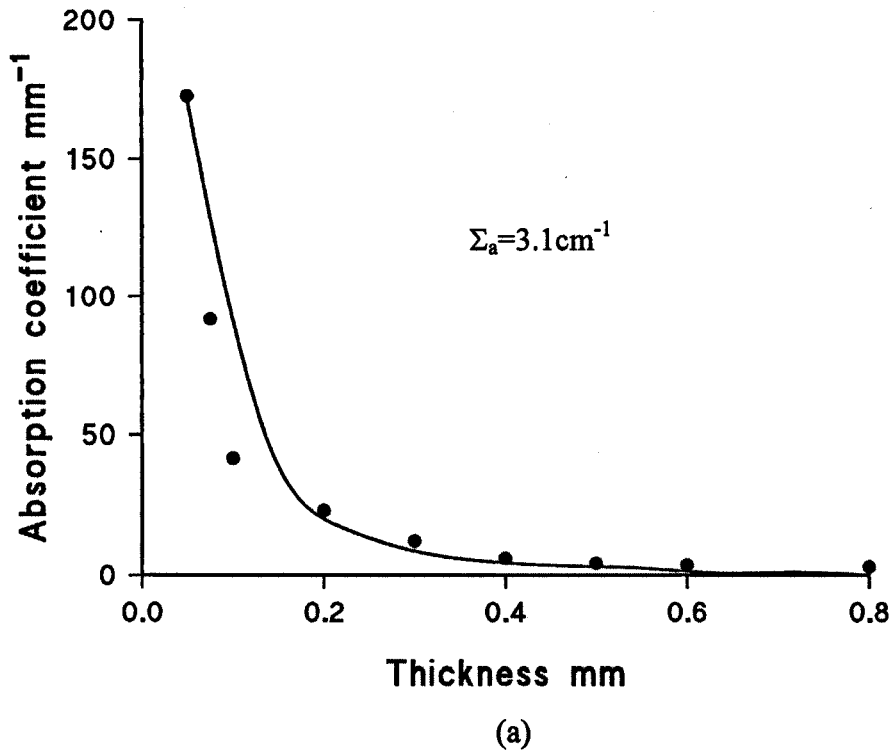


Figure 5.11(a) Absorption coefficient for human necrotic lung tissue computed from Kubelka-Munk using Radiative Transfer Theory.
 (b) Scattering coefficient for human necrotic lung tissue computed from Kubelka-Munk using Radiative Transfer Theory

beam diameter is necessary to avoid light loss through the side of the sample and by light transport down the glass slide. It has been suggested by Pickering et al.¹⁸ that collimated incident light is preferential to diffuse light. This is beneficial to lung tissue measurements, as tissue samples are not large enough to cover the port on the integrating sphere. Hence collimated light was used.

The methods which hypothesise isotropic scattering for tissue do not provide a reliable estimation of the optical properties since most tissues exhibit spatial inhomogeneity yielding apparent anisotropies. All tissues were measured at 633nm and observed to have strongly forward scattering behaviours. Table 5.1 shows the results from other researchers. At least three of the four parameters were given in each reference with the fourth result evaluated using the equation.

$$\Sigma_{eff}^2 = 3\Sigma_a[\Sigma_a + \Sigma_s(1-g)]$$

It is apparent that there is a large discrepancy between results from table 5.1, which can be accounted for by differences in the theoretical treatment and experimental methods. The relatively large variations in the optical properties of the tissue can probably be attributed to the optical non-homogeneity of the samples. An optically thick sample is described more uniform and more closely preserves the original tissue structure. It has been reported that there is considerable variation in the measured absorption coefficients of tissue as a function of sample thickness.¹⁹ Also the signal detected in reflection measurements is very sensitive to the integrating sphere geometry. Accurate measurement of reflection is more difficult than transmission in tissues.

Tissue	Σ_a cm^{-1}	Σ_s cm^{-1}	g	Σ_{Eff} cm^{-1}	Theory/ Experimental method	ref
Human tumour	1.2	240	0.95	6.5	IAD program /goniophotometry	25
Human normal	8.4	35.9	0.95	16	Beers law /goniophotometry	22
Human normal				11	Diffusion theory/ In situ	23
Human normal	8.1	324	0.75	44	Beers law/ goniophotometry	20
Bronchial mucosa				9.1	Beers law/ in situ	3
Pig lung with blood	$2.4 \pm$ 0.3	140 ± 21	$0.925 \pm$ 0.015	$9.6 \pm$ 0.9	Thesis :- K M and transport theory/ Integrating sphere, goniophotometry	Chpt 5
Pig lung without blood	$1.8 \pm$ 0.6	$72 \pm$ 10	$0.89 \pm$ 0.02	$7.2 \pm$ 0.9	As above	Chpt 5
Human tumour	3.1 ± 0.3	66 ± 10	$0.913 \pm$ 0.1	$9.0 \pm$ 1.5	As above	Chpt 5
Phantom	Σ_a mm^{-1}	Σ_s mm^{-1}	g	d_{Eff} mm^{-1}	Theory/ Experimental method	ref
1% of 10% Soyacal	0.0005	7	0.82	22.2	As above	Chpt 5
1% of 10% Intralipid	0.00026	6.1	0.69	26.7	Transport theory/ added absorber	24
1% of 10% Intralipid	0.0016	4.8	0.7	11.8	Transport theory/ added absorber	5

Table 5.1. Optical properties of lung tissue and optical phantoms in vitro.

The sample preparation method may have a significant influence on the consistency of results. Other researchers have used either tissue sandwiched between two glass slides or in situ measurements. Tissues that have been sandwiched between glass slides are usually frozen first, then microtomed to produce thin samples. Other researchers have used the microtome method to obtain thin samples then added phosphate buffered saline to prevent air bubbles. This method for measuring the thickness of the tissue, while accurate, leads to blood loss from the tissue and is not satisfactory for lung samples due to the air bubbles.

In principle the scattering coefficient can be determined by integrating these scattered flux measurements over all solid angles i.e. from the phase function experiments. However it is extremely difficult in practice to obtain absolute normalisation of the phase function since the signal strength is so small relative to the incident beam. An alternative is to place a sample in an integrating sphere²⁰.

It must be noted that Pickering et al.²¹ demonstrated a method of measuring simultaneously the reflection, diffuse and collimated transmission by two integrating spheres with the sample placed between the two spheres. In the experimental set-up a large optically uniform sample is required to cover the port, to prevent a substantial loss of light from around the edges of the sample. For bronchiole tissue, only small sections of an irregular shape can be obtained. The illumination of the sample has to be restricted to the area of the tissue. The two-sphere technique is thus not suitable for illumination for lung tissue measurements.

5.7 References

1. Marijnissen J, Star W, *Lasers Med. Sci.* **2**, 235 (1987)
2. Star WM, Marijnissen J P, van Gemert M J, *Phys. Med. Biol.* **33**, 437 (1988)
3. Welch A J, Yoon G, Van Gemert M J, *Lasers Surg. Med.* **6**, 488 (1987)
4. Kubelka P, *J. Opt. Soc. Am.* **38**, 338 (1948)
5. Wilson B C, Adam G, *Med. Phys.* **10**, 824 (1983)
6. Keijzer M, Kortum R R, Jacques S L, Feld M S, *Appl. Opt.* **28**, 4286 (1989)
7. Splinter R, Cheong W F, van Gemert M J C, Welch A J, *Lasers Surg. Med.* **9**, 37 (1989)
8. Graaff R, Dassel A, Koelink M, de Mul F F, Aarnoudse J, Zijlstra W, *Appl. Opt.* **32**, 435 (1993)
9. Cheong W F, PrahI S A, Welch A J, *IEEE J. Quant. Electron* **26**, 2166 (1990)
10. Jacques J, Kuppenheim H F, *J Opt. Soc. Am.* **45**, 460 (1954)
11. Goebel D G, *Appl. Opt.* **6**, 125 (1967)
12. Roos A, *Appl. Opt.* **30**, 486 (1991)
13. Kubelka P, *J. Opt. Soc. Am.* **38**, 448 (1948)
14. Kubelka P, Munk F, *Tech Phys*, **12**, 593 (1931)
15. van Gemert M J, Welch A J, Star W M, Cheong W, *L.I.M.S.* **2**, 295, (1987)
16. PrahI S A, Vitkin I A, Bruggemann U, Wilson B C, Anderson R R, *Phys. Med. Biol.* **37**, 1203, (1991)
17. Miller G E, Sant A J, *J. Opt. Soc. Am.* **48**, 828 (1958)
18. Pickering J W, Moes C J, Sterenborg H J, PrahI S A, Van Gemert M J, *J. Opt. Soc. Am. A* **9**, 621 (1992)
19. Cilesiz I F, Welch A J, *Appl. Opt.* **32**, 477 (1993)

20. Marchesini R, Bertoi A, Anreola S, Sichirollo A, Appl. Opt. **28**, 2318 (1989)
21. Pickering J W, Prah S A, Wierington N, Beek J F, Sterenborg H, Van Gemert M, Appl. Opt. **32**, 399 (1993)
22. Andreola A, Bertoni A, Marchesini R, Milloni E, LISM **8**, 142 (1988)
23. Doiron D, Svassand L O, Profio A E, Proc. SPIE **357** Lasers Surg. Med (1982)
24. Driver I, Feather J, King P, Dawson J B, Phys Med. Biol. **34**, 1927 (1989)
25. Qu J, MacAulay C, Lam S, Palcic B, Appl. Opt. **33**, 7397 (1994)

6 Effective attenuation coefficient in vitro and in vivo

6.1 Introduction

Detailed in this chapter is a means of measuring the effective attenuation coefficient in vivo of human lung tissue using of two specifically designed probes, termed displacement sensor probes. To date the in vivo measurement of human lung tissue has not been measured. The effective attenuation coefficient of homogenised pig lung was determined and the effective attenuation coefficient, absorption coefficient and scattering coefficient of Soyacal by the added absorber method was determined.

The displacement sensor probes were constructed specifically for in vivo human lung experiments on anaesthetised patients but were also used for homogenised pig lung experiments. The displacement probes consisted of two diffusing spherical bulbs one as a light source and the other as a detector both having a thermocouple mounted on each bulb. The thermocouple was placed on the diffusing bulb to detect any unwarranted temperature rise during the in vivo experiment. The experiment was aborted if any uncharacteristic rise in temperature was detected. A coil was wound around each fibre with an oscillating field produced by one coil, which in turn induced a voltage in the second coil. This mutual inductance was the basis for measuring the distance between the two probes. The effective attenuation coefficient for homogenised pig lung tissue was obtained as a calibration standard to normalise the detected light flux in vivo

Twenty four successful measurements were recorded on fourteen patients with numerous experiments aborted due to the patient's ill health.

6.2 Added absorber method of determining the optical properties of a Phantom

Theory

The theory of light transmission through a highly scattering but low absorbance homogenous infinite medium can be described by diffusion theory ¹. In spherical geometry the diffusion theory yields an expression for the fluence rate (Φ_r) at a distance (r) from the point source

$$\Phi_r = \frac{\Phi_0 \exp(-\Sigma_{eff} r)}{r} \quad (6.1)$$

where

$$\Phi_0 = \frac{3P[\Sigma_a + (1-g)\Sigma_s]}{4\pi} \quad (6.2)$$

where P is the total power radiated by the source, Σ_a is the absorption coefficient, Σ_s is the scattering coefficient and g is the mean cosine of scatter. The effective attenuation coefficient can be described as

$$\Sigma_{eff}^2 = \frac{1}{d_{eff}^2} = 3\Sigma_a[\Sigma_a + \Sigma_s(1-g)] \quad (6.3)$$

where d_{eff} is the effective penetrating depth (depth at which the irradiance falls to 1/e or 37%). The effective attenuation coefficient Σ_{eff} is a useful parameter for comparing the general light transmittance characteristics of different tissues, although it is a complex combination of the fundamental coefficients. The effective attenuation coefficient will depend on the irradiation and tissue geometry.

Absorption and reduced scattering coefficients

The added absorber method² is a means of experimentally determining the constituent parts of the effective attenuation coefficient Σ_{eff} ie the absorption coefficient Σ_a and the reduced scattering coefficient Σ_s' .

$$\Sigma_s' = \Sigma_s(1 - g) \quad (6.4)$$

By experimentally measuring the effective attenuation depth $\Sigma_{\text{eff},0}$ of a stock solution, equation 6.3 has two unknowns Σ_a and Σ_s' . To resolve these unknown coefficients another coefficient, which can be measured, is included in the equation.

With the addition of an absorbing medium known as the added absorber (Winsor and Newton india ink) to the stock solution, the absorption coefficient Σ_a of the new solution becomes

$$\Sigma_a = \Sigma_{\text{ink}} + \Sigma_{as} \quad (6.5)$$

where Σ_{as} is the inherent absorption coefficient of the original medium, and the absorption coefficient of the ink is

$$\Sigma_{\text{ink}} = K \cdot \varepsilon_p \cdot \quad (6.6)$$

K is the concentration of the added absorber with the extinction coefficient³ as

$$\varepsilon_p = \frac{A}{bc} \quad (6.7)$$

where A is the absorbance, b is the distance travelled by the light through the medium and c is the concentration. The assumption being that the added absorber does not alter the light scattering properties of the medium. Winsor and Newton india ink was used as the added absorber as it was found to be nearly totally absorbing with an insignificant scattering coefficient.

Adding ink to the stock solution, where the absorption coefficient of the ink Σ_{ink} can be measured, will produce an effective penetration depth Σ_{eff} of the new solution. By experimentally measuring the $\Sigma_{eff,0}$ of the stock solution and Σ_{eff} of the new solution, two equations with three measured known parameters Σ_{eff} , $\Sigma_{eff,0}$ and Σ_{ink} can be used to find the two unknown parameters Σ_{as} and Σ_s' .

$$\Sigma_{eff,0}^2 = 3\Sigma_{as}[\Sigma_{as} + \Sigma_s(1-g)] \quad (6.8)$$

$$\Sigma_{eff}^2 = 3(\Sigma_{as} + \Sigma_{ink})[(\Sigma_{as} + \Sigma_{ink}) + \Sigma_s(1-g)] \quad (6.9)$$

6.3 Dipole theory for displacement probes

The device employs the change in mutual inductance between two coils where the sensitivity is dependent upon parameters such as the shape and size of the windings, inductance, voltage amplitudes, frequency and current, etc. The induced current in a coil resulting from the presence of alternating current in an adjacent coil is calculated for a case of two similar circular coils.

Treating the probes as two cylinders of sufficiently small dimensions that: (a) field from P is analogous to a magnetic dipole and (b) field at Q is uniform over probe diameter and length as shown in figure 6.1. Thus we can estimate the coupling as follows:

Suppose m (electromagnetic moment) is a small current-loop dipole by resolving it into two components, one along r ($m \cos \theta$) and one perpendicular to r ($m \sin \theta$) the separate B fields of these components are found as shown in figure 6.2. The r ($m \cos \theta$) component was found from the on axis B field of a circular coil using the Bio-Savart law.⁴

$$B_r = \frac{\mu_0 2m \cos \theta}{4\pi r^3} \quad (6.10)$$

$$B_\theta = \frac{\mu_0 m \sin \theta}{4\pi r^3} \quad (6.11)$$

$$B_\phi = 0 \quad (6.12)$$

where r is the distance between the two dipoles and μ_0 is the permeability of free space.

For a probe that is small and aligned with P, $\theta = 90^\circ$ and by definition $m = IA_e$, where I is the current and A_e is the effective area of the coil therefore

$$B_r = 0 \quad (6.13)$$

$$B_\theta = \frac{\mu_0 IA_e \sin \theta}{4\pi r^3} = \frac{\mu_0 IA_e}{4\pi r^3} \quad (6.14)$$

$$B_\phi = 0 \quad (6.15)$$

If coil Q has N' turns and each has area A' , the flux linked is

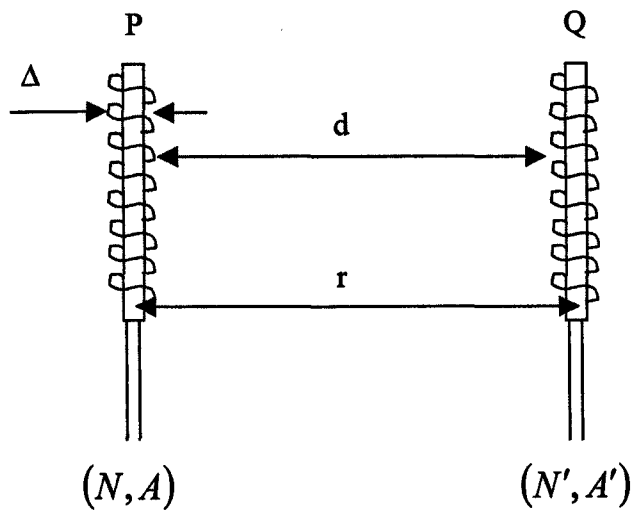


Figure 6.1 Mutual inductance coils

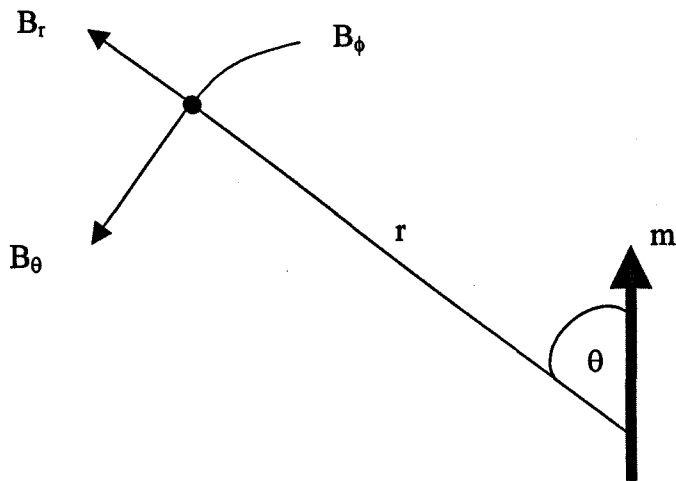


Figure 6.2 The B field due to a magnetic dipole of moment m

$$\phi = B_{\theta} N' A' \quad (6.16)$$

and induced voltage is

$$\Sigma = -\frac{\partial \phi}{\partial t} = N' A' \frac{\partial B_{\theta}}{\partial t} = \frac{N' A' \mu_0 A_e}{4\pi r^3} \frac{\partial I}{\partial t} = \frac{N' A' \mu_0}{4\pi r^3} A_e \omega i_0 \quad (6.17)$$

where current of the form $I = i_0 \sin \omega t$

now $r = d + \Delta$ where Δ is the coil diameter and d is the spacing between the coils and

$A_e = N A$ therefore the induced voltage is given by

$$\Sigma = \frac{N' A' \mu_0 N A}{4\pi r^3} \omega i_0 \quad (6.18)$$

6.4 Displacement sensor probe construction

A Farnell signal generator was used to produce an oscillating sine wave at 10 MHz. An oscilloscope was connected to both the signal generator and pickup coil. The induced voltage from the pickup coil was inverted and added to the original signal from the signal generator. The difference between the signal generator voltage and the combined voltage was then observed from the oscilloscope.

The displacement sensor probe as shown in figure 6.3 was constructed to detect the amount of light in vivo at a known distance through human tissue. This was constructed with two optical fibres, thermocouple and wire wound coils producing a mutual inductance field between the two. The probes were inserted down a rigid bronchoscope into the patients lungs.

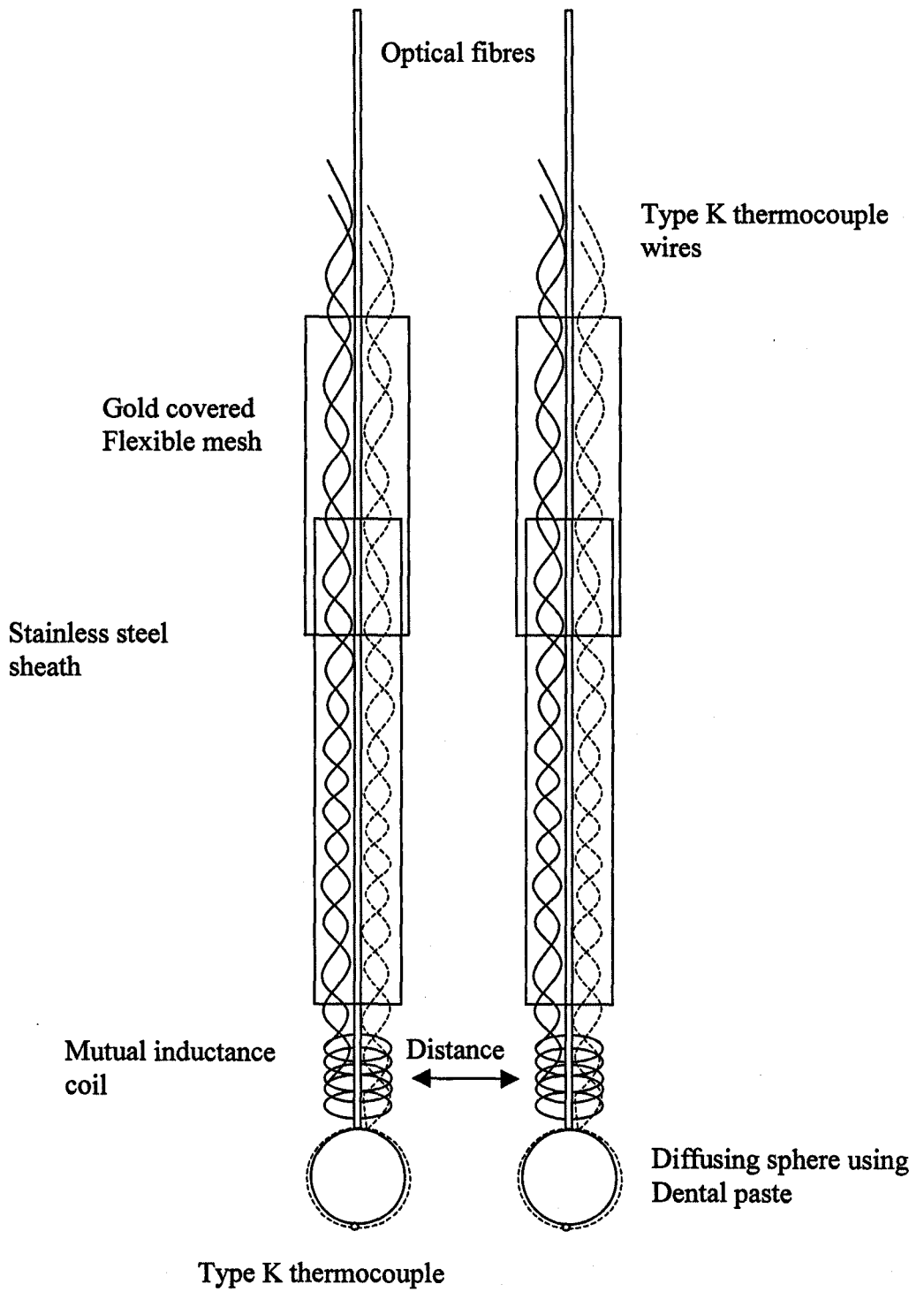


Figure 6.3 Displacement sensor probes for the measurement of light in vivo

Optical fibre preparation

The manufacturing technique described is used for plastic clad silica fibres, with a core diameter of $600\mu\text{m}$. The fibre ends are cleaved to obtain the required length of three metres. The outer protective plastic cladding of the fibre was removed, this was done using a designated stripping tool for the selected fibre diameter. The stripping tool removes a minimum length of 7mm protective sheath. On small core diameters cleaving produces a reasonable flat surface, however with larger diameter fibres cleaving is often followed with polishing due to core shattering.

Grinding was necessary to reduce the length of the stripped fibre to 2-3mm. The inner plastic cladding is retained while grinding, as this prevents the core from shattering. Using a fibre holder to secure the fibre, grinding is carried out using a fine grade wet and dry emery paper until the fibre end was flat and of the correct length. Once this was achieved, polishing was carried out using increasingly fine lapping paper down to $3\mu\text{m}$, until a polished surface was produced.

The plastic cladding is then removed, care is taken not to damage the polished diffusing end. This is achieved by gently scraping with a fingernail while supporting the fibre core. It is often difficult to remove the 0.25mm of cladding nearest to the plastic coating and was not necessary to do so. The exposed fragile silica core was de-greased using a tissue soaked in methanol or similar solvent.

Light diffusing sphere for optical fibre

Development work on light cure polymers at blue photoinitiation wavelengths has evolved from applications in dentistry.⁵ These resin based restorative materials were primarily used as dental fissure sealant. Consequently, the light cured polymer contained aesthetic additives in order to give a white enamel appearance similar to that of teeth. These aesthetic additives were powdered Titanium oxide or Silicon oxide and were used not only for the appearance but provided mechanical strength to the polymer. The amount of light scattering within the polymer can be controlled by the quantity of the additive.

The procedure for the construction of the diffusing bulb is essentially very simple. A thin coat of an acrylic copolymer (Op – Site spray dressing) is applied to the bare end. The fibre is dipped into a finely sieved titanium oxide powder immediately after each spray. The titanium oxide powder is embedded in the layer of acrylic and scatters light out of the diffuser. Several repeat sprays of Op-Site and dips into the oxide are required to provide a uniform appearance.

With the tip of the prepared fibre immersed in dental sealant, light from an Argon-ion (488nm) laser coupled to the other end was passed down the fibre causing the paste to harden and produced a partially cured small spherical bulb.⁶ The dental fissure sealant was configured into a small spherical shape by varying the power and time exposure of the cure. The output energy from the laser was controlled with Neutral density filters.

Removing the partially cured probe from the remaining uncured polymer results in a surface layer of material adhering to the underlying probe. This gives the bulb a “tear-drop” appearance that tends to diminish the uniformity of the surface flux. This is a viscosity problem and can be resolved by placing the semi-cured polymer in methanol. This removes any uncured polymer and allows the bulb to be cured rigid by delivering greater light energy. The net result of this process is a near perfect spherical bulb of rigid mechanical strength firmly adhered to the fibre tip.

Thermocouple Placement

A Type k wire thermocouple was placed on the surface of the spherical bulb. The thermocouple was placed at the bottom of the bulb with the wires following the geometry of the bulb on opposite sides. The thermocouple wires were then non-inductively wound together and run along side the optical fibre. The ends were terminated 1metre from the bulb with standard connectors. Thermocouple extension wire was used to connect between these ends and a Thurlby digital thermocouple meter. To secure the thermocouple on the diffusing bulb a small amount of dental paste was smeared on to the bulb then irradiated with 488nm-laser light.

Mutual inductance coil construction

Plastic insulated copper wire of diameter 0.18mm was used for the windings of the mutual inductance coils. The wire was run along the length of the optical fibre and temporarily held in place by cable tie-wraps. The coil winding started from the

spherical diffusing bulb and was manually wound around the optical fibre and thermocouple 40 times . Dental paste was used to secure the wire in place every five turns. The dental paste was cured using a portable Argon ion laser and a bare ended fibre as the light delivery system, which was flexible and convenient to manipulate around the coil. A second coil was wound around the first and secured with dental paste. The two three metre wires lengths were non-inductively wound together by placing each end of the wire into the chuck of a hand driven drill. By keeping the tension on the two wires and slowly turning the handle of the drill, kinks were avoided. The twisted pair was placed beside the fibre and temporarily held in place with cable ties.

Rigid Sheath for handling purposes

Before any connections to the optical fibre, thermocouple and inductance coil were made a 50cm stainless steel sheath with an outer diameter of 3.26mm, was placed over the optical fibre and cables. The sheath was positioned above the inductance coil with the opposite end secured in place with heat shrink cladding. The end of the sheath near the diffusing bulb was sealed using dental paste cured with 514nm laser light for hygiene purposes.

Probe Shielding

It was found that the 3m length of wire from the induction coil was susceptible to interference from external sources, therefore shielding the probe was necessary. The

shielding was provided by strips of flexible gold coated mesh. These strips were then wound around the fibre and cables with each strip overlapping the previous to give a good electrical connection. The gold coated mesh was terminated at the top of the stainless steel sheath. A piece of heat shrink cable was then shrunk around the mesh and stainless steel tube ensuring a good mechanical and electrical bond.

Probe Terminations

The opposite end of the fibre was ground and polished in preparation for the 600 μ m SMA connector. The inner plastic core is then stripped using a fingernail and the core placed in the connector. Inserting the prepared fibre and epoxy adhesive into the SMA connector a mechanically strong bond was formed. The inductance coil wire ends were terminated using a shielded connector attached to the gold covered mesh. The induction coil wires were soldered in place with the connector then “potted” using an acrylic potting resin. This ensured that the inductance coil wires were not able to move and create false signals.

The optical fibre and associated wires that ran along side the probe were covered in cable spiral wrap, this held the cables and gold covered flexible mesh in place and provided the cable bundle with an outer protective covering. A second probe identical to the first was constructed and termed the “detecting probe” this connected to an photosensitive detector.

6.5 Experimental methods

Soyacal

Soyacal, Intralipid and Nutralipid are the most commonly used fat emulsions, which are used clinically as intravenously administered nutrients. These fat emulsions are widely used as the basis of phantom materials for the investigation of the optical properties of tissues. Fat emulsions are suitable tissue phantom materials as they are highly scattering with low absorption. The liquid nature of the phantom material facilitates the measurement of internal light distributions. By varying concentrations of the fat emulsion and the known added absorber, simulating tissue is possible with measurements of cm's in the solution equivalent to mm's in tissue. The optical parameters of fat emulsions namely, the mean cosine of scatter, the absorption and scattering coefficients have previously been investigated near the 633nm wavelength by other authors^{7 8 9} All reports have differing results depending on the fat emulsion used, theoretical interpretations and experimental methods as shown in Table 5.1.

The 10% Soyacal consists mainly of fractionated soya beam oil diluted to 10% solution with water. The Soyacal was further diluted to a 1% aqueous solution with de ionised water filtered to 2 μm . Winsor and Newton ink was added in varying concentrations as the added absorber and was thoroughly stirred into the Soyacal solution.

The experimental arrangement for the measurement of the effective attenuation coefficient for Soyacal with and without added absorber is shown in figure 6.4. A 10-litre glass tank painted matt black on the inside to reduce reflections was filled with the aqueous Soyacal solution. A 38mW HeNe laser beam was chopped at 100Hz and

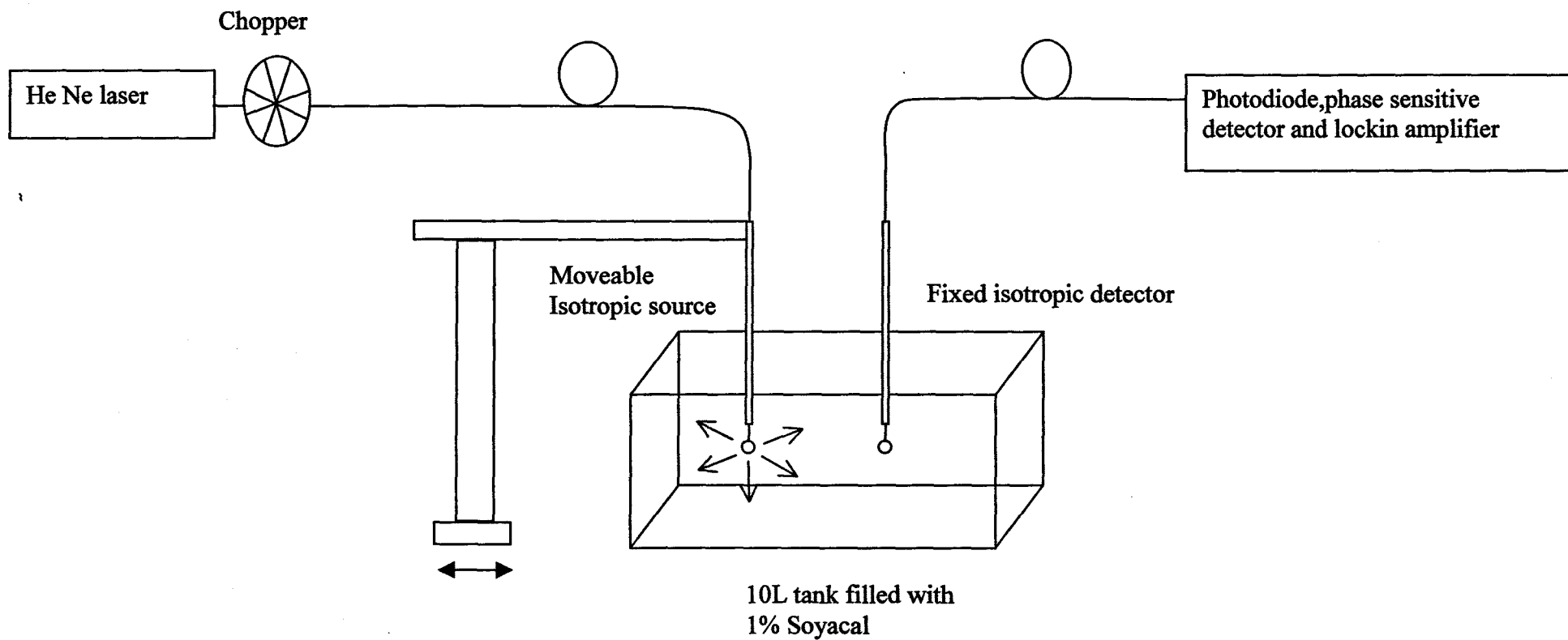


Figure 6.4 Light source and detecting probes in a 10 litre tank. The added absorber technique for measuring the scattering and absorption coefficients of a 1% aqueous solution of Soyacal.

coupled to the source probe of the displacement sensors. The source probe was positioned vertically in the 10-litre tank and attached to an XYZ positioning mount. The 50cm long stainless steel sheaths of the source and detecting probes were both mounted on plastic rods for added mechanical strength and to insulate the probes from any contact of the metal mounts. To measure the detected light flux the detecting probe was positioned vertically in the tank, fixed rigid and aligned with the source probe. The light via the detecting probe was detected by a photodiode, phase sensitive detector and lock-in amplifier, which tracked the frequency of the chopper and amplified the detected voltage. The detecting probe was moved away from the source probe using the XYZ mount. The accuracy of the mount was found to be $\pm 0.025\text{cm}$.

Lung tissue

The experimental arrangement for the measurement of the effective penetration depth for homogenised lung tissue was similar to that of Soyacal. The homogenised lung tissue was prepared in an identical manner to the experiments in outlined in chapter 4 and 5 as stated before. The homogenised lung sample was placed in a glass beaker with the sides and bottom painted matt black.

The source probe was attached vertically to a XYZ mount and placed such that the diffusing bulb was midway down the beaker. The detecting probe was attached vertically to a rigid stand with the source probe being aligned to this. The source probe was connected to an Oxford Laser Argon-ion pumped dye laser tuned to 630nm. A Laser Therapeutics power meter measured the power in Watts from the isotropic source probe.

The isotropic source probe was noted to shatter at 400mW when immersed in homogenised lung tissue. The tissue surrounding the probe was seen to be charred and fused to the probe. The source probe was then immersed in homogenised lung tissue for a period of 4 minutes with a 200mW output, the temperature reading of the thermocouple on the surface of the bulb rose to 60°C. The output from the isotropic source probe for all experimental work was then set to 200mW, which produced a detectable light source over the required distance for homogenised lung tissue.

When the displacement sensors were fully submerged in the homogenised lung tissue the detecting probe was moved away from the source probe using the XYZ mounts. The induced voltage from the induction coil and detected light were measured as a function of distance. It must be noted that there was no visible difference in the induced voltage between the two coils in air or when submerged in lung tissue. After the experiments the source and detecting probes were then removed from the XYZ mounts and sterilised with either alcohol or a sterilising fluid depending on hospital procedure.

In vivo experimental method

All patients gave consent to the experimental procedure. Each patient had been anaesthetised and prepared for surgery before any experimental procedure was undertaken and had been given a prior injection of the photosensitiser PII. The time that the source probe was irradiating the tissue with light when in vivo experiments were carried out was kept to a minimum due to the presence of the photosensitiser.

The consultant Surgeon (Prof. Moghissi) inserted the source probe down the rigid bronchoscope into the patients bronchus and then repositioned the probes into the tumour. The detecting probe was then inserted down the rigid and positioned close to the source probe. When the surgeon was confident that the probes were successfully placed the laser light was applied and measurements taken for the distance, temperature and detected light. The laser was immediately switched off after the experiment due to each patient having previously been injected with a photosensitiser and possible photodestruction of the nearby tissue. The surgeon then repeated the placements of the probes and if possible another set of measurements were taken. The repeat procedure was only accomplished on several patients as the probes restricted the airway and the patients vital signs deteriorated. After each experiment the probes were gently washed with sterilising fluid to remove any lung tissue or blood.

Displacement sensor Alignment

A displacement sensor probe was attached horizontally to a small rotating table with the second probe positioned above and parallel to the first and independent of the rotating table. The probes were aligned such that the diffusing sphere of each probe was at the centre of the rotating table. When the table was manually rotated the angle θ between the displacement sensor probes increased from $\theta = 0$ to $\theta = 60^\circ$. There was no change in the induced voltage from the displacement probes from $\theta = 0^\circ$ to $\theta = 15^\circ$. The 50cm probes, when used in vivo were placed down a 25cm long rigid bronchoscope with maximum diameter of 3cm resulting in a maximum angle between the two probes of 7° .

When the surgeon used the displacement probes in vivo it was noted that the probes would cross one another producing a “knitting needle effect”. A simple experiment was performed to investigate any adverse effect from this cross over. A displacement sensor probe was attached to a rotating table with the second probe fixed parallel but independent of the table as before. The probes were fixed such that the centres of the mutual inductance coils were placed over the centre of the table. When the table was manually rotated a “knitting needle” effect was then observed between the two probes. No discernible change in the induced voltage was observed for $\theta < 8^\circ$.

The displacement sensor probes when used in vitro were vertically aligned by sight and by using the maximum deflection from the induced voltage of the pickup coil. It was observed when both probes were aligned vertical and parallel to one another that a vertical movement from one probe decreased the induced voltage, as expected. A greater vertical movement, where the coils were only midway aligned, produced a phase shift in the induced voltage. This phase shift was used when aligning the probes in vivo. The probes were also graduated at the top of the stainless steel sheath indicating when the diffusing bulbs at the other end were aligned.

6.6 Results

By measuring the parameters required to evaluate the induced voltage Σ in equation (6.18) for the displacement sensor probes a comparison of the theoretical model and experimental data can be assayed. A frequency of 10MHz with a peak to peak voltage of 15V induced $60\mu\text{V}$ (peak to peak) in the pickup coil at a distance of 3 mm. A plot of

the normalised induced voltage for both experimental and theoretical data versus distance is shown in figure 6.5 with near field effects ignored.

The absorption coefficient of the added absorber (ink) Σ_{ink} was found by finding the extinction coefficient ϵ_p of the ink and multiplying this by the concentration K of ink used as in equation (6.6). The extinction coefficient of ink at 630nm was measured using an ultraviolet / visible ATI Unicam 5625 spectrophotometer. Using increasing concentrations of ink and water into a 10mm cuvette the absorbance of the solution was measured using a spectrophotometer. A graph of ink concentration versus absorbance can be seen in figure 6.6 from which the gradient was determined. Using equation (6.7) the extinction coefficient for the Winsor and Newton india ink was found to be $0.00025\text{mm}^{-1}(\mu\text{l/l})$. Using equation (6.6) the absorption coefficient for the concentration of ink used was found to be $\Sigma_{\text{ink}} = 0.0625 \text{ mm}^{-1}$.

Measuring the fluence rate in Soyacal suspension with and with out the added absorber gives the effective attenuation coefficients. This was achieved by placing the source and detecting probe in a 10 litre tank filled with the required solution as discussed earlier. From equation (6.1) a plot of the normalised fluence $\ln(\phi/r)$ against distance r is shown in figure 6.7 and results in a straight line the gradient of which is equal to $-\Sigma_{\text{eff}}$. The graph yields the gradients $(-\Sigma_{\text{eff}0})$ and $(-\Sigma_{\text{eff}})$ for Soyacal with and without the added absorber respectively. As the diffusion approximation does not hold close to the source, the gradient was taken from the linear section of the graph. The effective attenuation coefficients were found be $\Sigma_{\text{eff}0} = 0.0355 \text{ mm}^{-1}$ and $\Sigma_{\text{effink}} = 0.1644 \text{ mm}^{-1}$.

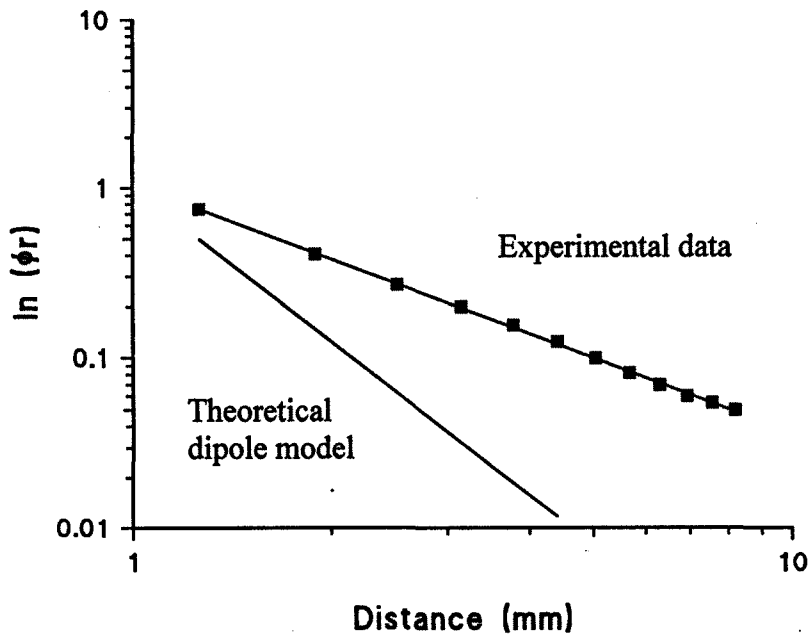


Figure 6.5 Theoretical and experimental data for induced voltage vs. distance using displacement probes

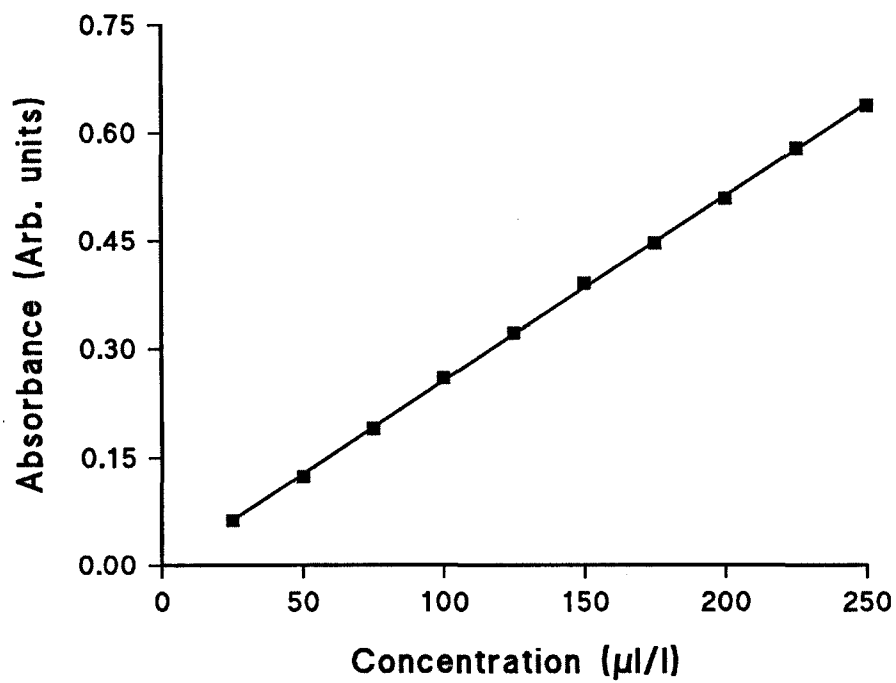


Figure 6.6 Absorbance vs. concentration of Winsor and Newton ink using a spectrophotometer at 630nm

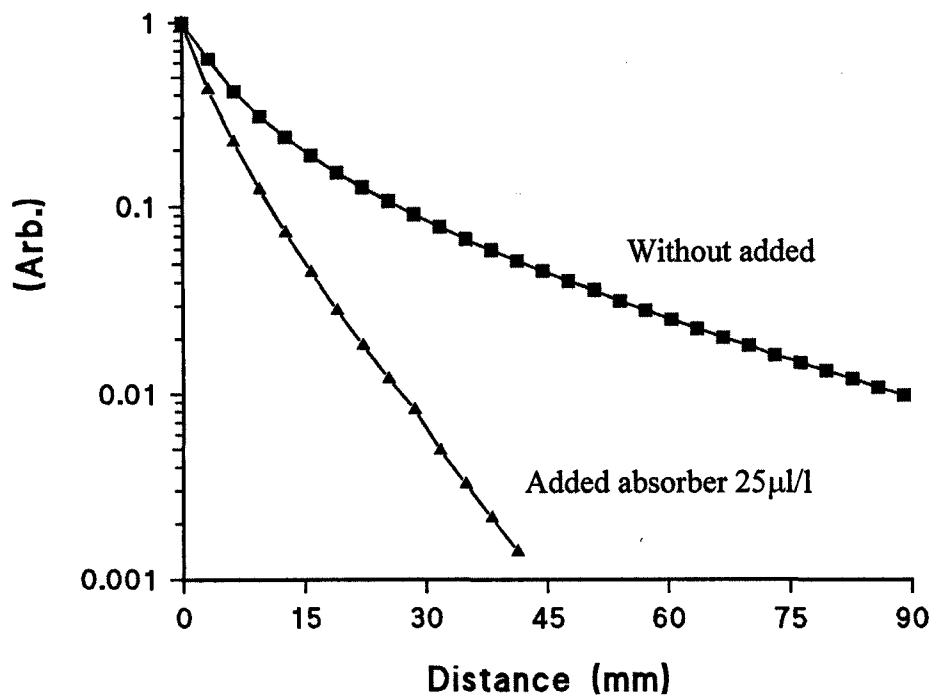


Figure 6.7 Plot of normalised detected light flux vs. distance for a 1% Soyacal solution with and without added absorber

From the values obtained for $(-\Sigma_{eff}), (-\Sigma_{eff})$ and Σ_{ink} the two simultaneous equations (6.8) and (6.9) were solved for the absorption coefficient of Soyacal Σ_a and the reduced scattering coefficient Σ_s' by using Mathematica (a mathematical computer package) by Wolfram Research. The reduced scatter was found to be $\Sigma_s' = 1.26 \text{ mm}^{-1}$ and the Soyacal absorption coefficient $\Sigma_a = 3.06 \times 10^{-4} \text{ mm}^{-1}$. Since the reduced scattering coefficient $\Sigma_s' = \Sigma_s(1-g)$ the scattering coefficient Σ_s can be found with the knowledge of the mean cosine of scatter g . In chapter 4 the mean cosine of scatter was found for Soyacal and quoted in Table 4.1 as $g = 0.82$. This was used to find the scattering coefficient $\Sigma_s = 7 \text{ mm}^{-1}$.

Using the displacement sensor probes mounted on a XYZ mount a plot of the normalised fluence $\ln(\phi r)$ against distance r is shown in figure 6.8 for homogenised pig lung and results in a straight line the gradient of which is equal to $-\Sigma_{eff}$. The effective attenuation coefficient for homogenised pig lung was found to be 10.3 cm^{-1} .

The in vivo experimental results are shown in figure 6.9 from which the Effective attenuation coefficient was obtained $\Sigma_{eff} = 11.8 \text{ cm}^{-1}$. The induced voltage and detected light from the displacement sensor was measured and recorded. The equivalent induced voltage from figure 6.5 was then used to obtain the distance in mm. The detected light was normalised from previous measurements, when the probes were immersed in homogenised lung tissue with laser output of 200mW as in figure 6.8. Fourteen patients were used in the experiments with 24 measurements of significant data.

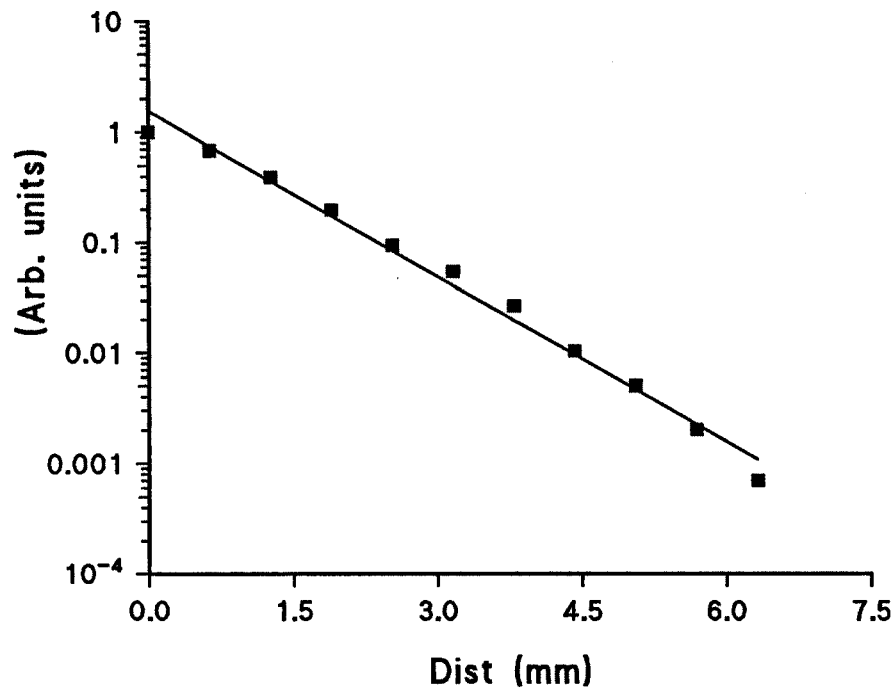


Figure 6.8 Plot of normalised detected light flux vs. distance for homogenised pig lungs for displacement probes

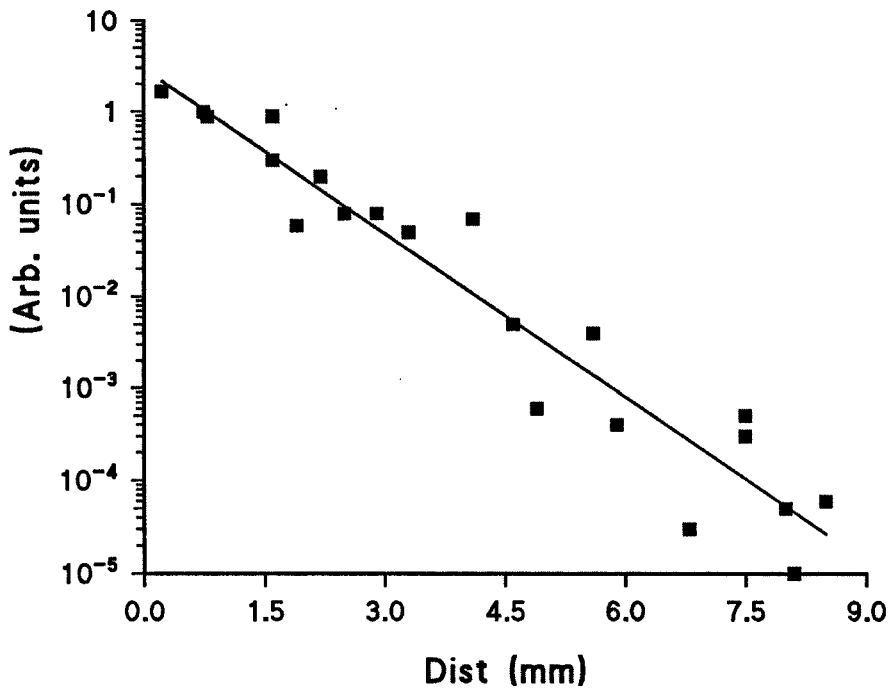


Figure 6.9 Plot of normalised detected light flux vs. distance for in vivo position displacement probes on fourteen patients

6.7 Discussion

The effective attenuation coefficient for Soyacal was found to be $\Sigma_{\text{eff}} = 0.0355\text{mm}^{-1}$ therefore the effective penetration depth $d_{\text{eff}} = 28$ mm. The units mm are not consistent with the units for lung tissue given in cm but are presented this way for clarity as previous researchers have reported the values in mm. The reduced scattering given as $\Sigma'_s = 1.36\text{mm}^{-1}$ is used to obtain the scattering coefficient from equation (6.4) and by using the experimental value for the mean cosine of scatter given in chapter 4 the scattering coefficient $\Sigma_s = 7.6\text{mm}^{-1}$. A comparison of these results is given in table 5.1. The added absorber method for evaluating the effective attenuation coefficient, the scattering coefficient and the absorption coefficient is in agreements with other researchers and with the other methods described in chapter 5.

Homogenised pig lung effective attenuation coefficient was found to be 10.3cm^{-1} and the in vivo human lung effective attenuation coefficient was found to be 11.8cm^{-1} . This is in agreement with experimental results in chapter 5 and other authors given in table 5.1. The greater the distance between the two probes the greater the error due to the decreasing induced voltage from the pick up coil. A greater applied field from the source probe would increase the range of the probes but the amount of current passed down the coil would create a safety problem. Additionally increasing the field strength might interfere with other equipment in the operating theatre. Increasing the number of turns in the coil has a practical limit of coil diameter and mechanical strength.

The theoretical model for the induced voltage of the two probes breaks down in the near field region. As shown in figure 6.5 the dipole model deviates from the experimental

results as the distance between the two probes increase. The dipole model for distances over 5mm is inappropriate and needs refining especially if it is to be used successfully in predicting the distance between the two probes. In practice when a coil is placed near another coil with an oscillating field, mutual inductance occurs between the two coils. The mutual inductance between the coils will itself, set up a field which will interact with the source field and therefore a near field effect is setup as the coils come closer together. The in vivo experimental voltages taken for the distance between the two probes was converted to distance in mm by the experimental data in figure 6.5.

The in vivo placement of the displacement sensor probes was of great relevance to the measurements taken. The alignment and positioning of the two diffusing spheres can not be visibly ascertained. It was observed on numerous experiments that the consultant surgeon had mistakenly placed the fibres either in air or out of alignment. The respiratory movement of the patient and the movement caused by the surgeon holding the probes gave rise to practical problems of measuring the distance and detected light. A computer simultaneously recording all the data from the equipment could overcome this.

6.8 References

1. Wave propagation and Scattering in random media, Ishimaru A, Academic Press, (New York) Vol 1, 1978
2. Wilson B C, Patterson M S, Burns DM, LIMS 1, 232 (1986)
3. Absorption Spectroscopy, Bauman P R, New York, Wiley (1962)
4. Electricity and Magnetism, Duffin W J, McGraw Hill, 3rd. Ed. (London), Chpt. 7 (1980)
5. Cook W D, Standish P M, Aust. Dental Journal 28, (5), 307, (1983)
6. Murray R T, Jones M, SPIE 1040, 94 (1988)
7. Star W M, Marijnissen, J P Ansen H J, Keijzer M, van Gemert M J C, Photochem. Photobiol. 46, 619 (1987)
8. Moes C J, van Gemert M J C, Star W M, Marijnissen J P A, Prah S A, Appl Opt. 28, 2292 (1989)
9. Driver I, Feather J W, King P R, Dawson J B, Phys. Med. Biol. 34, 1927 (1989)

7 Conclusion

Absorption and scattering of laser light in biological media were studied. First an overview of PDT was detailed in chapter 2 and a mathematical model for light propagation in media was derived in chapter 3. Methods for determining the in vitro tissue optical properties such as absorption coefficient, scattering coefficient and phase function were examined in chapter 4 and 5. From these measurements the effective attenuation coefficient can be derived. Chapter 6 contains details of a specifically designed probes for in vivo bronchial measurements of the effective attenuation coefficient through human lung tissue. To date there has been no in vivo measurements on human lung tissue.

The models currently used ie the diffusion approximation and Kubelka-Munk theory on the light distribution in tissue were examined. The diffusion approximation has been popular since it provides a relatively simple solution of radiative transfer theory and its assumption on dense media is appropriate for most biological media. The diffusion approximation to the transport equation in a slab geometry suggests a simple experimental protocol to determine absorption, scattering and the scattering anisotropy factor from a measurement of the reflection and transmission of a small volume slab of material. For highly scattering media the diffusion approximation is considered to give good estimations. The diffusion theory is written in terms of diffuse forward and backward fluxes which allows a comparison with the K-M model.

A method for measuring the angular dependence of scattering for tissue was presented in chapter 4. The experimental arrangement is referred to, as a goniophotometer and

could be improved by placing the sample and detector (optical fibre) in water. This would reduce the reflection and refraction effects between the sample and detector. The H-G phase function was best found to characterise scattering from tissue. The phase function was evaluated from the anisotropic forward-scattered light and the isotropic back-scattered light. Thin tissue samples were required to estimate the H-G anisotropy and isotropy factor. The isotropic back-scattered light although small in comparison to the forward transmission is still accountable for the H-G phase function. From table 4.1 it can be seen that there is a large variance in values for the phase function from other researchers, which is accountable by the theoretical models and experimental methods used. The mean cosine of scatter g for pig lung with blood was found to be 0.925. The values presented in chapter four are comparable to previously published results.

Scattering and absorption coefficients were measured based on transmission and reflection measurements using an integrating sphere. The theory of the integrating sphere allows the description of uncertainties in the reflectance and transmittance measurements of a sample. These uncertainties suggest that collimated light is preferential to diffuse incident light. Diffuse light measurements for lung tissue samples were not practical, as the sample area does not cover the port of the integrating sphere. Once the reflected and transmitted values had been extracted from the integrating sphere measurements the absorption and scattering coefficients for the tissue were then computed for the K-M solution of the transport equation.

Other researchers have quoted values for the absorption and scattering coefficients for lung tissue and can be seen in table 5.1. The numerous different values of the coefficients for the same tissue type are due to the theoretical models and experimental

methods used. All the researchers have quote values for the absorption and scattering coefficients of tissue without blood. This method while enabling consistent tissue samples does not related to the practicality of blood flow etc. Since space irradiance is greatly dependent on albedo especially for values close to 1 as in human tissue a small variation in the absorption coefficient value could result in a great modification of the light propagation pattern.

For an optical phantom the added absorber method presented in chapter six to determine the absorption and reduced scattering coefficients is relatively straightforward. The assumption being that the added absorber is purely an absorbing medium and does not change the characteristics of the stock solution. The results obtained for the optical properties of Soyacal compare to the previous results in chapters 4 and 5 and with previous researchers. Ink was mixed with homogenised pig lung as an added absorber in an effort to measure the absorption and scattering coefficients but with little success. The phantoms optical properties were measured and compared with other researchers to ensure the theoretical model and experimental procedure presented in this thesis were an effective method for ascertaining the phantoms, and hence the tissue samples optical properties. Since the optical properties of lung tissue have been measured, the optical properties of the phantom can be varied to copy that of lung tissue. Experiments can be carried out on the phantom and related to lung tissue.

The displacement sensor probes described in chapter 6 use mutual inductance to determine the distance between the two. As the distance between the two coils increases the induced voltage in the pickup coil reduces and is not detected beyond a range of 2cm. Increasing the number of windings is a solution to increasing the range

but will decrease mechanical strength of the fibre tip due to the displacement of the stainless steel sheath. There is a limit on the overall diameter of the probe hence the coil can not have a large number of windings on top of one another. Increasing the field strength will increase the range between the two coils but great care must be observed not to produce a field likely to interfere with any biological rhythms of the patient or any of the equipment in the theatre. If the range of the displacement sensor probes can be increased and the aligning method developed further, the probes could be used for any in vivo experimental work on optical properties of tissue.

Using the specially designed probes for in vivo bronchial measurements of human lung tissue a comparison between the in vitro and in vivo measurements can be assayed. The results can be applied in detecting optical properties and therefore estimating light dosimetry during PDT or any other similar light dependent treatment. This is important for medical applications of lasers

The displacement sensor probes are a successful method for measuring the in vivo effective attenuation coefficient of human lung tissue. This was found to be $\Sigma_{\text{eff}} = 11.8 \text{ cm}^{-1}$. The displacement sensor probes were used to measure the effective attenuation coefficient of homogenised pig lung and was found to be $\Sigma_{\text{eff}} = 10.3 \text{ cm}^{-1}$. The effective attenuation coefficient of homogenised pig lung and human tumour was found by using the results in chapter 4 and 5 and quoted in table 5.1. The homogenised pig lung and human tumour in vitro effective attenuation coefficients were found to be $\Sigma_{\text{eff}} = 9.6 \text{ cm}^{-1}$ and $\Sigma_{\text{eff}} = 9.0 \text{ cm}^{-1}$ respectively. These are comparable with the in vivo results.

The measured values for homogenised pig lung without blood are lower than the in vitro and in vivo measurements as expected.

The effective penetration depth d_{eff} is the reciprocal of the effective attenuation coefficient Σ_{eff} and is quoted in equation (6.3). The effective penetrating depth is defined as the depth at which the irradiance fall to $1/e$ or 37% of its initial value. Therefore by knowing the optical properties of the tissue an assessment of the light distribution through the tissue can be achieved. From Table 5.1 the penetration depth for human lung tissue has been reported by other researchers to vary between 0.2mm and 2mm. The in vivo experimental work carried out in this thesis has concluded that the penetration depth is 0.9mm and the in vitro experimental work on homogenised pig lung is 1.0mm.